The Investigation of Tendon ECM Alterations in Response to Stress Relaxation for Improving the Ponseti Method

A THESIS SUBMITTED IN PARTIAL FULFILMENT OF THE

REQUIREMENTS FOR THE DEGREE OF DOCTOR OF PHILOSOPHY

AT THE UNIVERSITY OF OXFORD

BY

MU-HUAN LEE

TRINITY COLLEGE

AND

DEPARTMENT OF MATERIALS

UNIVERSITY OF OXFORD

TRINITY TERM 2022

Preface

This thesis describes the work carried out by the author in the Department of Materials, University of Oxford, from October 2017 to October 2022, under the supervision of Prof. Jan Czernuszka and Chris Lavy. No part of this thesis has been previously submitted for a degree at this or any other university. The work of other authors has been drawn upon and has been referenced and acknowledged in the text. A list of references is given at the end of the thesis. Some of the work in the thesis has been reported in the following publications:

Publication

- Murtaza Kadhum, **Mu-Huan Lee**, Jan Czernuszka, and Chris Lavy. "An Analysis of the Mechanical Properties of the Ponseti Method in Clubfoot Treatment." Applied Bionics and Biomechanics 2019 (co-1st author).

- **Mu-Huan Lee**, Hung-Pei Tsai, Chris Lavy, Pierre-Alexis Mouthuy, and Jan Czernuszka. "Time-dependent ECM alterations of young tendons in response to stress relaxation – a model for Ponseti method." Journal of The Royal Society Interface 2022.

Abstract

Congenital clubfoot or congenital talipes equinovarus (CTEV) is a complex paediatric foot deformity which will lead to long-term disability, deformity, and pain if left untreated. At present, the Ponseti method composed of a series of manipulation and casting is recognized as the standard treatment for clubfoot. However, the evaluation for the treatment outcome is based primarily on the clinical examinations and functional parameters while no work has explored the material response and the alterations of extracellular matrix (ECM) of a clubfoot tendon in response to the treatment – a long term stress relaxation. *Ex vivo* stress relaxation experiments discovered time-dependent tendon lengthening and ECM alterations including crimp angle reduction and elastin fragmentation, which illustrated the mechanism behind the treatment – a material-based tissue lengthening resulted from elastin fragmentation. This proposed mechanism was further supported by the relaxation results using elastin-digested tendons which also found a positive contribution to stress relaxation and relaxation rate from elastin. As the changes in crimp and elastin structures will be influential in the function and health of the tendon tissue, the capability of recovery of these ECM alterations in a tendon became a critical examination. The *in vivo* results derived from stress-relaxed tendons of young rabbits observed restoration of the

above-mentioned ECM alterations along with increased elastin and vascularity level, and the existence of inflammation, indicating process of healing and recovery from the tendon in reaction to the treatment over time. While the increased vascularity and persisted inflammation may potentially bring concerns to the tendon health, they are both important biological adaptation in response to the mechanical treatment. Additionally, cellular response derived from the *in vitro* experiment discovered increased gene expressions of COL1A1 and ELN, supporting the incidence of recovery. Overall, this study reveals the treatment mechanism and proves the efficacy of the Ponseti method to correct clubfoot from an ECM-oriented perspective.

Acknowledgement

I would like to thank my supervisors, Jan Czernuszka and Chris Lavy for all their supports, guidance, and mentoring over the last five years. From every meeting and discussion, I learned not only materials science, but also the fascinating world of biomaterials and orthopaedics. Jan pushed me to become independent and helped me learn to be creative but practical at the same time. Chris was always there at the critical moments with valuable insights and suggestions. I am truly grateful for the opportunity to study under their supervision.

On the path to completing my research, thanks to Francis Szele in DPAG for lending me the microtome and microscope; thanks to Charlotte Williams and Georgina Gregory in the Department of Chemistry and James Marrow in the Department of Materials for lending me the mechanical testers; thanks to Jennifer Holter, Graham Wyatt, and Gareth Hughes for the EM-related supports and trainings; thanks to Pierre-Alexis Mouthuy, Sarah Snelling, and Sarah Salmon in NDORMS for providing the cells, equipment, laboratory space, and all the trainings for my cellular experiments; thanks to Yu-Ming Wang at TWBM, Yong-Ming Lin at MASTER LABORATORY Co., Ltd, and Hung-Pei Tsai at Kaohsiung Medical University for all their supports on

the animal study; and thanks to the Jardine Foundation for accepting me as a scholar and offering me the Jardine Postgraduate Scholarship for my DPhil study.

I want to thank the members in the Biomaterials Group: Jim Yang Xu, Sonia Iftekhar, Jerry Qu, Sasza Nabilla, Hazal Gezmis, Ilayda Karadag, and Zhaoying Ma; the committee members in OUTSS: Jeff Liu, Albert Lee, Wayne Wu, Gulung Lin, and Cindy Tsai; boxers and trainers in OUABC; and my best buddies: Michael Wojcicki and Said Abubakar. I have so many great memories in Oxford because of you guys. I am fortunate to know all of you.

Last but not least, I want to thank Mum, Dad, and Wen-Hsin for always being supportive for my overseas studies and life decisions, raising me up, and being my best friends since childhood. I want to thank my wife: Ya-No for living with my flaws, helping me become a better person, and showing me love every single day. I will not be able to finish this journey without your kind encouragements and loves.

Table of Contents

List of Abbreviations

ABS	acrylonitrile butadiene styrene
ACL	anterior cruciate ligament
BSA	bovine serum albumin
CCT	common calcaneal tendon
CT	cycle threshold
CTEV	congenital talipes equinovarus
DDFT	deep digital flexor tendon
DNase	deoxyribonuclease
DPX	dibutylphthalate polystyrene xylene
ECM	extracellular matrix
EDP	elastin-derived peptide
FM	fascicle matrix
GAG	glycosaminoglycan
GAPDH	glyceraldehyde 3-phosphate dehydrogenase
GT	gastrocnemius tendon
H&E	hematoxylin and eosin
HMDS	hexamethyldisilazane
IACUC	Institutional Animal Care and Use Committee
IFM	interfascicle matrix
IHC	immunohistochemistry
MMP	matrix metalloproteinase
MRI	magnetic resonance imaging
MVG	Miller’s elastic Van Gieson

NZW	New Zealand White
OCT	optimal cutting temperature
PB	phosphate buffer
PBS	phosphate buffered saline
PG	proteoglycan
qPCR	quantitative polymerase chain reaction
SBTI	soybean trypsin inhibitor
SD	standard deviation
SDFT	superficial digital flexor tendon
SDS	sodium dodecyl sulphate
SEM	scanning electron microscopy
S_N2	second-order nucleophilic substitution
SRB	sulforhodamine B
TEM	transmission electron microscopy
UTS	ultimate tensile strength
VVG	Verhoeff–Van Gieson

List of Figures

Figure 3.3. A demonstration showing the maker displacement (d_0 to d(t)) on the tendon surface before (left) and after 16 seconds of tensile testing (right).

Figure 3.4. A demonstration of a tendon strained to failure. The tendon sample were prepared and gripped as mentioned in the method section. Failure occurred at the middle of the sampling region of the sample.

Figure 3.5. Comparisons of the values of the surface strain (red) and the grip strain (blue) plotted against testing time of 3 separate tests (a, b & c). Paired t-test found no difference between the two strains for all 3 tests. A linear fitting was conducted and displayed for each test.

Figure 3.6. Mechanical results of the strain rate-dependency experiments. (a) Illustrative stress-strain profile of all 5 strain rates tested (1%/s, 0.5%/s, 0.1%/s, 0.01%/s & 0.001%/s), and the results of the strain rate-dependencies of the (b) Young's modulus and the (c) strain at UTS. Both data are plotted against the logarithm of the strain rate (%/s). Univariate linear regression ($y = a\,x + b$) was applied to (b), and the results generated a linear fit (red line) with a slope of 89.8 MPa and an intercept of 321.1 MPa with an R-Square of 0.93. All data are displayed as the mean ± standard deviation (SD) (n=3). $^*P < 0.05$.

Figure 4.1. Illustrative images of the adductus correction using a plastic clubfoot model. A plastic model for clubfoot without manipulation is shown in the left image in which the red lines marked the inward rotation angle of adductus at the medial side and the yellow arrows marked the string (an approximation of the tebialis posterior tendon) with an initial length (l_0). After correction, which is shown in the right image,

lengthening of the string (l_c) simulating the lengthening of tendons and ligaments in the clubfoot can be measured.

Figure 4.2. The stress-time mechanical profiles of the young bovine DDFTs undergoing 2 h of stress relaxation. (a) The initial 30 seconds of the relaxation profile displaying the transition from the 'toe' to 'linear' region. (b) The initial 20 minutes of the relaxation profile displaying the exponential decay of stresses. All data are displayed as the mean ± SD (n=3).

Figure 4.3. The tendon lengthening percentages due to stress relaxation. The lengthening ($\Delta L/L_0 \times 100\%$, L: tendon length; L_0: initial tendon length) of different relaxation durations (0 h, 2 h, 24 h & 48 h) calculated based on Eqn. 4.1. All data are displayed as the mean ± SD (n=3). Significant differences were analysed by 2-sample t-test. *P < 0.05, ***P < 0.001.

Figure 4.4. Mechanical profiles of the young bovine before and after the 2 h stress relaxation treatment. (a) The stress-strain curves of the first (blue) and second (red) tensile straining. The second test was conducted at the same initial stroke position and under the same strain rate of 0.5%/s as the first test. (b) The stress-strain curve of the initial 6% strain of (a). All data are displayed as the mean ± standard deviation (SD) (n=3).

Figure 4.5. SEM images of the stress-relaxed tendons (right column) and its control (left column). Scale bars are 500 μm (top row) and 50 μm (bottom row).

Figure 4.6. Illustration of crimp angle (θ) and side length (d) measurement. Scale bars are 50 μm.

Figure 4.7. Crimp angle reduction of tendons treated with stress relaxation. Crimp angle values of tendons treated with stress relaxation (blue) for different durations (0 h, 2 h, 24 h & 48 h) and their respective controls (red). Data are displayed as the mean ± SD (n=30). Significant differences were analysed by 2-sample t-test. *$P < 0.05$, ***$P < 0.001$.

Figure 4.8. Estimated values of tendon lengthening contributed by crimp angle reduction of tendons of different stress relaxation durations (2 h, 24 h & 48 h) calculated using Eqn. 4.2.

Figure 4.9. A tendon section stained with Miller's elastic stain. The collagen matrix was stained darkish red. The elastin, which should be stained black, was not observed. Scale bars are 50 μm.

Figure 4.10. Fluorescence images of tendon sections stained with SRB: (a) unfixed section; (b) fixed section; (c) section treated with hyaluronidase; (d) section treated with hyaluronidase and collagenase. Scale bars are 100 μm.

Figure 4.11. Fluorescence image of tendon section stained with SRB before and after background subtraction. Scale bars are 50 μm.

Figure 4.12. Fluorescence images of immunostained elastin and DAPI-stained cell nuclei. Representative immunostained tendon images captured by confocal microscopy revealing the morphology of elastin (green; left column), cell nuclei (blue; mid column) and tendon matrix (grey; right column) in bovine DDFTs. Images are displayed in the longitudinal view (top 2 rows) and the cross-sectional view (bottom 2

rows). Scale bars in the 1st and 3rd rows are 50 µm; scale bars in the 2nd and 4th rows are 25 µm.

Figure 4.13. Comparison of the elastin morphology (left column), cell nuclei (mid column) and tissue matrix background (right column) of a healthy tendon (top row) to those of a stress-relaxed tendon (bottom row). Scale bars are 25 µm.

Figure 4.14. Illustration of the collection and the quantification (particle analysis) of elastin fragments. The quantification process was conducted as follows: (I1) The regions containing fragmented elastin clusters were selected and cropped from the original image; (II2) the cropped images were converted to 8-bit grayscale; (III3) the threshold of the image was adjusted based on the mean fluorescence level (mean of 5 intensity maxima) of the local healthy/intact elastin (yellow circles) where all fluorescence signals lower than this mean were excluded; finally, (IV4) the total area of these elastin fragments were measured using particle analysis where only particles of size larger than 5 pixel^2 were included.

Figure 4.15. The elastin fragmentation ratio in the tendon matrix after the treatment of stress relaxation. Values of fragmentation ratio of young bovine DDFTs treated with stress relaxation of different durations (0 h, 2 h, 24 h & 48 h). Data are displayed as the mean ± SD (n=20). Fragmentation ratio is defined as the total area of elastin fragments over the image area (tendon matrix area) for each fluorescence image. Data are displayed as the mean ± SD (n=4). Significant differences were analyzed by 2-sample t-test. *$P < 0.05$, ***$P < 0.001$.

Figure 4.16. Illustration of the effect of adding alcohols or stress relaxation (prolonged tension) to the reaction solution of elastin hydrolysis. Under normal condition (left),

the folded conformation of elastin shield the hydrophobic region (red bars) from the water molecules; while under tension or the addition of alcohols (right), the unfolded conformation exposes the hydrophobic region to the water molecules, allowing hydrolytic degradation to occur.

Figure 5.1. An illustrative image for the Maxwell model describing a viscoelastic material. The model contains a spring as the elastic component (modulus, E) and a dashpot as the viscous component (viscosity, η) in series. When a fixed strain is applied, the dashpot dissipates the tensile load from the spring over time.

Figure 5.2. The percentage of tendon lengthening after the treatment of elastase. A control derived from tendon sections incubated with a PBS solution containing SBTI is included. All data are displayed as the mean ± SD (n=6). *$P < 0.05$.

Figure 5.3. Fluorescence images of tendon sections with (bottom row) and without (top row) the treatment of elastase revealing the immunostained elastin (left column), DAPI-stained cell nuclei (mid column), and tendon matrix (right column). Scale bars are 50 μm.

Figure 5.4. SEM images of tendon sections with (right column) and without (left row: incubated in PBS & mid row: incubated in SBTI solution) the treatment of elastase revealing the collagen fibre morphology of the tendon. Scale bars are 50 μm and 5 μm for the 100X images (top row) and the 2kX images (bottom row), respectively.

Figure 5.5. SEM images (left column) along with the histograms of directionality (right column) of tendon sections with (bottom row) and without (top row) the treatment of elastase captured under 5000X of magnification. Scale bars are 5 μm.

Figure 6.9. SEM images of the decellularized tendon sections or scaffolds. The decellularized tendon scaffold: blank scaffold with no cell seeding (left), the scaffold seeded with human tenocytes without stress relaxation (mid), and the scaffold seeded with human tenocytes treated with stress relaxation for 21 d (right). Seeded tenocytes are marked with red lines and red arrows. Scale bars are 10 μm.

Figure 6.10. Elastin and collagen type I gene expression levels due to the treatment of stress relaxation. Fold changes of gene expressions of COL1A1 and ELN of human tenocytes cultured on decellularized tendon treated with 21-d stress relaxation compared to tenocytes without stress relaxation. Data are displayed as the mean ± SD (n=3 for COL1A1 and n=2 for ELN). One data point of ELN level was excluded as an outlier. Significant differences were analysed by 2-sample t-test. No statistical difference was found in all groups in both experiments.

Figure 6.11. Demonstrative image of a 45-day-old NZW rabbit after the stress relaxation treatment via manipulation and tapping. Redness and swelling can be seen on the muscles at the back of the left leg.

Figure 6.12. Demonstrative images of the CCT-muscle complex collected from NZW rabbits treated with stress relaxation for 1 day (left image) and 7 days (right image).

Figure 6.13. Demonstrative images of blood vessels presenting in rabbit CCTs which were stress-relaxed for 7 days. CCT samples were incubated in 30% sucrose cryoprotectant to increase transparency.

Figure 6.14. SEM images of the tendon sections. Tendon surface morphology of the young rabbit GT (top row) and SDFT (bottom row) sections of the control (left

column), the foot stress-relaxed for 1 d (mid column), and the foot stress-relaxed for 7 d (right column). Scale bars are 100 μm.

Figure 6.15. Summary of the values of crimp angle reduction due to stress relaxation. The amount of the crimp angle reduced after the treatment of stress relaxation plotted over different relaxation durations (1 d & 7 d) for both GT and SDFT of the young rabbits. Data are displayed as the mean ± SD (n=4). Each $\Delta\theta$ value is calculated by subtracting the stress-relaxed angle from the mean angle of the control ($\overline{\theta_{\mathrm{ctrl}}} - \theta_{\mathrm{exp.}}$). Significant differences were analysed by 2-sample t-test. *P < 0.05, ***P < 0.001.

Figure 6.16. Representative immunostained tendon images captured by confocal microscopy revealing the morphology of elastin (green), cell nuclei (blue) and tendon matrix (grey) in (a) a rabbit GT and (b) a rabbit SDFT after the treatment of stress relaxation for 1 d & 7 d. Examples of elastin fragmentation caused by stress relaxation appear as aggregated clusters with higher fluorescence intensity compared to the intact elastin fibres. No elastin fragment can be found in the controls. Scale bars are 50 μm.

Figure 6.17. The elastin fragmentation ratio in the tendon matrix after the treatment of stress relaxation. Values of fragmentation ratio of young rabbit GTs and SDFTs treated with stress relaxation for 1 d and 7 d. Fragmentation ratio is defined as the total area of elastin fragments over the image area (tendon matrix area) for each fluorescence image. Data are displayed as the mean ± SD (n=4). Significant differences were analysed by 2-sample t-test. *P < 0.05.

Figure 6.18. Changes in Elastin fluorescence levels due to the treatment of stress relaxation. Elastin protein level ratios of 7-d stress relaxation over 1-d stress relaxation of young rabbit GTs and SDFTs calculated based on Eqn. 6.2 using fluorescence level

changes normalized by the controls. Data are displayed as the mean ± SD (n=4). Significant differences were analysed by 2-sample t-test. No statistical difference was found between the two tendon groups.

Figure 6.19. Quantification of cell number alterations due to stress relaxation. Changes in cell numbers in the rabbit GTs and SDFTs after 1 d and after 7 d compared to their corresponding controls. Data are derived based on Eqn. 6.4 and are displayed as the mean ± SD (n=4). Significant differences were analysed by 2-sample t-test. *$P < 0.05$.

Figure 6.20. H&E-stained GT and SDFT. Optical images of rabbit GTs and SDFTs treated with 1-d and 7-d stress relaxation from H&E staining. A control image of each group is displayed in the 1st column. The collagen matrix displaying the usual wavy crimp pattern was stained pink, and the cell nuclei were stained purplish blue. Representative regions of neovascularization (2nd column) and inflammation (3rd column) of the tendon FM are displayed for each experimental group. Neovascularization (marked with white arrows) and inflammatory cells including macrophages (marked with yellow arrows), heterophils (marked with blue arrows), and lymphocytes (marked with green arrows) could be observed. Scale bars are 50 μm.

Figure 6.21. Quantification of vascularity alterations due to stress relaxation. Changes in vascularity level of the rabbit GTs and SDFTs after 1 d and after 7 d compared to their corresponding controls were quantified based on Eqn. 4. Data are displayed as the mean ± SD (n=4). Significant differences were analysed by 2-sample t-test. *$P < 0.05$.

Figure 6.22. Illustrative image showing the cross-section microstructure/components including the collagen fibre, FM, IFM, and paratenon.

List of Tables

Chapter 1: Introduction

Congenital clubfoot or congenital talipes equinovarus (CTEV) shown in Figure 1.1 is a complex paediatric foot deformity. It consists of four complex foot abnormalities with varying degrees of rigidity, namely midfoot cavus, forefoot adductus, hindfoot varus, and hindfoot equinus (1,2). The incidence is widely reported as 1 in 1000 live births in the United Kingdom with males being affected about twice as often as females (1,3). In almost half of affected infants, both feet are involved. To date, the causes of clubfoot are poorly understood and regarded as idiopathic, however genetic factors and associated conditions such as spinal bifida, cerebral palsy, and arthrogryposis have been reported (1,3,4).

Figure 1.1. Illustrative image of bilateral clubfeet in a new-born infant. Image provided by C. Lavy, NDORMS, University of Oxford.

If left untreated, clubfoot inevitably leads to significant long-term disability, deformity, and pain (2). Although various surgical techniques including soft tissue releases and arthrodesis are used to correct clubfoot, currently conservative management is the preferred option. Some surgical techniques have been shown to pose a greater risk of pain, avascular necrosis, infection, over-correction, poor long-term ankle range of movement, weakened mechanical strength, and arthritis than if treated conservatively (5–10). Interestingly, some studies have also reported a correlation between the extent of release surgery and degree of functional impairment (7). To date, surgical options are mainly employed to manage resistant cases, recurrence or if unable to achieve complete correction of the deformity.

Currently, the optimal treatment utilizes the Ponseti method developed by Ignacio Ponseti in the 1940s (6,11). This technique consists of two distinct stages of manipulation and maintenance. The manipulation phase involves identifying the head of talus via palpation, supinating the forefoot to eliminate the cavus deformity, and abducting the forefoot. This manipulation is then followed up by application of a plaster cast, holding the foot in the corrected position, and providing sufficient time

for soft tissue remodelling. This manipulation-casting sequence is repeated on a weekly basis for an average of six weeks until a 50-degree abduction of the foot around the tibia is achieved. An Achilles tenotomy may then be required to eliminate any residual equinus and is followed up by three weeks in a cast to aid healing (1,6,11–13). The maintenance phase then involves holding the foot in an abduction brace for 23 hours per day for 3 months, helping to reduce recurrence rates (12,13). Zionts *et al.* (14) reported that due to the increased use of Ponseti method, the estimated percentage of clubfoot treated with surgical release has dropped from 72% in 1996 to 12%.

Due to the deformities, the dimension, structure, and mechanical properties of most soft tissues in a clubfoot are different to those of a normal foot. The presence of shortened, thickened, and fibrotic tissues at the medial and posterior aspect of the clubfoot was reported in several studies (15–17). These abnormalities include thickening and shortening of the posterior tibial tendon, Achilles tendon, tibionavicular ligament (deltoid ligament), and plantar calcaneonavicular ligament. In addition, a fibrous matrix was also seen in the posterior fibulotalar and deltoid ligaments. Masala *et al.* (18) investigated the difference in mechanical properties of Achilles tendon between a clubfoot and a normal foot by real-time sonoelastography.

The result shows lower mean elasticity values from the Achilles tendons of the clubfeet compared to normal feet (unilateral clubfoot patients), demonstrating that the Achilles tendon is softer in a clubfoot. However, little is known regarding the microstructural integrity of a clubfoot tendon after treatment of Ponseti method. The current evaluation of the outcome of Ponseti method is based on clinical examinations and functional parameters including Pirani score, Dimeglio scale, gait analysis, isokinetic muscle strength, and Kinematic variables (19–23). Several studies applied radiography to probe the correlation between radiologic angles of the foot and the functional results (24–28), but these studies were unable to image the abnormal tendons and ligaments in a clubfoot. Chandirasegaran *et al.* (29) measured the length and thickness of the Achilles tendon of a clubfoot treated with Ponseti method by ultrasonography, and discovered positive correlation between tendon lengthening and hindfoot correction, which suggests that tendon lengthening is an indicator of clubfoot correction. Although ultrasonography (29,30) is capable of macroscopically imaging tendons and ligaments in the foot, it fails to reveal microscopic details and changes of tendons and ligaments due to Ponseti manipulation. In short, despite being recognized as the gold standard treatment for clubfoot, the influence and effect of the Ponseti manipulation/casting on the microstructure of tendons and ligaments remain unknown.

Furthermore, the average casting period between manipulations (~1 week) of Ponseti method, which adds up to approximately six weeks for the whole treatment, makes practicing Ponseti method challenging in low resource countries (31–34). As traveling from home to a clinic can be inconvenient, costly, and time-consuming, many clubfoot patients failed to follow through the entire treatment. It has been shown that the success of Ponseti method relies heavily on the attentive participation and abiding commitment from the family of the patient (35), and that any temporary discontinuation and/or delay of scheduled casting may result in increased number of casts required and higher rate of recurrence (32,36,37). Therefore, recent studies have focused on accelerated Ponseti protocols which utilized a shorter cast change interval (38–40). A shortened cast duration is likely to help reduce the number of visits to the clinic, which may consequently lower the 'drop-out' rate. However, there is no scientific evidence supporting an accelerated protocol in these clinical studies, and thus the optimal cast change interval remains inconclusive.

The aim of this work is to (I) model the mechanical effect of a standard Ponseti manipulation/casting on a tendon tissue, (II) discover the changes of tendon

microstructures due to this mechanical treatment, (III) probe the mechanism behind the Ponseti method, (IV) investigate the role of elastin (an extracellular matrix (ECM) protein responsible for the recoil properties of an elastic tissue) in tendon stress relaxation, and (V) study the biological response to the treatment using an animal model to hopefully acquire supportive results for an accelerated Ponseti protocol and suggest additional examinations focused on tendon microstructural integrity other than functional parameters post-treatment.

Chapter 2: Literature Review

2.1 Introduction

A standard Ponseti method involves a series of manipulation and castings. During the manipulation process, the foot is slowly brought to a corrected position at which the soft tissues primarily at the medial and posterior side of the foot will be stretched to a certain strain value. The cast applied afterwards ensures this corrected position or this strain is well-maintained for tissue remodelling to take effect before the next manipulation/casting. The soft tissues responding (or resisting) to a Ponseti stretch include: (I) skin, (II) capsules and (III) tendons & ligaments. To investigate the main tissue that is restricting the foot from reaching the corrected position during stretching, the stress values generated from the skin (σ_{skin}), capsules (σ_{cap}) and tendons & ligaments (σ_{TL}) due to the mechanical stretch are required. To date, the stress values and elastic moduli (E_{skin}, E_{cap} and E_{TL}) of these soft tissues in a clubfoot in response to stretching via the Ponseti method have not been studied.

The general constitutive stress-strain relation can be described with Eqn. 2.1:

$$\sigma = E \cdot \varepsilon \qquad \text{(Eqn. 2.1)}$$

By calculating the product of the Young's modulus of the tissue and the strain value produced by the stretch, the stress value required for manipulation can be acquired. A single stretch from a manipulation and casting causes different strain values (ε_{skin}, ε_{cap} and ε_{TL}) in each tissue. Typically, ε_{skin} and ε_{TL} will have approximately the same value, while ε_{cap} will be much smaller than ε_{skin} and ε_{TL} in any given stretch; hence, here we consider only ε_{skin} and ε_{TL} in our calculation. The Young's moduli of human tendons & ligaments and human skin at the ankle from existing studies are listed in Table 2.1. It is worth noting that the approximately 10-fold difference between the modulus of the calcaneal tendon, which is also known as the Achilles tendon from Liao *et al.* (43) and from Kongsgaard *et al.* (44) was likely due to the difference in testing methods, the embalming treatment, and the age & condition of the tendons. Liao *et al.* (43) measured the modulus via *in vitro* tensile testings, while Kongsgaard *et al.* (44) adopted the ultrasonography for strain measurements together with indirect estimation of the *in vivo* tendon tensile force derived from the measured plantarflexor torque. In addition, Liao *et al.* (43) reported significantly lower modulus values in all four tendons and ligament caused by the treatment of Thiel embalming compared to the non-treated tendons. Lastly, tendons from Kongsgaard *et al.* (44) were from young

male athletes which were more likely to have stronger mechanical properties than those from Liao *et al.* (43) which were derived from old cadavers.

Table 2.1. Elastic Moduli of different human tendons, ligaments, and Skin.

Soft Tissue Type	Source	Test Method	Young's Modulus (MPa)	Ref.
Human Ankle Tendons & Ligaments	Plantaris Tendon	*in Vitro* Tensile	1.24×10^3	(41)
	Anterior Tibialis Tendon	Ultrasonography	$0.45 - 1.2 \times 10^3$	(42)
	Peroneus Longus Tendon	*in Vitro* Tensile	$1 - 5 \times 10^2$	(43)
	Peroneus Brevis Tendon	*in Vitro* Tensile	$1 - 4 \times 10^2$	(43)
	Calcaneal Tendon	*in Vitro* Tensile	$0.5 - 3.5 \times 10^2$	(43)
	Calcaneofibular Ligament	*in Vitro* Tensile	$0.7 - 4.5 \times 10^2$	(43)
	Achilles Tendon	Ultrasonography	2×10^3	(44)
	Deltoid Ligaments	CT, MRI, and Finite Element Modeling	$0.45 - 2.7 \times 10^3$	(45)

	Medial Collateral Ligaments	*in Vitro* Tensile	$0.99 - 3.2 \times 10^{2}$	(46)
	Lateral Collateral Ligaments	*in Vitro* Tensile	$2.16 - 5.12 \times 10^{2}$	(46)
Human Skin	Neck	MRI and Finite Element Modeling	~ 2	(47)
	Breast	Suction Cup Method	$2 - 4.8 \times 10^{-1}$	(48)
	Arm	*in Vivo* Tensile (extensionmeter)	$1.3 - 6.57 \times 10^{-1}$	(49)
	Arm	*in Vivo* Indentation	$4.5 - 8 \times 10^{-3}$	(50)
	Arm	*in Vivo* Indentation	$\sim 8.5 \times 10^{-3}$	(51)
	Foot	Ultrasound Palpation	$0.6 - 1 \times 10^{-1}$	(52)

As the Young's Moduli of the tendons (lowest: 50 MPa) are larger than those of the skin (highest: 2 MPa) with almost similar tissue-fulcrum distances, larger stresses (or resistance) will be generated from them during the Ponseti Method, meaning tendons and ligaments are the rate-limiting soft tissues in this treatment. After a session of manipulation/casting, how the tendon tissue responds or adapts to the tensile stress

before the next manipulation is a critical question. Both material stress relaxation and biological tissue remodelling would contribute to this process.

2.2 Tendon Structure & Composition

2.2.1 Structure of Tendon and Ligament

Tendon is a highly ordered composite material composed of various types of proteins. Although approximately 55-70% of its total weight is composed of water, the tissue exhibits high tensile strength in a healthy state (53–55). This strong mechanical characteristic is contributed by the well-organized collagen fibres aligned to the load axis which also provides the tissue with anisotropic properties (56–59). In terms of cellular elements, 90-95% of the cells in a tendon are tenoblasts and tenocytes, and the rest are chondrocytes at the entheses and a few synovial cells in the synovial tendon sheath (53).

Tendons are often grouped with ligaments rather than muscles due to their similarities in composition. For example, in an anterior cruciate ligament (ACL) reconstruction surgery, a patellar tendon or a four-head hamstring tendon can be used as an autograft (60,61). Although a tendon and a ligament have similar structures and compositions,

they are not completely identical. A ligament connects bone to bone and helps the formation of a joint. It holds the structure in place and prevents excessive or undesirable joint motion; on the contrary, a tendon helps facilitate joint motion. In addition, the forces transmitted by tendons are generally uniaxial, whereas for ligaments, which also possess high tensile strength, the forces can be transmitted in multiple directions depending on the motion of the associated joint (62–65).

2.2.2 Collagen

Collagen composes 60-85% of a tendon's dry weight (66). For all the collagen types in a tendon, 60-80% is collagen I, 0-10% is collagen III, and about 2% is collagen IV. There are also small amounts of collagens V, VI, and other types present in the tissue (53,54,67). Collagen in both tendon and ligament displays a hierarchical structure (55,63) shown in Figure 2.1. Briefly, starting with collagen triple helix molecules as the basic unit, they arrange themselves in a staggered configuration to from tropocollagen molecules. These collagen molecules (sub-fibril) then assemble to form collagen fibrils in an array which creates a periodic striation known as the 'D-spacing' (~67 nm) along the long axis (68–70). The fibrils are formed and stabilized by covalent crosslinking. An extracellular enzyme, lysyl oxidase, deaminates lysine and

hydroxylysine on collagen to produce aldehyde groups, which eventually covalently bonded with each other to form crosslinks (71,72). The collagen molecule is believed to have a length of 4.46 times D-spacing (~300 nm) and a diameter of ~1.5 nm (55,69). Collagen fibrils display a diameter of 50-500 nm and a length up to a few millimetres. Multiple fibrils then come together to form collagen fibres (1-20 um) by crosslinking macromolecules such as proteoglycans. At the next hierarchy level, fibres are bonded together to form fascicles (20–200 µm) (69,70,73–75) which can assemble to form the bulk tissue. In a tendon, collagen fibrils and fibres are aligned parallel to the long axis of the tendon, whereas in a ligament, the fibrils and fibres are not all strictly aligned to the long axis but interlace each other at small angles (20-30°) (63).

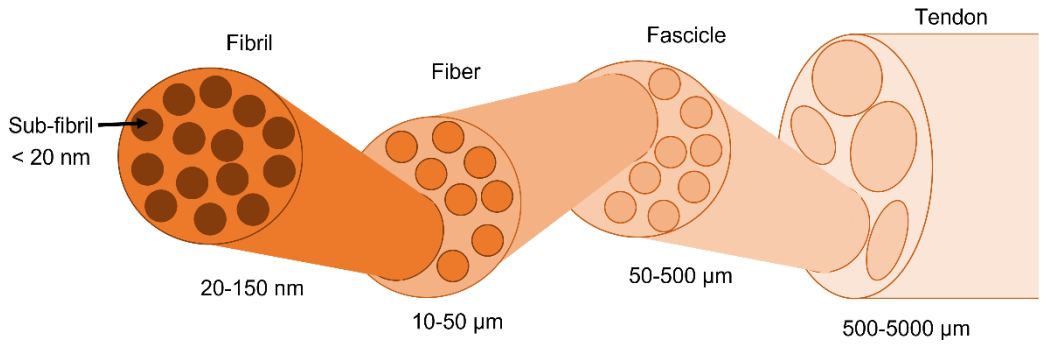

Figure 2.1. The schematic illustration of the structural hierarchy of a tendon displaying multiple units at different scales (fascicle, fibre, fibril & sub-fibril).

2.2.3 Ground Substance

Ground substance in a tendon or a ligament refers to water, proteoglycan, and glycoproteins. These materials intersperse between collagen fibrils, fibres, and fascicles (55,65,76). Generally, ligaments have a higher portion of ground substance than tendons (77).

Proteoglycans, which are the most abundant ground substance in tendons and ligaments, are considered a specific subset of glycoproteins (55). The general structure of proteoglycan consists of a core protein with one or more polysaccharide chains being covalently attached to it (55,78,79). Commonly referred as glycosaminoglycan (GAG), these polysaccharide chains are negatively charged and are responsible for drawing the major amount of water (up to 50 times by weight) (78) which accounts for 65-75% of the tissue wet weight (65). GAGs are non-branched polysaccharide chains composed of repeating disaccharide units. The unit is a uronic acid connecting to an amino sugar by a glycosidic bond (80–83). Due to the repulsion force generated by the charges and the high water content, proteoglycans provide the tissue with strong compressive resistance and enable collagen fibres to glide over each other (65,84). They also allow the molecule transportation and cell migration within the ECM (78).

2.2.4 Elastin & Elastic Fibres

One of the non-collagenous ECM components whose specific role in a tendon is not well-understood is the elastic fibre. These elastic fibres are composed of fibrillin-rich microfibrils surrounding a core of elastin which accounts for approximately 90% of the fibre volume and 1-2% of the whole tendon dry weight (78,85). The elastin protein, which possesses incredible flexibility and extensibility (almost 1000 times more than collagen), is present predominately in extensible tissues including lungs, blood vessels, ligaments, tendons, skin, and elastic cartilages (86,87), providing these tissues the ability to deform under physiological loading and recover back to the original state when the load is removed (i.e., reversibility) (88). The low modulus of elasticity and high resilience of elastin, allows elastic fibres to complement the collagen fibrillary tensile strength (89).

The process responsible for the formation of functional elastin within the elastic fibre is known as elastogenesis. Within the cell, the tropoelastin monomer is produced from expression of the elastin gene. These intracellular tropoelastin monomers associate with the elastin binding protein and are later secreted to the cell surface (90,91) at which they aggregate by coacervation to progressively become larger spherical

globules (92). The tropoelastin coacervates were then deposited onto microfibrils which is believed to function as a scaffold to direct tropoelastin crosslinking and consequential elastic fibre formation (93–95). Crosslinking is facilitated by the enzyme lysyl oxidase, which deaminates lysine side chains in tropoelastin to form allysine sidechains that can subsequently react with adjacent allysine or lysine side chains to form crosslinks (96). These crosslinks can then further react to form desmosine and isodesmosine crosslinks between tropoelastin molecules. Multiple crosslinks result in the mature insoluble elastic fibre (96,97).

Studies of elastin have generally focused on the cardiovascular system, lung, and skin tissue (98–103). In the case of an artery, both the collagen and elastic fibres appear undulated and wavy without loading. Under physiologic pressures or loading, most elastic fibres and less than 10% of the collagen fibres are straightened (104). As the stress increases, more collagen fibres are recruited, producing a nonlinear (J-shaped) stress-strain profile (98,100). Similarly, in the skin, although collagen fibres are known to be the main load-bearing component, the elastic fibres are responsible for the mechanical response at low stress and strain values and the retractability of the tissue (101). In a tendon, a unique wavy pattern called 'crimp' can be spotted on the collagen

fibres. During tension at low strain (~2-4%), which is known as the 'toe' region, the crimp pattern will be gradually flattened as the fibres collectively become straightened due to stretching. Although the organisation and the origin of fibril crimp is a highly debated topic. Some studies have suggested that elastin could be responsible for maintaining fibril crimp (77,105,106). However, the studies on elastin or elastic fibres in tendons are limited and inconclusive (107–109).

2.3 Tendon Mechanical Properties

2.3.1 Stress-Strain Profile of a Tendon

A typical stress-strain curve for a tensile test on a tendon is demonstrated in Figure 2.2. The graph shows three distinct regions (110,111). Initially, the collagen crimps are stretched out, and increasing number of collagen fibres and fibrils become aligned to the loading axis. This region is known as the 'toe' region, and it normally extends to approximately 2% elongation (111). The toe region lies within the elastic limit and thus the tissue will return to its original length when unloaded. Further straining brings the tissue into the 'linear' region which exhibits a constant Young's modulus. The stress-strain response mainly comes from elongating the collagen fibres and fibrils. Further straining induces plastic deformation by inter-fibrillar and inter-fibre sliding

and consequently the tissue does not return to the original length and structure after unloading. In the last region (yield & failure region), in which macroscopic defects occur, yielding begins as the slope of the curve decreases, with inevitable tissue failure occurring with further load (110,111).

In a Ponseti treatment, the stretch caused by manipulation aims to produce sufficient plastic deformation in the tendons to encourage tissue remodelling and lengthening. This deformation should lie within the early part of the linear region (red bracket in Figure 2.2), as excess deformation would risk entering the yield & failure region and deficient deformation would prove ineffective.

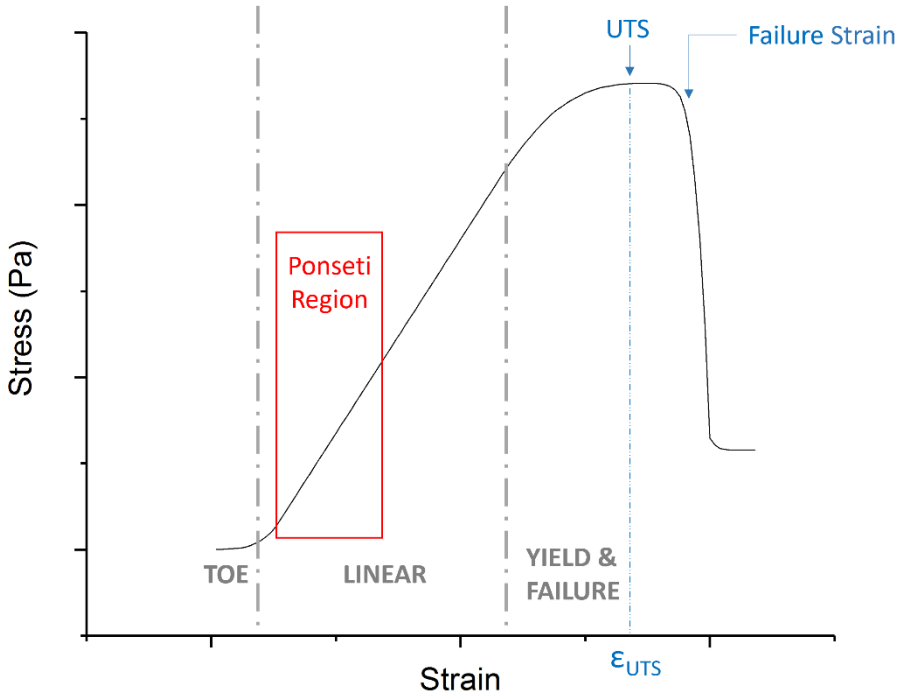

Figure 1.2. A typical stress-strain curve of a tendon. The J-shaped curve shows three distinct regions. The 'toe' region involves uncrimping of collagen fibres controlled by elastin; the linear region, which is the region at which the Ponseti method targets, is the physiological upper limit of tendon strain whereby the collagen fibrils orient themselves in the direction of tensile mechanical load; and the yield & failure region is where micro-damage continues to accumulate and the intramolecular crosslinks between collagen fibres fail, causing the stiffness to decrease and the tendon to fail.

2.3.2 Viscoelasticity

A tendon displays a time-dependent mechanical behaviour known as viscoelasticity, which means it possesses both elastic and viscous properties (112). Due to this behaviour, the tissue displays several characteristics: strain rate dependency, hysteresis, creep, and stress relaxation.

The mechanical response of the tissue is dependent on the strain rate. In general, a faster loading results in a higher elastic modulus (113–116), as typically exhibited by polymers. The increase in ultimate tensile strength (UTS)/failure stress and decrease in strain at UTS (ε_{UTS})/failure strain with increased strain rate were also reported (Table 2.2) (117–119). Pioletti *et al.* (120) demonstrated that the bovine ACL displayed higher stresses and elastic moduli when stretched under higher strain rates (0.1, 1, 5, 10, 20, 30 and 40%/s). Woo *et al.* (121) and Danto *et al.* (113) also studied this effect under wider ranges of strain rates on medial collateral ligaments (0.011-222%/s) and rabbit patellar tendons (0.016-135%/s), respectively, and both showed the same positive correlation between elastic modulus and strain rate. According to the results from Bonner *et al.* (117), a logarithmic relation between elastic modulus and strain rate is discovered (Figure 2.3), i.e., the dependency becomes less significant as the strain rate increases.

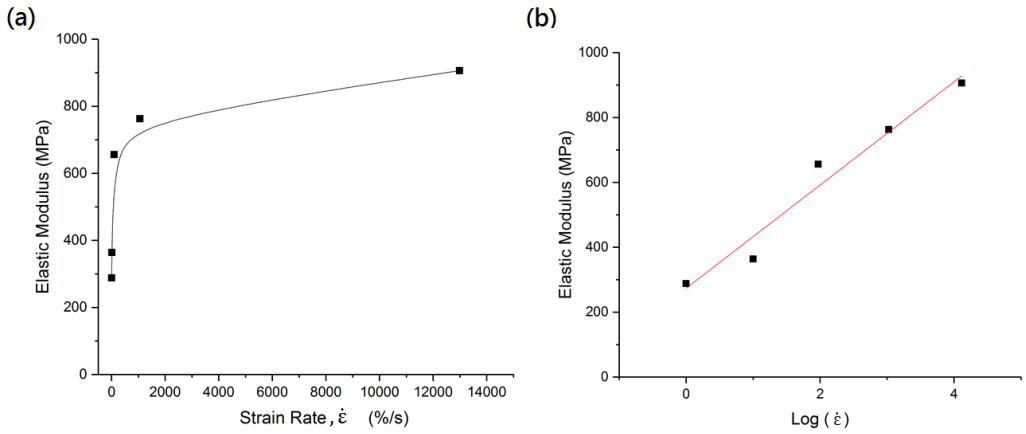

Figure 2.3. The relationship between tendon elastic modulus and strain rate. The plots were made using the data adopted from Bonner et al. (117). (a) Elastic modulus plotted against strain rate; (b) Elastic modulus plotted against the logarithm of strain rate. A logarithm relationship was found between modulus and strain rate.

Table 2.2. Existing work demonstrating the strain rate dependency of tendons and ligaments.

Source	Strain Rate (%/s)	Elastic Modulus (MPa)	UTS (MPa)	ε_{UTS} (%)	Ref.
Human Achilles Tendon	10	401.1	73.3	25.2	(118,119)
	100	544.7	81.3	21.0	
Source	Strain Rate (%/s)	Elastic Modulus (MPa)	Failure Stress (MPa)	Failure Strain (%)	Ref.

Porcine Lateral Collateral Ligament	1	288	39.9	17	(117)
	10	364	56.5	18	
	94	656	72.8	14	
	1060	763	75.9	11	
	12990	906	77.4	9	

When a tendon is strained, the energy stored during loading is more than the energy lost during unloading, i.e., the area under the loading curve is larger than that under the unloading curve. This feature on the curve, which represents the energy lost as a result of a non-conservative or dissipative process, is known as hysteresis loop (112,122). Under repetitive loading-unloading, the stress-strain curve of each cycle will be dissimilar until approximately 10 cycles (77). The size of the hysteresis is believed to be relevant to locomotion efficiency (123) and the risk of thermal damage (124,125). A creep describes the continuous increase in strain or deformation under constant loading force. The shape of the deformation-time curve during a creep test is believed to be dependent on the loading history (loading force, loading rate and force increments) (126,127). Wren *et al.* (128) reported that the time to failure decreases with increasing applied stress and increasing initial strain.

A stress relaxation, demonstrated in Figure 2.4, describes the continuous decrease in stress over time under constant strain. The relaxation rate of the stress is believed to be faster with a higher initial stress (129–131). Under different strain rates applied to reach the initial strain, the tendon will display different relaxation profiles. With a higher strain rate, the corresponding peak stress will be higher, resulting a faster relaxation (126,132). More details about stress relaxation will be discussed in the next section.

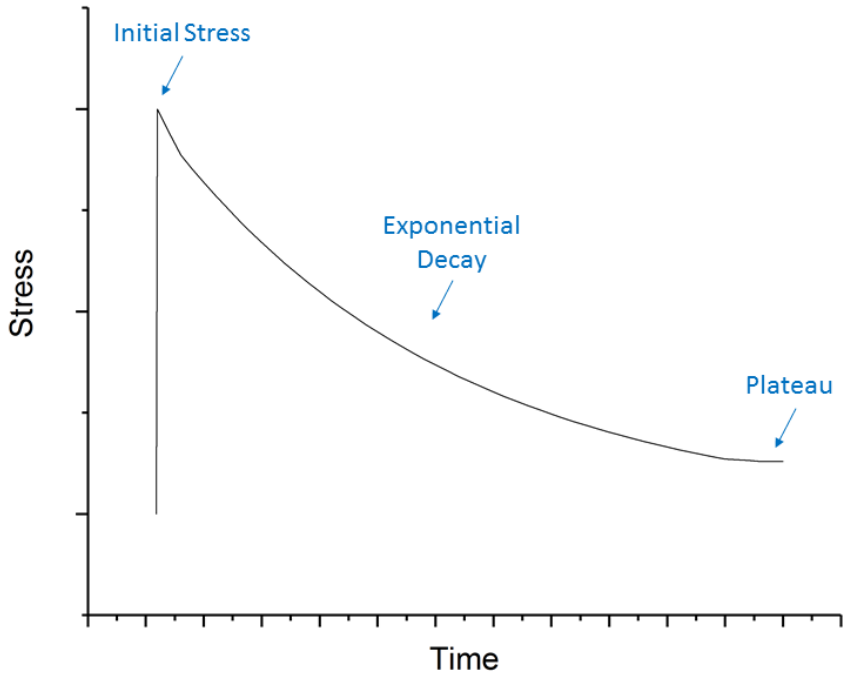

Figure 2.4. A typical stress-time curve of a single stress relaxation.

2.4 Stress Relaxation and Tissue Remodelling/Adaptation

It is worth highlighting that stress relaxation is the main event in a Ponseti method. As the clubfoot is held at an improved position by casting after manipulation, a constant strain or deformation is applied, and consequently stress relaxation occurs in the strained soft tissues. During this process, both the (I) material stress relaxation and (II) tissue remodelling/adaptation take place and both events are responsible for the shape of the relaxation curve.

Regarding the first event, existing *in vitro* studies on stress relaxation have focused on the microstructural changes of collagen units (i.e., fibrils, fibres, and fascicles) including reorganization, sliding and relaxation of each unit (129,133,134). Screen *et al.* (134) reported that reacting to a constant strain, the collagen fibres predominantly dissipate the stress through inter-fibre sliding compared to fibre relaxation, especially in lower stain values. When tested in higher strains, the percentage of fibre relaxation increases, indicating fibril level sliding/reorganization is adopted. The non-collagenous components of the tendon matrix, particularly proteoglycans (PGs) and glycosaminoglycans (GAGs), are generally believed to play an important role in viscoelasticity and stress relaxation. Legerlotz *et al.* (135) showed that the removal of

GAGs by chondroitinase in a tendon lead to more stress relaxation. The tendons from mice with knockouts of decorin, the major PG in a tendon, also show increased stress relaxation (136), relaxation rate (137) and reduced strain rate dependency (138). However, the roles of other important non-collagenous components such as elastin or elastic fibres in tendon viscoelasticity and stress relaxation remain unclear. While elastin digestion by elastase on tendon results in lower ultimate tensile stress and failure strain with no change in elastic modulus (139), no work has focused on the effect elastin removal on stress relaxation. At the same time, recognizing these microstructural deformations, tissue remodelling causes subtle growth of the tissue which would also contribute to the stress relaxation. The existing mechanical work of *in vitro* stress relaxation on tendons cannot examine the effect of tissue growth but only the microstructure rearrangement. It is thus reasonably to predict that the *in vivo* stress relaxation during a Ponseti stretch would be faster than the *in vitro* tests.

Unlike synthetic materials, a biological material like the tendon is capable of adapting to chemical and physical stimuli (140). The tenocytes in a tendon, which express a fibroblastic phenotype, are responsible for responding to stimuli by producing growth factors (141), synthesizing collagen and other matrix components of the ECM (142),

and remodelling old ECM by releasing matrix metalloproteinases (MMPs) (143). Mechanical loading or straining are a key stimulus which generates a series of signals responsible for maintaining, repairing, and modifying the ECM in a tendon. Fibroblast proliferation, morphology, alignment, and gene expression have been reported to be influenced by mechanical stimuli (144–149). In terms of ECM synthesis and remodelling, studies have shown that cyclic tension on fibroblasts can increase collagen type I and collagen type III mRNA expression (148,150,151). These changes cause the number, diameter, and concentration of collagen fibrils to increase (152,153), thus increasing the stiffness of the tissue (152,154). By contrast, compression loading is believed to induce the synthesis of (152,154) proteoglycans and type II collagen, and in some cases, a decrease in collagen type I (155–158). This change in composition results in the formation of fibrocartilaginous matrix (158,159). The adaptation of a tendon is dependent on the type of loading, strain magnitude, strain rate and number of cycles. It is worth mentioning that most existing studies on the effect of mechanical stretching on tissue remodelling focused mainly on short-term cyclic straining (145–151,160,161). Kalson *et al.* (162) studied the effect of static stretching on adaptation by slow stretching (0.25%/day) a tendon-like construct seeded with embryonic tendon cells for 4 days. The result shows increased collagen fibril diameter, fibril length, fibril

number, and mechanical stiffness. The increase in the collagen fibril length and number is a promising indication of tendon growth or lengthening which is expected and desired in the Ponseti treatment. On the other hand, under a long-term stress relaxation, the tissue response and adaptation could be different.

2.5 Summary

The Ponseti method, developed by Dr. Ignacio V. Ponseti in the 1940s, has been recognized as the gold standard treatment for clubfoot (6,11). However, the current outcome evaluation for the treatment is based only on clinical and functional parameters (19–23). A single manipulation and casting in the Ponseti method results in a long-term stress relaxation on the key resistant soft tissues in the clubfoot: tendons. The lack of knowledge regarding how these soft tissues respond and remodel according to a long-term stress relaxation provide us with no insight on the structural outcomes, thus inhibiting the development of additional outcome examinations focusing on tissue integrity and the improvement in the efficiency of Ponseti method.

Although a tendon is predominately composed of collagen fibres, non-collagenous components such as PGs, GAGs and elastin are also critical to the function and

mechanical behaviour of the tissue (107–109). Existing studies on tendon stress relaxation mainly focused on how collagen units react (sliding and reorganizing at different hierarchy levels) to dissipate stresses, and the roles of PGs and GAGs in stress relaxation (134,135). Composing only 1-2% of the whole tendon dry weight, elastin is a much weaker but more extensive material compared to collagen. Unlike collagen, which provides the tissue with the main tensile strength, elastin functions primarily in the physiological loading known as the 'toe region' by providing the tissue with flexibility and retractability (77,86,87,105,106). Although a few studies have explored the mechanical role of elastin in a tendon (107,139), minimum effort has been put in their contribution to the viscoelasticity of a tendon.

By observing the microstructural changes, particularly the elastin in a tendon after a long-term stress relaxation, the effect of a single Ponseti manipulation/casting can be studied. Understanding the role of elastin in tendon stress relaxation, may help us improve the Ponseti method and suggest additional examinations on tissue integrity after the treatment.

Chapter 3: Setup & Design of Tensile Testing and Strain-rate Dependency of a Tendon

3.1 Introduction

When a tendon is stretched, the collagen fibres begin to uncrimp once the mechanical profile enters the toe region. As the straining continues and reaches the linear region of the profile, more collagen fibres are recruited and aligned to the load axis, causing stress response to increase drastically. A Ponseti manipulation would gradually stretch the tendons and ligaments at the medial and posterior sides of the foot. A cast is then applied to maintain the corrected foot position, thus initiating stress relaxation in the tissues. To test this mechanical event on a tendon, a tensile testing setup must first be developed. Unlike the conventional solid materials, e.g., metals, alloys, etc., a tendon is a soft material that displays undesirable properties when being tested on a mechanical tester. To begin with, the wet and slippery surface of a tendon causes the biggest challenge for gripping the sample ends firmly using common grips and clamps (163). While insufficient compression between the grips would result in slippage of the sample, excessive compression would inflict damage or rupture close to the gripping regions, causing premature yielding on these sample ends which produces unreliable mechanical results. To solve this issue, several clamp designs using self-

tightening clamp, sandpaper or other high friction surfaces have been proposed; however, slippage still occurs (164,165). Riemersa and Schamhardt (166) first proposed the solution for removing slippage by lowering the surface temperature at the gripping region using 'cryo-jaw' clamps. These freezing clamps have shown to grip the tendons up to a tensile load of 13800 N without the occurrence of slippage (166–169). However, this thesis aims to examine the effect of a Ponseti cast on the tendon, which would produce a stress relaxation lasting for almost a week. The requirement for long durations more than an hour for each test would make cryogenic clamps nonapplicable as the freezing effect from the clamp will creep towards the testing region over time. This temperature fluctuation within the tendon during testing is likely to alter the mechanical response recorded (170–172). Shi *et al.* (173) developed a polymeric serrated teeth to grip the tendon for tensile testing at room temperature. The teeth were designed as peak-to-peak instead of peak-to-valley, which reduced the risk of the expansion and creep of the tendon and was able to reduce the occurrence of slippage. From their results, the teeth were able to stretch bovine tendons to a maximum load of 6.87 kN. However, the compressed regions of the tendon by the clamp may produce higher stress concentration as seen in existing experiments (174,175); hence, additional measures must be applied to solve this issue.

Currently, there is no fixed criterion on how fast a manipulation of the clubfoot should be. As mentioned in section 2.3.2, tendon is a viscoelastic material (112), i.e., its mechanical properties are time time-dependent or rate-dependent. Several studies have explored the strain rate-dependency of Young's modulus (E) on a tendon. While in general, a faster loading would result in a higher elastic modulus (113–116), as typically exhibited by polymers, some studies did not observe this strain rate-dependency (176,177). Furthermore, loading at higher strain rates have been reported to show correspondence to a lower strain at ultimate tensile stress (UTS) (117,118). However, the strain rate-dependency of tendons has not been examined in a slow loading regime of the Ponseti manipulation.

In summary, this chapter aims to first experiment a gripping method for long-term tendon stress relaxation. 3D-printed acrylonitrile butadiene styrene (ABS) teeth-based clamps were made based on the design from Shi *et al.* (173) to allow firm grips without causing rupture on the gripping ends. Selective air-drying was performed on the gripping ends of the tendon to remove the slippery and compliant characteristics due to hydration. The viability of this new method was tested by comparing the engineering

strains derived from the grip displacement with the surface strain. This surface strain was measured from the displacement of ink markers on the tendon surface. Once a tensile testing setup was established, the strain rate-dependencies of the (I) Young's modulus and (II) strain at UTS (ε_{UTS}) of a young tendon were examined at five different strain rates.

3.2 Materials & Methods

3.2.1 Clamps Development & Sample Preparation

The design chart and the actual clamps were displayed in Figure 3.1. The 3D-printed serrated teeth can be inserted into the socket of the metallic piece. Each end of a tendon sample can be sandwiched between two serrated teeth and then be secured with screws before inserting into a tensile tester. The polymeric teeth were 3D printed using ABS by an uPrint SE Plus 3D printer (Stratasys) with each step of 0.25 mm of layer thickness. The dimension of a teeth piece is: 4.1 mm in bulk thickness; 1.6 mm in the thickness of the teeth part; 20 mm in width; and 32 mm in length. The metallic parts of the clamps, which were made of 304 stainless steel, were fabricated at the workshop in the department of Engineering Science, Oxford University.

Four-week-old Dutch Calf feet were obtained from a local abattoir. Deep digital flexor tendons (DDFTs) of the feet were extracted at their origins and insertions, and stored in -80°C. Before testing, DDFTs were selectively air-dried on both ends using plastic films (Figure 3.2), which left a 50-55 mm testing region in the centre, for secured gripping and failure prevention at the ends.

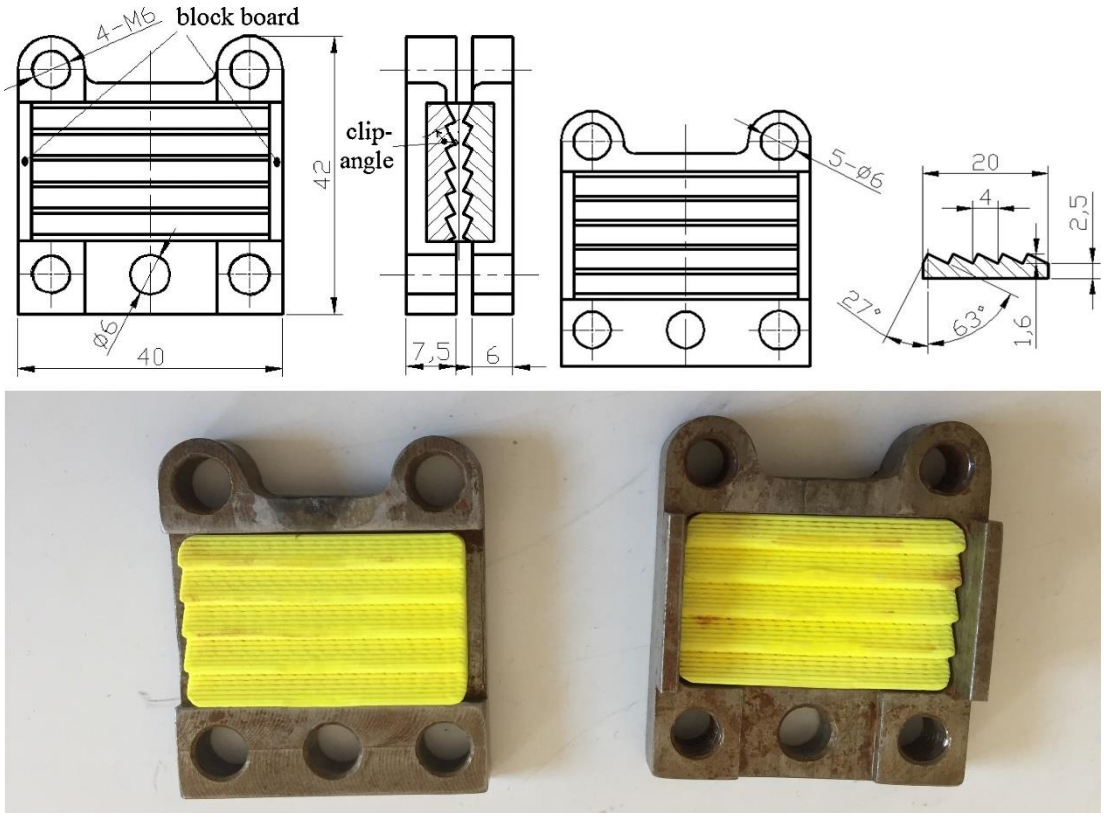

Figure 3.1. The design chart adopted from Shi *et al.* (173) (top) and the actual image (bottom) of the custom-made clamps consist of serrated ABS teeth and steel chambers.

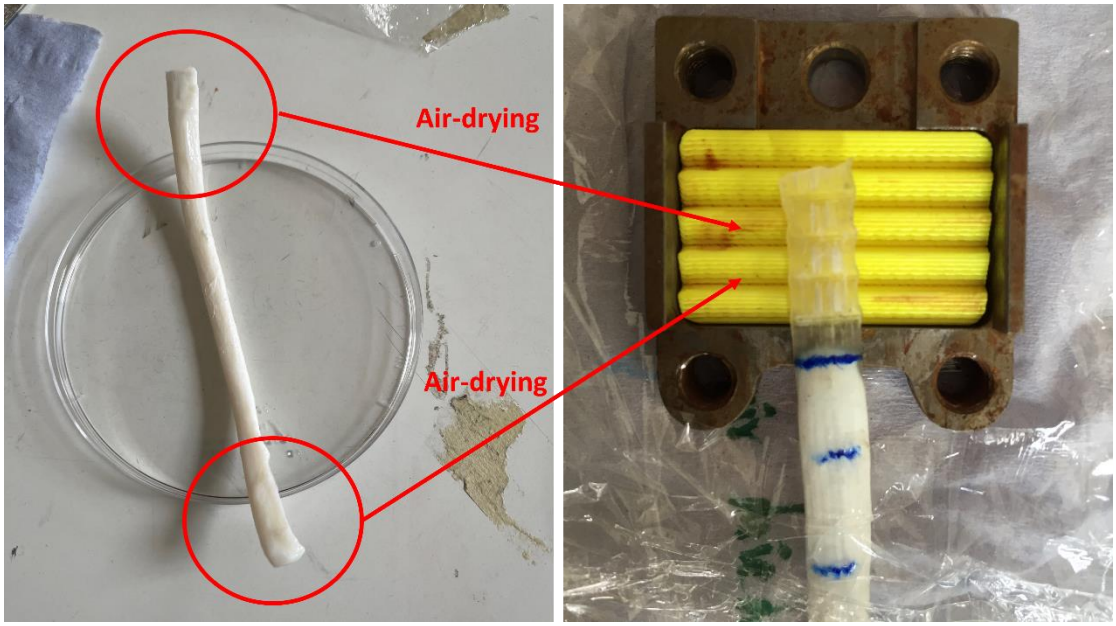

Figure 3.2. Illustrative images showing the changes of the tendon ends before (left) and after (right) selective air-drying. The tendon surface displays a yellow-ish colour and becomes stiffer after drying.

3.2.2 Tensile Testing and Strain Measurement

Once both ends of the tendon sample have been securely gripped with the clamps, the initial length (l_0) of the tendon (i.e., the hydrated sampling region) was measured before inserting into an Autograph AGS-X tensile tester (Shimadzu) with a 5 kN load cell. The engineering strain (ε_e) at any time during the test (t) was derived based on the grip displacement (l(t)) and l_0 using the following equation:

$$\varepsilon_e(t) = \frac{[l(t) - l_0]}{l_0} \qquad \text{(Eqn. 3.1)}$$

A permanent marker was used to create markings on the sampling (hydrated) region. Once the sample along with the clamps were inserted into the tester, a video camera

was used to record the displacement of the markers (d) over time during the tensile test as shown in Figure 3.3. The surface strain (ε_s) was then derived using Eqn. 3.2.

$$\varepsilon_s(t) = \frac{[d(t) - d_0]}{d_0} \qquad \text{(Eqn. 3.2)}$$

The cross-sectional area was acquired from the width and thickness of the sample measured with a calliper, assuming the cross-sections have an oval shape for all samples. The initial stroke position was set to be at ~0.1N of tensile force for each test. Tendon samples were stretched under a strain rate of 0.5%/s until 8%. The values of the engineering strain and surface strain acquired from Eqn. 3.1 & 3.2 over time were compared at the same time points by paired t-test.

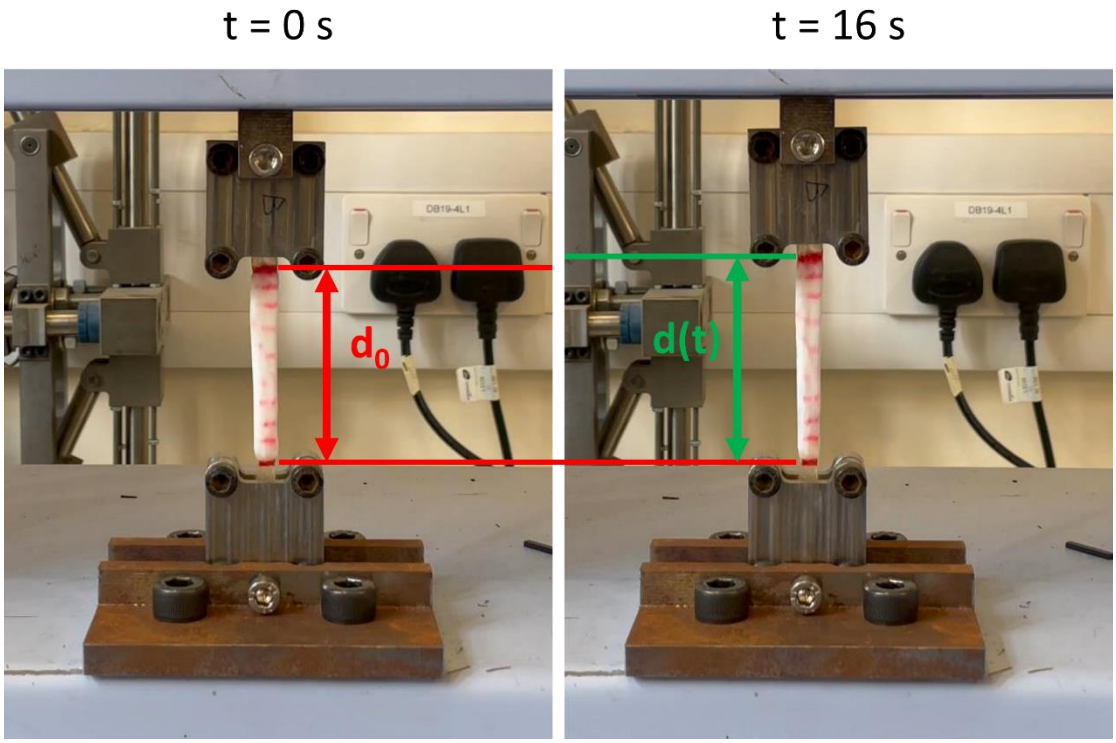

Figure 3.3. A demonstration showing the maker displacement (d_0 to d(t)) on the tendon surface before (left) and after 16 seconds of tensile testing (right).

3.2.3 Strain Rate-dependencies of Modulus and Strain at Ultimate Tensile Stress

Following the tensile testing setup and sample preparation mentioned in the previous sections, young DDFTs were tensile tested at 5 different strain rates using a tensile tester (DMG, 6160). Clinically, the manipulation of a clubfoot using the Ponseti method takes about 1-2 minutes to gradually move the clubfoot to a corrected position. Based on the estimated tendon strain of 7-10% produced by a single manipulation to correct adductus, which will be detailed in section 4.2.1, a Ponseti manipulation is likely to strain the tendon at strain rates between 0.05%/s to 0.17%/s. Hence, strain rates of (I) 1%/s, (II) 0.5%/s, (III) 0.1%/s, (IV) 0.01%/s, and (V) 0.001%/s were tested in this chapter. The initial stroke position was set to be at ~0.1N of tensile force for each test.

3.3 Results

3.3.1 Tensile Setup Applicability & Strain Measurement

The combination of the polymeric teeth and the selective air-drying successfully gripped the tendon sample until failure (Figure 3.4) without slippage and rupture at the gripped site. As shown in Figure 3.4, the reduced compliance due to drying also

ensured the occurrence of elongation and failure at the sampling region rather than the gripped region. Results from the surface strain measurement using markers as strain gauges were displayed in Figure 3.5. For all three tests (n=3), no statistical difference was found between the surface strain and the grip strain. The surface strain rate of each curve was also derived by linear fitting the ε_s-time curve as shown in Figure 3.5. A mean surface strain rate of 0.487±0.011%/s, which is similar to the grip strain rate of 0.5%/s.

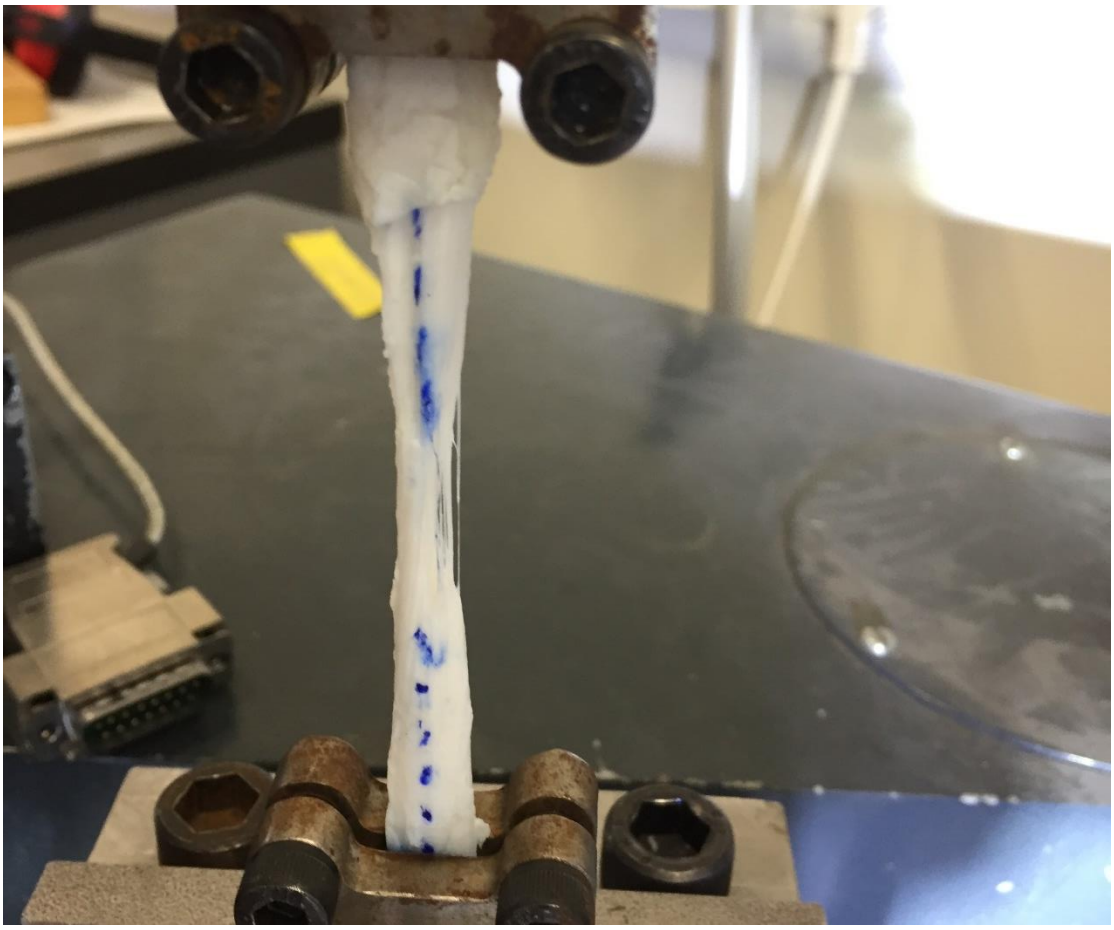

Figure 3.4. A demonstration of a tendon strained to failure. The tendon sample were prepared and gripped as mentioned in the method section. Failure occurred at the middle of the sampling region of the sample.

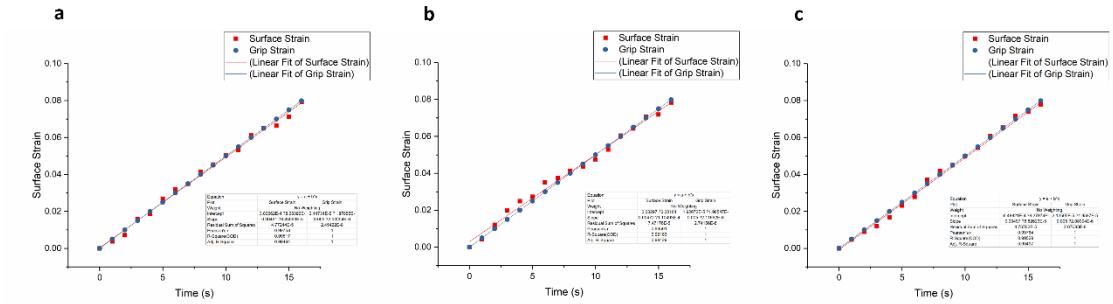

Figure 3.5. Comparisons of the values of the surface strain (red) and the grip strain (blue) plotted against testing time of 3 separate tests (a, b & c). Paired t-test found no difference between the two strains for all 3 tests. A linear fitting was conducted and displayed for each test.

3.3.2 Strain Rate-dependencies of Modulus and Strain at Ultimate Tensile Stress

Figure 3.6(a) shows the illustrative stress-strain curves of the tendons strained at 5 different strain rates. Higher stress responses can be observed from samples strained at higher rates, demonstrating a positive correlation. The Young's modulus and the ε_{UTS} were plotted against the logarithm of strain rate as shown in Figure 3.6(b) and 3.6(c). Strain rate-dependency could be observed in the Young's modulus as the strain rate began to decrease from 1%/s. From Figure 3.6(b), while decreased modulus could be seen in the curve, statistical difference only existed between strain rates of 100 times gap. By reducing the strain rate from 1%/s to 10^{-3}%/s, the modulus could be lowered approximately 4 times smaller. On the other hand, no association was discovered between strain rate and the ε_{UTS} (Figure 3.6(c)). Univariate linear regression was performed on the dataset of modulus vs the logarithm of strain rate, and the result

generated a linear fit with a slope of 89.8 MPa and an intercept of 321.1 MPa (red line in Figure 3.6(b)).

a

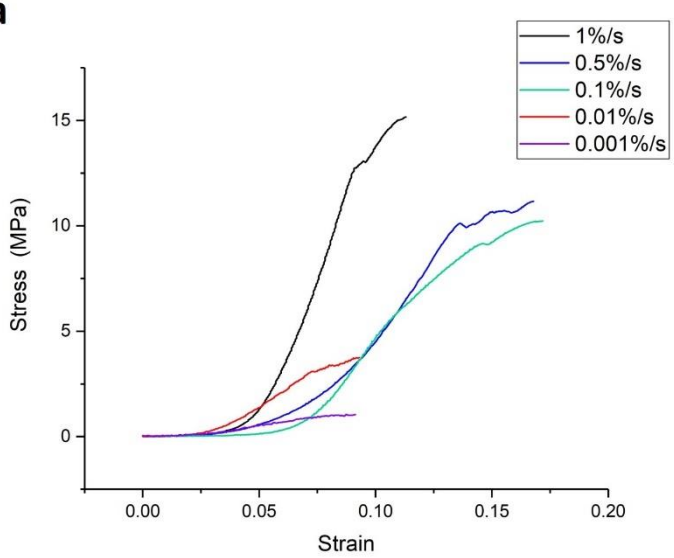
1%/s
0.5%/s
0.1%/s
0.01%/s
0.001%/s
Stress (MPa)
Strain
0
5
10
15
0.00
0.05
0.10
0.15
0.20

b

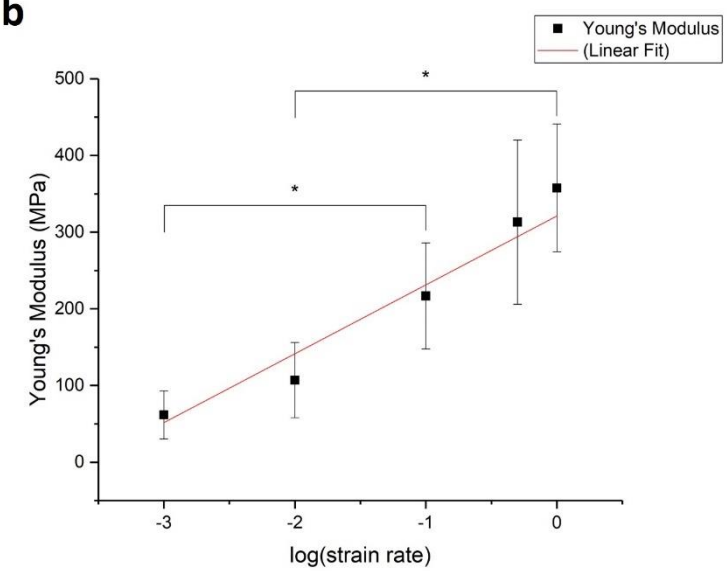
Young's Modulus
(Linear Fit)
Young's Modulus (MPa)
log(strain rate)
*
*
0
100
200
300
400
500
-3
-2
-1
0

c

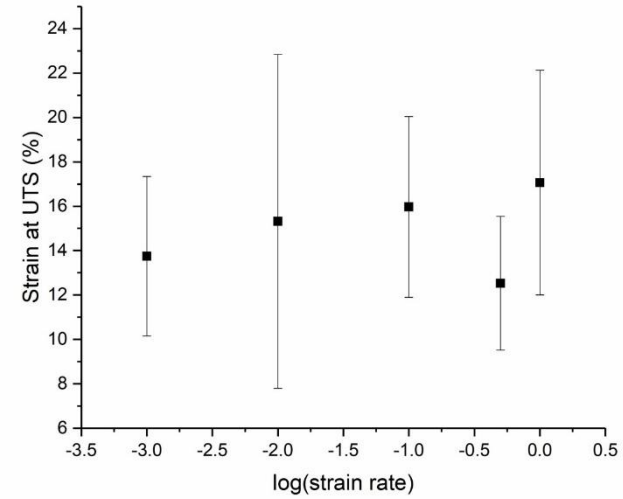
Strain at UTS (%)
log(strain rate)
6
8
10
12
14
16
18
20
22
24
-3.5
-3.0
-2.5
-2.0
-1.5
-1.0
-0.5
0.0
0.5

Figure 3.6. Mechanical results of the strain rate-dependency experiments. (a) Illustrative stress-strain profile of all 5 strain rates tested (1%/s, 0.5%/s, 0.1%/s, 0.01%/s & 0.001%/s), and the results of the strain rate-dependencies of the (b) Young's modulus and the (c) strain at UTS. Both data are plotted against the logarithm of the strain rate (%/s). Univariate linear regression ($y = a x + b$) was applied to (b), and the results generated a linear fit (red line) with a slope of 89.8 MPa and an intercept of 321.1 MPa with an R-Square of 0.93. All data are displayed as the mean ± standard deviation (SD) (n=3). *$P < 0.05$.

3.4 Discussion

Tensile testing on tendon tissues has been challenging based on several issues including slippage and rupture or compliance generated by gripping (163). Because of these complications, the results derived from tensile tests are often unreliable and inaccurate. To examine the effect of a Ponseti cast on a tendon, a mechanical setup capable of performing long-term stress relaxations on tendons is required. Although the cryogenic clamps have been widely used on tensile tests to produce viable results (166–169), this technique cannot be applied on a tensile test lasting more than several hours. Hence, a non-frozen clamp system was developed in this experiment. The polymeric serrated teeth adopted from Shi *et al.* (173) was designed to firmly hold the tissue to prevent slippage. Made of ABS, high compressive forces for gripping were allowed without the risk of rupturing the tendon due to the low stiffness nature of ABS, since the conventional metallic teeth are likely to create cuts on the tendon. To further limit slippage, drying on the gripped regions of the tendon was conducted, as hydration

is a main source of the tissue's slippery nature. In addition, dehydration also increased the stiffness of the tendon, which not only lowered the risk of rupture but also prevented high strain concentration occurring at the gripped region of the tendon.

To further examine the applicability of this gripping technique, the surface strain was measured and compared with the strain derived from grip displacement. If any of the complication mentioned above (e.g., slippage or high strain concentration at the gripped region) have occurred, the measured surface strain on the tendon would be smaller than the grip strain. Current methods of measuring strain of a tendon have used transducer-based systems, medical imaging, and strain gauges (178). The applications of transducer-based systems including liquid metal strain gauges (179–181), implantable force transducers (182,183) and Hall effect transducers (184–186) are complicated and hard to implement. Medical imaging techniques such as ultrasound (187,188), MRI (189), and fluorescent cell tracking (190) are expensive and time-consuming. Physical strain gauges when being attached to the tendon surface by suturing, gluing, etc. (191–193) may result in tissue damage or inaccuracy due to insecure attachment. In this experiment, the tendon strain was measured by monitoring the marker displacement. While this method is less sophisticated, for a relatively large

objective strain of 8%, the measurement errors are more tolerable. In addition, this study does not focus on local strain distribution but the overall engineering tensile strain; hence, a simplified marker-tracking method is reasonable and viable. The results from the strain measurement demonstrated matching strain and strain rate values between the surface and grip strains indicating a successful tensile test setup capable of producing reliable strain values based on grip displacement.

Strain rate-dependency of Young's modulus was found between 1%/s and 10^{-3}%/s within which the modulus would decrease as the strain rate was decreased. This observation is expected and matches the results from existing work (113–116). Bonner *et al.* (117) plotted the Young's moduli over logarithm of a wide range of strain rates (from 1%/s to 12990%/s), and discovered a linear relationship between them. This logarithmic association between the modulus and strain rate has also been observed in polymer materials (194–196). The use of a logarithm function was driven by the fact that mechanical properties of polymer systems are usually sensitive to the logarithm of the rate of loading (194–196). As a tendon is also a polymer material, a phenomenological dependence equation (Eqn. 3.3) for polymer materials adopted

from Richeton *et al.* (195) was applied to characterise the dependency of strain rate and modulus for the young bovine DDFTs. Eqn. 3.3 was displayed below:

$$\frac{E}{E_{ref}} = 1 + S \times \log\left(\frac{\dot{\varepsilon}}{\dot{\varepsilon}_{ref}}\right) \qquad \text{(Eqn.3.3)}$$

where E is the Young's modulus, E_{ref} is the reference value of the Young's modulus, $\dot{\varepsilon}$ is the strain rate, $\dot{\varepsilon}_{ref}$ is the reference value of the strain rate, and S is the strain rate dependency. From the univariate linear regression shown in Figure 3.6(b), a slope of 89.8 MPa and an intercept of 321.1 MPa were derived. Using these parameter values derived from linear regression with the chosen reference strain rate ($\dot{\varepsilon}_{ref}$) of 10^{-3}%/s and the corresponding reference modulus (E_{ref}) of 61.7 MPa, a strain rate dependency (S) value of about 1.46 was derived. Several models have been developed to probe the association between the mechanical properties and strain rate or temperature for polymers (197–202). Specifically, the phenomenological Eyring's model has been used to describe this association in polymers for decades (198,199). The Eyring's equation (198,199) was shown below:

$$\sigma_y = \frac{\Delta H}{V} + \frac{kT}{V}\left(\log\left(\frac{\dot{\varepsilon}}{\dot{\varepsilon}_0}\right)\right) \qquad \text{(Eqn. 3.4)}$$

where σ_y is the yield stress, ΔH is the activation energy, V is the activation volume, k is the Boltzmann constant, T is the temperature, $\dot{\varepsilon}$ is the strain rate, and $\dot{\varepsilon}_0$ is a constant pre-exponential strain rate. Considering the fact that yield stress is also a

mechanical property that is sensitive to strain rate, and the stress value could be derived from the product of modulus and strain, comparing Eqn. 3.3 with Eqn. 3.4 would provide insights for understanding the physical meaning of strain rate dependency. Like Eqn. 3.3, Eqn. 3.4 also consists of a logarithm of strain rate over a strain rate constant with a slope and an intercept containing energy and temperature terms. Through normalisation of the ΔH/V term (intercept), Eqn. 3.4 could be rewritten as:

$$\frac{\sigma_y \cdot V}{\Delta H} = 1 + \frac{kT}{\Delta H}\left(\log\left(\frac{\dot{\varepsilon}}{\dot{\varepsilon}_0}\right)\right) \qquad \text{(Eqn. 3.5)}$$

where the first term containing the yield stress becomes unitless. Thus, from Eqn. 3.3 and Eqn. 3.5, the strain rate dependency would be positively and negatively correlated to temperature and activation energy, respectively.

One theory for explaining the modulus strain rate-dependency is the dissipative theory derived by Ciarletta and Ben Amar (203). Ground substance, the key component for tendon hydration and inter-fibre force transfer, is thought to mediate interactions and create temporary interfibrillar bridges between collagen fibres during loading. When strained at relatively slow rates, the water and ground substance matrix are believed to have sufficient time to disperse and distribute forces, respectively, thus dissipating the stresses; when strained at higher rates, less time is given to the fluid to dissipate

through the ECM (204). Reduced strain rate-dependency was found in decorin-knockout mice (138). It is likely that the dissipative events also resulted from inter-fibre sliding and reorganization. Both Screen *et al.* (134) and Gupta *et al.* (129) reported that reacting to a constant strain, the collagen fibres predominantly dissipate the stress through inter-fibre sliding compared to fibre relaxation. As the strain rate increases, apart from the hindrance of fluid dissipation, the collagen fibres also have less time for inter-fibre sliding, causing higher percentages of tensile strain experienced by the fibres, which produces stiffer responses. This speculation is also supported by a study done by Clemmer *et al.* (204) in which higher levels of fibre elongation, larger portion of aligned fibres, and increased elastic modulus were seen in tendons strained at higher rates. Essentially, these microstructural events (i.e., fluid dissipation mediated by ground substance, inter-fibre sliding, and fibre relaxation) would occur during straining to dissipate stresses in the tendon matrix. As the strain rate decreases, the effect of stress dissipation is likely to become more significant, thus reducing the stress response and modulus. These microstructural events may also explain the lack of rate-dependency in ε_{UTS} in this study, which matches the findings from several existing studies (118,205,206). Additionally, both Bonner *et al.* (117) and Edwards *et al.* (207) also found no rate-dependency in failure strain on porcine

ligaments and tendons. This observation suggests that the incidence of failure during straining in a tendon is predominately controlled by the strain experienced by collagen units in the fibre or/and fibril hierarchies rather than stress, i.e., failure would occur when a certain fibre/fibril strain is reached no matter what stress value is produced. Straining at lower strain rates permits more time for inter-fibre sliding and fibre reorganization to take place before more fibres are being recruited during straining. Straining at higher rates would only result in higher fibre recruitment which generates a stiffer response, but the maximum strain experienced by the local fibres/fibrils is likely the same as that strained at lower rates (identical local maximum of strain); hence, only the modulus and stress display rate-dependencies. Clinically, as a lower strain rate would result in a lower modulus, suggesting a slower manipulation procedure in the Ponseti method could contribute to lower resistance from the foot.

3.5 Summary

In this chapter, a simple but effective tensile setup has been developed to solve the common issues spotted in tendon tensile testing. The use of polymeric teeth for gripping the tendon limits the risk of cutting when high compression is required to secure the sample. Selective air-drying removes the slippage complication caused by

hydration and the high strain concentration at the gripped sites. Through comparison between the grip strain and the surface strain derived by marker displacement, this new gripping setup has proved to be successful. Using this setup, the strain rate-dependencies of E and ε_{UTS} were experimented at 5 different strain rates. While no dependency was found in ε_{UTS}, lower E values were observed under lower rates. The result suggests the probability of minimizing resistance from the clubfoot by lowering the rate of the Ponseti manipulation procedure.

Chapter 4: The Effect of Time-dependent Stress Relaxation on Tendon Microstructure and Elastin

4.1 Introduction

A Ponseti manipulation would stretch the tendons at the medial and posterior sides of the foot. A cast is then applied to maintain the corrected foot position, thus initiating stress relaxation in these soft tissues. When a tendon is stretched, the collagen fibres begin to uncrimp once the mechanical profile enters the toe region. As the straining continues and reaches the linear region of the profile, more collagen fibres are recruited and aligned to the load axis, causing stress response to increase drastically. In physiological loading, a tendon is generally strained in the toe region where the tissue is able to recoil back its original state when the load is removed. This uncrimping and recoiling characteristic is commonly thought to be controlled by the elastin (77,105,106). In the case of a Ponseti manipulation, the tissue strain is believed to be in the linear region since the objective of each Ponseti cast is to permanently bring the foot to an improved position, thereby lengthening the tendon in the absence of loading. To achieve this goal, sufficient plastic deformation is required and is most likely accomplished in the linear region (208).

As a biological composite material, plastic deformation could occur in different components in a tendon including collagen fibres, elastin, and various types of ground substance. Tissue remodelling can then repair this micro-damage and restore normal tendon function through ECM degradation and synthesis. Examining the biological response may help us discover the plastic-deformed components in a tendon. Existing *in vitro* studies have shown that cyclic tension on tendon or ligament fibroblasts can increase collagen type I and collagen type III mRNA expression (148,150,151). Since a tendon is primarily composed of collagen, in order to adapt to tension and achieve tissue lengthening, the upregulation of collagen expression to produce more collagen fibres appears reasonable. Nevertheless, other ECM components may also be functionally and microstructurally altered. Gupta *et al.* (129) studied how a tendon structurally respond to stress relaxation at different levels of collagen unit and found out that inter-fibre sliding contributed more to stress relaxation compared to intra-fibre relaxation. The result suggests that other ECM components residing in the inter-fibre matrix (i.e., elastin and ground substance) play a key role in stress relaxation and are likely to be microstructurally altered or plastically deformed. How non-collagenous components such as elastin contribute to stress relaxation, and conversely how stress relaxation influence these components are critical questions for studying the Ponseti

method. In addition, present studies only experimented tendon stress relaxation within several minutes which are not comparable to the duration of one Ponseti cast.

Composed of a core of elastin and a scaffold of microfibrils, elastic fibre is an important ECM component in soft tissues, providing the tissue with flexibility and extensibility. Most studies which involve observing or imaging the elastin were conducted mainly on arteries with some work on skin, lungs, and kidneys (209–213). In a tendon or ligament, although the elastin contributes to only 1-2% of the tissue dry weight, they were suggested to be responsible for retaining the collagen crimp, ensure elastic stretch and recoil, and play a pivotal role in the resistance of the transverse shear forces within the tissue (139,214,215). To observe the microstructural changes in a tendon after a Ponseti treatment, microscopic techniques to image different tendon ECM components are needed.

Early studies adopted electron microscopy, scanning electron microscopy (SEM) and transmission electron microscopy (TEM), to image elastin in a tendon (105,216–218). However, before imaging, tendon samples will require dehydration treatment which could disrupt the sample microstructure. The use of TEM would also require ultra-thin

tendon samples through sectioning (219). In addition, although both the SEM and TEM are suitable to investigate the ultrastructure of elastin with great resolution, the magnification range is generally too high to visualise the overall organization or the functional unit of elastin.

Other techniques that require minimal tissue processing and enable good elastin visualization were also considered. Recent studies have explored the possibility of using magnetic resonance imaging (MRI) to image elastin. A novel elastin-specific magnetic resonance contrast agent has been developed as an elastin-specific probe (212,220–222). Although MRI is a painless and non-invasive technique, its low-resolution characteristic makes imaging the microscopic morphology of elastin fibres challenging. Histological staining is also a common method for imaging structural components in a tendon. This technique is less expensive, allows for the study of large sections of sample, and is able to visualise multiple components by using different stains. Stains that are specifically used for identifying elastin include Weigert's resorcin-fuchsin stain (223), Verhoeff–Van Gieson stain (VVG) stain (224) and Miller's elastic Van Gieson (MVG) stain (109). Among these staining methods, the Miller's stain has been reported to show better elastin-to-background contrast, elastin

definition and staining consistency, and to be easy to perform (225). However, to visualise the stained structures and components, traditional optical microscopes are commonly used in histology, and they generally do not have sufficient imaging resolution to distinguish the detailed fibre structure of tendons but reveal the overall fibre texture and the morphology of tenocytes.

To solve the problem of poor resolution in histology but still be able differentiate elastin from other ECM components, confocal laser scanning microscopy can be used. Offering better resolution then the conventional wide field optical microscopy, a confocal microscope can control the depth of field, reduce background information at the focal plane, and image serial sections from thick samples. Unlike the conventional optical microscopy, in confocal microscopy, the excitation beam can be focused through objective lens on a small pot inside the sample. The reflected/fluorescent light is then collected, projected, and focused to a detector. A tiny pinhole aperture is applied to allow only the light emitting from the desired focal spot to pass through. This setup allows the microscope to filter out any out-of-focused and scattered light signals that could reduce image resolution (226). The use of autoflorescence signal to visualise elastin has been experimented. Since elastin display excitation maxima at

350-450 nm and emission maxima at 420-520 nm (227), some work has utilized this natural fluorescence signal without tagging elastin with fluorophores. Elastin in various soft tissues including medial collateral ligament, trabecular meshwork tendon, ciliary muscle tendon, coronary adventitia, linea alba and aortas has been imaged by two-photon/multiphoton excitation with excitation wavelengths of 800-850 nm and emission wavelengths collected at 495-550 nm (214,228–231). In addition to autofluorescence signals, sulforhodamine B (SRB), a polar fluorescence dye with low molecular weight (max. absorption: 565 nm & max. emission: 590 nm), has shown to selectively stain elastin over collagen (107,232,233). Ricard *et al.* (234) demonstrated that compared to autofluorescence, which has an emission wavelength in the blue range that can be highly scattered and absorbed by the surrounding ECM and requires long exposure time, the SRB was able to image elastin in muscle epimysium, muscle endomysium and blood vessels with lower incident laser power but better signal intensity. However, in a tendon where elastin only composes 1-2% of tissue dry weight, the two aforementioned methods may not provide sufficient signals, elastin-specificity or bonding of dyes with elastin. These issues can be solved with fluorescence immunohistochemistry (IHC) which uses antibodies to strongly and specifically bond with the antigens on the target protein. This strong bonding between the two molecules

is more resistant to washing procedures and reduces the amount of non-specific binding. After the first or primary antibody bonds with the target protein, a secondary antibody carrying a fluorophore can then bond with the primary antibody. Since the secondary antibody is made in a species that is different than both those of the primary antibody or the specimen, it limits non-specific binding with surrounding antigens other than the primary antibodies which minimizes false positives and background noise (235).

In this chapter, we aim to study the effect of long-term stress relaxation on tendon microstructure. Particularly, how the length of casting or stress relaxation duration would influence microstructure was examined. The collagen crimp morphology of a young bovine deep digital flexor was observed using SEM. The efficacy of multiple methods for imaging elastin in tendons including histology, SRB fluorescence dye and fluorescence IHC were also experimented. Recognizing the microstructural changes and pinpointing the key disrupted ECM components may help us understand the mechanism of Ponseti method and how a tendon is lengthened in each manipulation/casting.

4.2 Materials & Method

4.2.1 Stress Relaxation Test

To determine the objective tensile strain value for modelling a Ponseti cast, two estimations were conducted first. Using a plastic clubfoot model of a 6 to 8-week-old infant from the Nuffield Orthopaedic Centre as an example shown in Figure 4.1, the total tensile strain produced by the correction around the ankle of a clubfoot can be estimated. A deformity component known as adductus describes the medial deviation away from the leg's vertical axis towards the midline (3). The correction to this inward rotation on the medial side of the clubfoot was chosen for the first estimation. The uncorrected angle between the 3rd metatarsal and tibia (metatarsal-talus-tibia) (θ_0) was roughly measured to be 143.4 degrees using ImageJ as shown in Figure 4.1 (red markings). Since a healthy foot can generate a 30-degree rotation towards the lateral side (236), an objective rotation degree was assigned as 210 degrees. Hence, an angle deviation percentage of 46.4% ($(210 - 143.4)/143.4 \times 100\%$) was derived as a simplified approximation to the total tensile strain produced by correcting adductus. A mean cast number of 7.59 was reported by Vaishy *et al.* to correct a clubfoot (237). Since approximately 3 casts were used to correct canvus in the beginning and equinus at the end (238), 4.59 casts would contribute to the adductus correction, and each cast

would produce a tensile strain of 10.1%. Another estimation based on the string elongation using the same clubfoot plastic model (correction of adductus) was also conducted. From the plastic model shown in Figure 4.1, after the correction was applied, the string on the medial side (marked by yellow arrows), which approximates the tebialis posterior tendon, was lengthened, and the length values before (l_0) and after (l_c) the correction were measured. This lengthening of the string was assumed to mimic the lengthening of the tendons and ligaments due to the Ponseti manipulation. The percentage of tensile strain (ε) produced by the correction was calculated using the following equation:

$$\varepsilon = \frac{(l_c - l_0)}{l_0} \times 100\% \qquad \text{(Eqn. 4.1)}$$

This correction procedure was conducted repeatedly for 10 times, and the mean strain was derived as 35.71 ± 6.48%. Similarly, assuming 4.59 casts (237,238) were used to achieve this strain value, each cast would produce a strain of 7.78%. In summary, based on these estimations, a single casting of the Ponseti method may generate a tensile strain between 7-10%. Since a stretch in the linear region would generate irreversible micro-damage to the tendon, painful reaction is likely to occur. Hence, a strain of 8%, which lies in the beginning of the linear region (demonstrated in Figure 4.4 in section 4.3.1), was chosen to model an actual Ponseti casting.

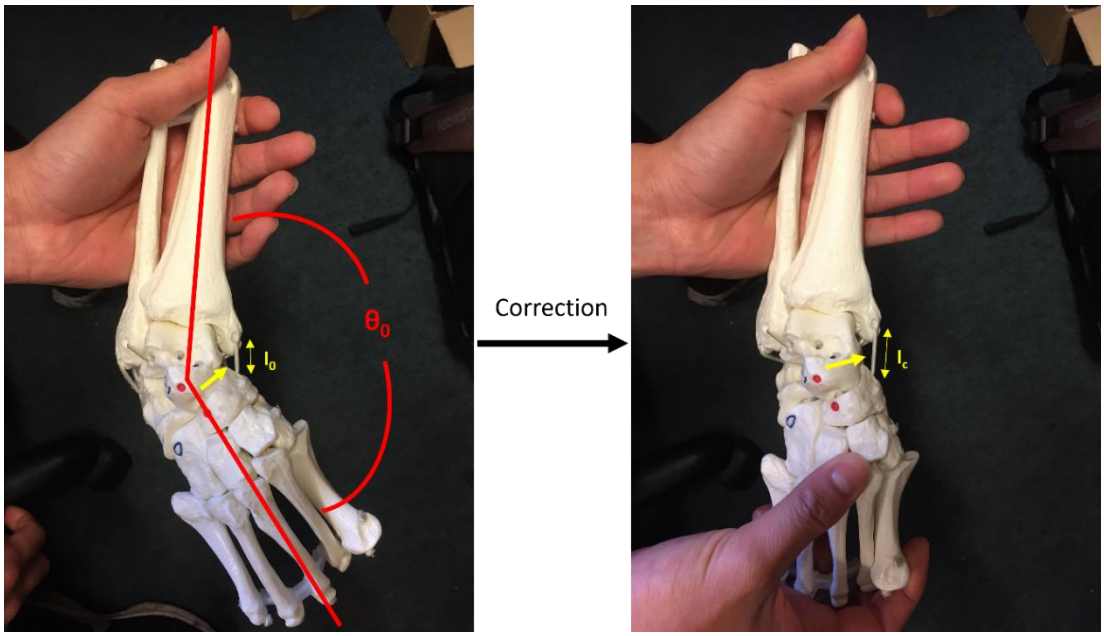

Figure 4.1. Illustrative images of the adductus correction using a plastic clubfoot model. A plastic model for clubfoot without manipulation is shown in the left image in which the red lines marked the inward rotation angle of adductus at the medial side and the yellow arrows marked the string (an approximation of the tebialis posterior tendon) with an initial length (l_0). After correction, which is shown in the right image, lengthening of the string (l_c) simulating the lengthening of tendons and ligaments in the clubfoot can be measured.

Regarding the stress relaxation tests, the sample preparation and mechanical testing set-up were adopted from chapter 3. Briefly, 2 to 4-week-old bovine DDFTs were selectively/partially air-dried on both ends, which left a 50-55 mm testing region in the centre, for secured gripping and failure prevention at the ends. A permanent marker was used to label both ends of the experimental (hydrated) region. The cross-sectional area was acquired from the width and thickness of the sample measured with a calliper,

assuming the cross-sections have an oval shape for all samples. Customized 3D-printed ABS teeth were used to grip the dried sample ends firmly before inserting into an Autograph AGS-X mechanical testing machine (Shimadzu) with a 5 kN load cell. The initial stroke position was set to be at ~0.1N of tensile force for each test. Tendon samples were stretched under a strain rate of 0.5%/s until 8% engineering strain and then held for 0 h (immediate return to initial length), 2 h, 24 h and 48 h. During stress relaxation testing, the samples were wrapped with plastic films and sprayed with phosphate buffered saline (PBS) solution with 0.2 mg/ml sodium azide for every 4-6 hours. After the treatment, the tension was released by reverting to the initial stroke position. The tendon length was then re-measured and compared with its original length. Control samples were prepared by cutting a piece (~1 cm in length) of the original tendon of each experimental group (0 h, 2 h, 24 h and 48 h) before the stress relaxation test.

4.2.2 Sample Preparation for Imaging

To prepare the samples for imaging, the tendons were first cut along the long axis into pieces (~1 cm in length). For Miller's elastic staining, the tendon pieces were directly fixed in 10% formalin. For the rest imaging methods, the tendon pieces were incubated

in cryoprotectant solutions: 15% (w/v) sucrose & 15% (v/v) ethylene glycol in 0.1M phosphate buffer (PB) and 30% (w/v) sucrose and 30% (v/v) ethylene glycol in 0.1M PB successively, embedded in an optimal cutting temperature compound (OCT) (Labtech, 16-004004) in a custom-made mold, and cooled in -20°C. The OCT-embedded blocks were then transferred to a dry ice sliding microtome (Leica Biosystems, SM2000 R) for cryosectioning. Each block was fixed on a stage cooled by dry ice. Tissue blocks were sectioned into 200 µm thick for SEM imaging and into 50 µm thick for fluorescence imaging. All sectioned tendon sheets were washed in PBS three times to remove the remaining cryoprotectant and OCT compound.

For SEM imaging, tendon sections were fixed in 2.5% glutaraldehyde (Fluorochem, 358208), dehydrated by a series of ethanol solutions (50%, 70%, 80%, 90% & 100% x 3 times) and Hexamethyldisilazane (HMDS) (Sigma, 440191), and coated with ~6 nm of platinum before imaging; for fluorescence confocal imaging, tendon sections were fixed in 10% formalin (Sigma, HT501128) before staining.

For Miller's elastic staining, to allow paraffin wax to fully infiltrate the tissue, the formalin-fixed tendon piece was dehydrated using a series of ethanol solutions with an

increasing concentration gradient (50%, 70%, 80%, 95% & 100% x3). Clearing of the tendon sample was achieved through treatment of xylene. As the dehydrated samples were immersed in three changes of xylene, the residual ethanol in the tissue was gradually replaced with xylene and the sample became transparent. The samples were then immersed in three different paraffin wax immersions to replace xylene in the tissue with paraffin and the samples were embedded into blocks. Lastly, tissue blocks were sectioned into 5 µm thick sections using a microtome (Leica Biosystems, RM2125 RTS). Sections were transferred onto glass microscope slides in a warm water bath (40-45^{o}C). After dried in air for 30 minutes, the sections were baked in an oven at 45^{o}C overnight before proceeding to staining. The Miller's elastic stain (TCS Biosciences, HS237) staining procedure is illustrated as follows: Paraffin embedded tendon sections were transferred into a xylene solution to remove paraffin wax from the sections. These deparaffinized sections were immediately treated with a series of ethanol solutions with descending concentrations (100% for 3 min x 2, 95% for 1 min & 70% for 1min) to gradually rehydrate the samples. Sections were oxidized in 1% potassium permanganate for 5 min and 1% oxalic acid was later used (10 min immersion) to remove potassium permanganate from the tissues. After washing with 95% ethanol, sections were stained with Miller's stain for 3h. Once staining was

completed, sections were wash with 95% ethanol and running H_2O before counter-staining with Van Gieson stain for 4 min which could give the collagen background a pink/red colour. This counterstain would provide a colour contrast to the elastin that was stained black. Lastly, sections were dehydrated by ethanol gradient and treated with xylene before mounting on slides with dibutylphthalate polystyrene xylene (DPX) (Solmedia, REA219). Stained sections were imaged under optical microscope.

Staining with SRB dye was achieved by directly immersing the tendon sections in a 1 mg/ml SRB solution for 1 min followed by washing with PBS three times. SRB solutions were prepared by dissolving SRB powders (Sigma, 230162) in PBS solution. The effect of fixing with 10% formalin, treatment with hyaluronidase (4800 units/ml) and treatment with collagenase (30 cdu/ml) were examined. The treatment of hyaluronidase or collagenase before staining has been shown to improve tissue permeability for SRB molecules (239). Both enzyme solutions were prepared by dissolving the stock powders (Sigma, H3506 and Sigma, C0130) in PBS solution.

To prepare samples for fluorescence IHC, tendon sections were permeabilized with 0.1% triton x-100 (Sigma, T8787) for 10 minutes, blocked with 1% bovine serum

albumin (BSA) (Sigma, A9647) in PBS that contained 0.05% triton x-100 for 1 hour to minimize non-specific hydrophobic bonding before primary staining. Tendon elastin was immunostained with rabbit anti-elastin antibody (Abcam, ab21607) as the primary antibody and with Alexa FluorTM 488 goat anti-rabbit IgG (Invitrogen, A-11034) as the secondary antibody. Briefly, tendon sections were incubated in the primary antibody solution of 1:200 dilution (in 1% BSA) at 4 °C for 48 h. Samples were then washed with PBS and incubated in the secondary antibody solution of 1:500 dilution (in 1% BSA) for 1 hour at room temperature. After washing with PBS, cell nuclei in the tendon were stained by incubating the samples in a DAPI solution (1:1000 dilution in PBS) for 10 min at room temperature. Once staining was complete, samples were mounted on microscope slides with FluoroSave mounting media (Sigma, 345789).

4.2.3 SEM Imaging

The collagen fibre morphology of the tendon was visualised by an Evo MA10 SEM (Zeiss). To compare the changes happened in these two parameters, a small piece of control sample was cut off from the original sample using surgical blades before the stress relaxation test for each experimental group which allows direct comparison of

each sample with its untreated counterpart. The crimp angle (θ) and fibre side length (d) in each crimp were measured (30 sets of data points) using ImageJ. More details will be displayed in section 4.3.2. Two-sample t tests were conducted to test the hypothesis of no difference between the treated and the control groups.

4.2.4 Confocal Fluorescence Imaging

The elastin morphology was captured using a FV1000 confocal laser scanning microscope (Olympus). SRB-stained sections were excited at 559 nm and SRB emissions were collected at 565-600 nm. IHC sections tagged with Alexa Fluor 488 were excited at 488 nm and collected using a 500-530 nm bandpass filter. A 20× and an oil immersion 60× objective lenses were used to collect emission spectra.

Image processing and analysis were performed using ImageJ to reduce background noise and to quantify the 2D elastin volume fraction. The amount of fragmentated elastin in the stress-relaxed samples was also quantified using threshold adjustment (details will be explained later in section 4.3.3).

4.3 Results

4.3.1 Physical & Mechanical Integrity

The stress-time profile of the stress relaxation test of the 2 h experimental group was displayed in Figure 4.2. As an illustration, all experimental groups produced similar stress-time profiles in which the stress response clearly differentiated the toe and linear regions in the first 16 seconds under a slow strain rate of 0.5%/s (compared to common stress relaxation tests (135,240–243)) and then exponentially decayed over time after t = 16 s where 8% strain was reached.

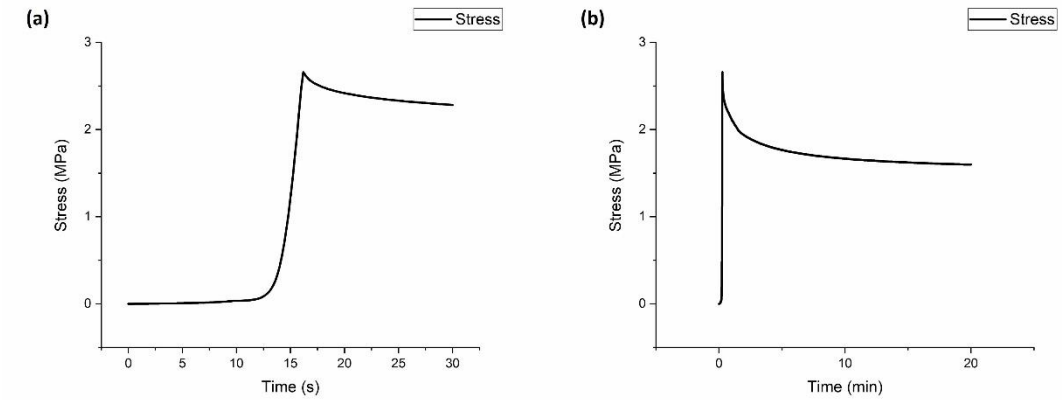

Figure 4.2. The illustrative stress-time mechanical profile of a young bovine DDFT undergoing 2 h of stress relaxation.
(a) The initial 30 seconds of the relaxation profile displaying the transition from the 'toe' to 'linear' region. (b) The initial 20 minutes of the relaxation profile displaying the exponential decay of stresses.

After the stress relaxation treatment, the tendon samples showed lengthening without loading. The tendon lengthening percentages of different relaxation durations are displayed in Figure 4.3. The results show that the degree of tendon lengthening is

dependent on the duration of stress relaxation. No statistical difference was spotted between the 24 h and 48 h groups which suggests the 'material part' of tendon lengthening or the maximum lengthening in a single Ponseti cast was achieved within the first day of casting. Stress relaxation for 2 h was able to reach approximately 83% of the maximum lengthening value from the 24 h and 48 h groups.

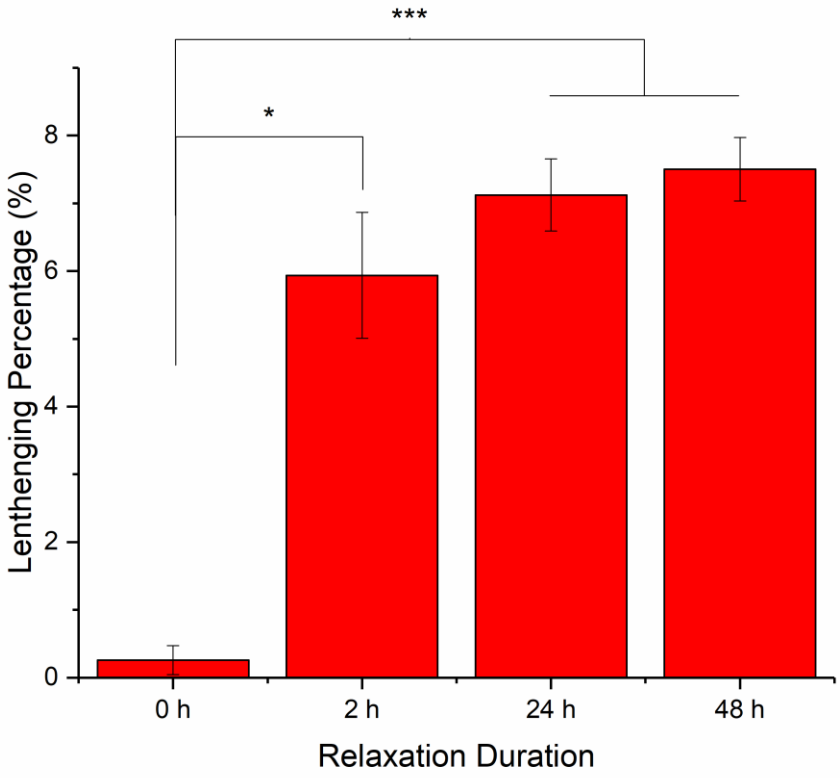

Figure 4.3. The tendon lengthening percentages due to stress relaxation.
The lengthening ($\Delta L/L_0 \times 100\%$, L: *tendon length*; L_0: *initial tendon length*) of different relaxation durations (0 h, 2 h, 24 h & 48 h) calculated based on Eqn. 4.1. All data are displayed as the mean ± SD (n=3). Significant differences were analysed by 2-sample t-test. *$P < 0.05$, ***$P < 0.001$.

To investigate the variation in mechanical profile, a second tensile test were conducted on the 2 h group immediately after the stress relaxation. Once the stress relaxation experiment was complete, the tendon was allowed to return to the initial stroke position (where the first test started) and then stretched to the same stroke position (where the first test ended) under the same strain rate. A set of illustrative stress-strain curves were displayed in Figure 4.4. To compare the differences in stress response at each elongation point, stresses in both curves were plotted against the engineering strain values of the first curve (stress relaxation test). Throughout the whole 8% strain, the stress responses of the second tensile test were lower than those of the first tensile test at all strain values. On the other hand, no reduction in the Young's modulus (first test: 201.6 ± 62.3 MPa and second test: 250.7 ± 68.3 MPa), which was derived by linearly fitting the short linear region below 8% strain, was confirmed statistically using the paired t test.

(a)

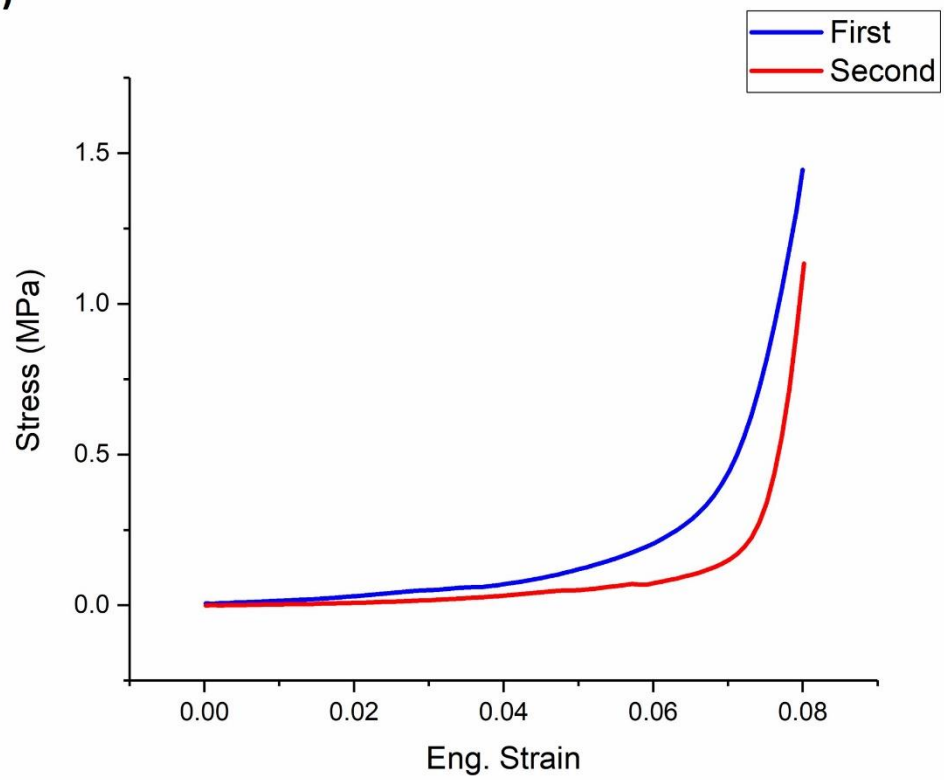
First
Second
Stress (MPa)
1.5
1.0
0.5
0.0
0.00
0.02
0.04
0.06
0.08
Eng. Strain

(b)

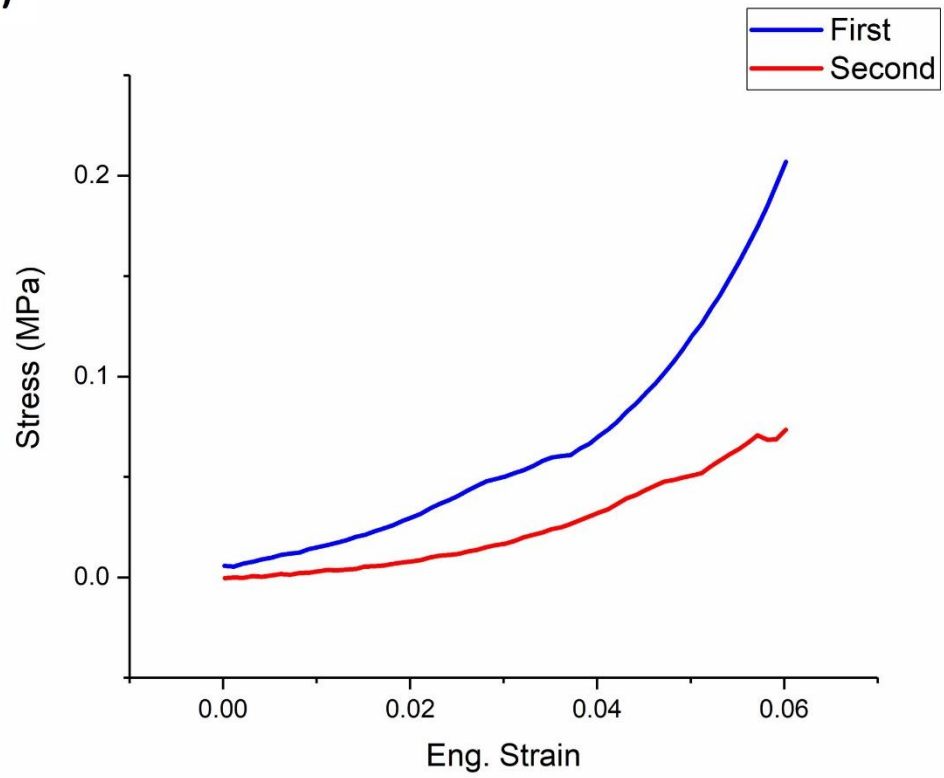
First
Second
Stress (MPa)
0.2
0.1
0.0
0.00
0.02
0.04
0.06
Eng. Strain

Figure 4.4. The illustrative mechanical profiles of a young bovine DDFT before and after the 2 h stress relaxation treatment. (a) The stress-strain curves of the first (blue) and second (red) tensile straining. The second test was conducted at the same initial stroke position and under the same strain rate of 0.5%/s as the first test. (b) The stress-strain curves of the initial 6% strain of (a).

4.3.2 Collagen Crimp Morphology

Figure 4.5 shows the surface morphology of a bovine DDFT stress-relaxed for 48 h and its untreated control capture by SEM imaging. Images of the control displays the common wavy pattern of collagen fibre crimp in tendon tissues. On the other hand, regions of flattened crimps were spotted in tendons that experienced long-term stress relaxation.

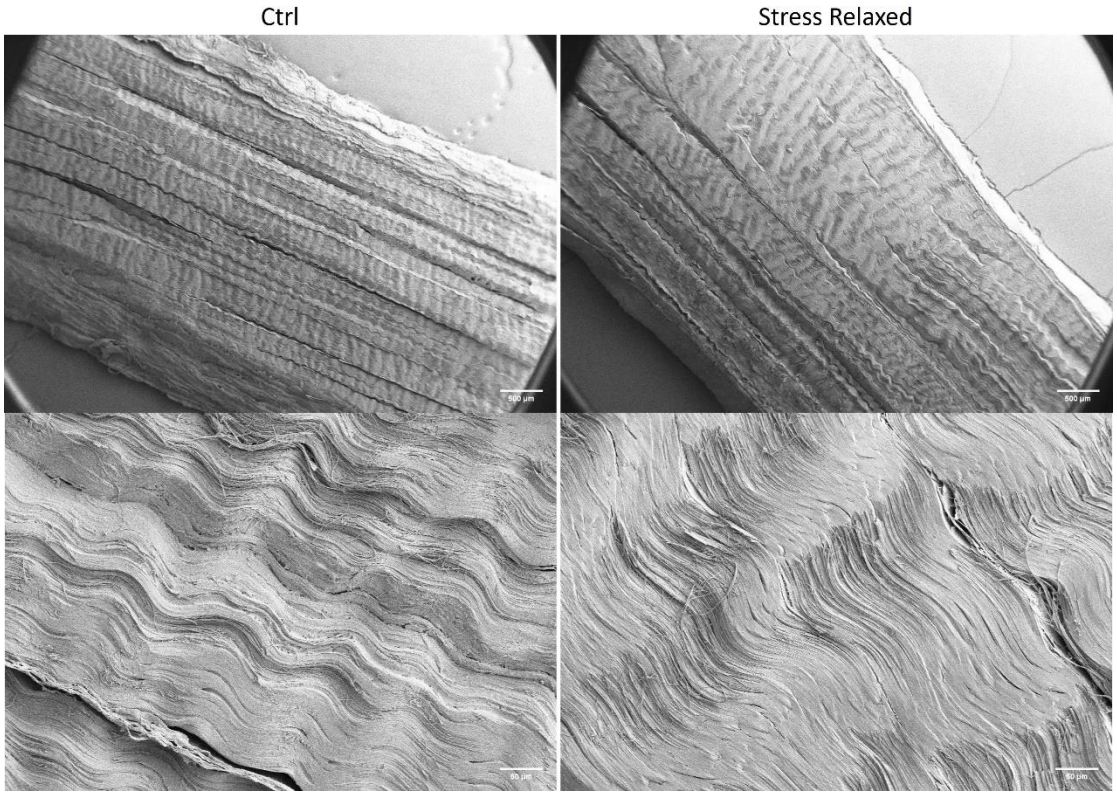

Figure 4.5. SEM images of the stress-relaxed tendons (right column) and its control (left column). Scale bars are 500 μm (top row) and 50 μm (bottom row).

The angles (θ) and the side length (d) of a crimp were measured using ImageJ according to the illustrative SEM image in Figure 4.6. For each experimental group of relaxation duration, 30 measurements (n = 30) were recorded for both θ and d, and the values were compared to those obtained from its corresponding control.

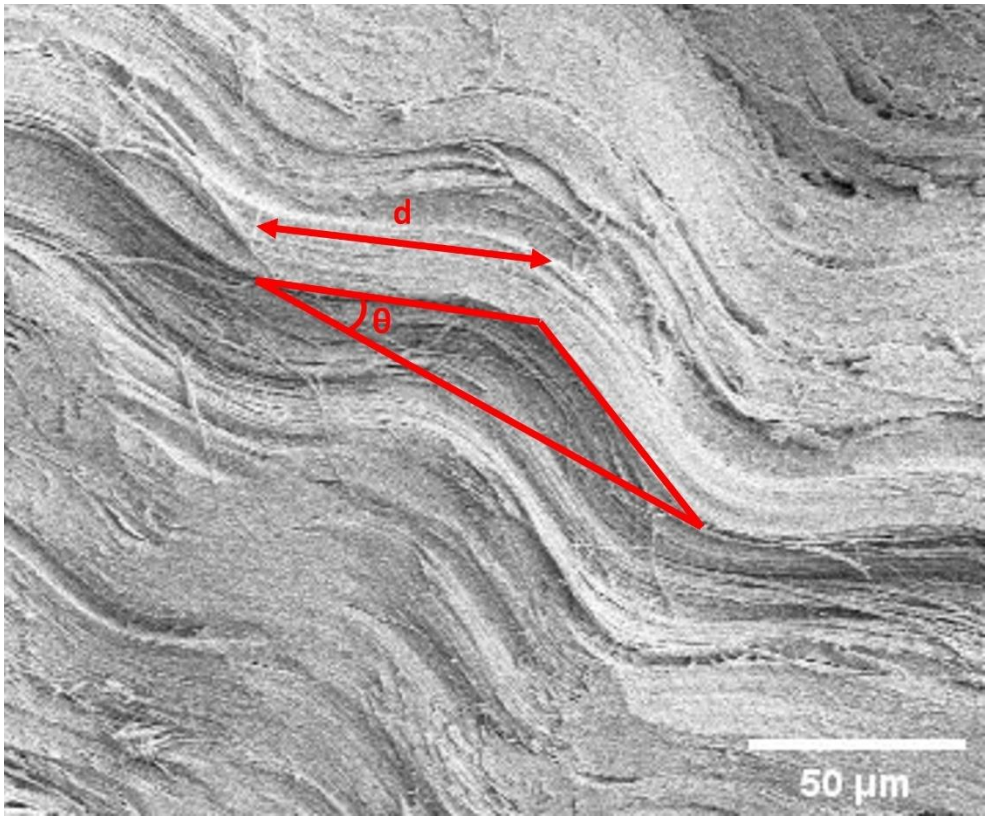

Figure 4.6. Illustration of crimp angle (θ) and side length (d) measurement. Scale bars are 50 µm.

Crimp angle reduction was discovered in tendons treated with stress relaxation, while no change was seen on fibre side length. As shown in Figure 4.7 and Table 4.1, different durations of stress relaxation showed different levels of crimp angle reduction that coincides with the levels of the tissue's lengthening (2 h < 24 h = 48 h). No angle reduction was spotted in the 0 h group which highlighted the importance of relaxation duration (length of casting). Since no change was observed on crimp side length in each experimental group, according to the demonstration in Figure 4.6, the

contribution of angle reduction to lengthening can be calculated using the following equation:

$$\text{Lengthening } (\Delta\theta) = \frac{\Delta L}{L_0} = \frac{\cos\theta_{Exp} - \cos\theta_{Ctrl}}{\cos\theta_{Ctrl}} = \frac{\cos\theta_{Exp}}{\cos\theta_{Ctrl}} - 1 \qquad \text{(Eqn. 4.2)}$$

The calculated result displayed in Figure 4.8 shows similar order (2 h < 24 h = 48 h) comparing to the result in Figure 4.3.

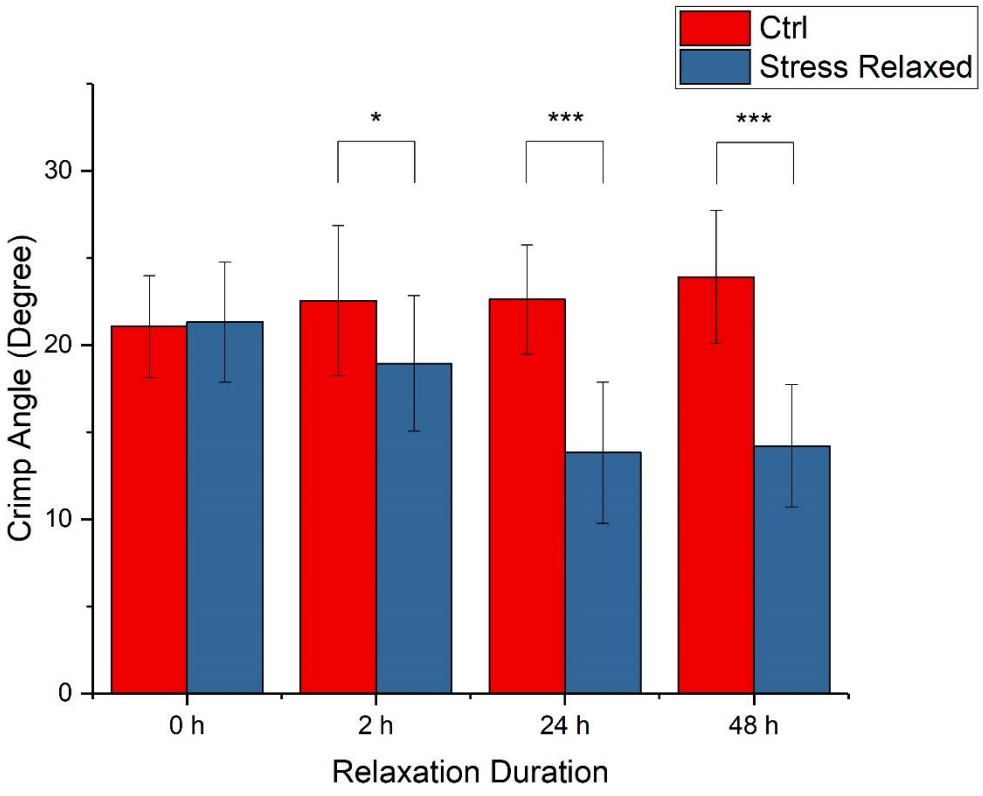

Figure 4.7. Crimp angle reduction of tendons treated with stress relaxation.
Crimp angle values of tendons treated with stress relaxation (blue) for different durations (0 h, 2 h, 24 h & 48 h) and their respective controls (red). Data are displayed as the mean ± SD (n=30). Significant differences were analysed by 2-sample t-test. *P < 0.05, ***P < 0.001.

Table 4.1. Values of crimp angle reduction of tendons treated with stress relaxation of different durations. Data are displayed as the mean ± SD.

Relaxation Duration	2 h	24 h	48 h
$\overline{\theta_{Exp}} - \overline{\theta_{Ctrl}}$ (degree)	3.61 ± 3.89	8.79 ± 4.05	9.70 ± 3.51

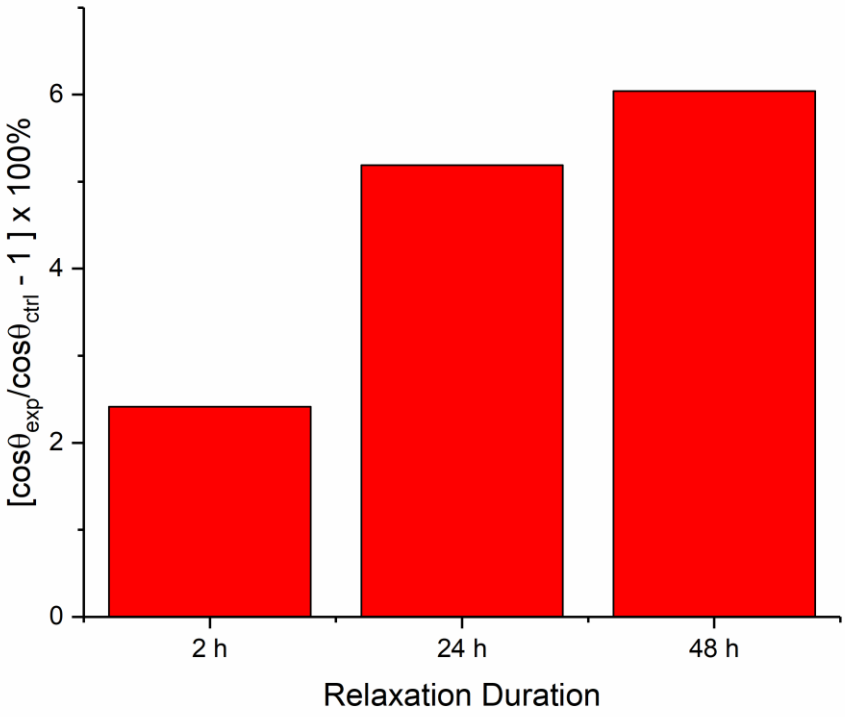

Figure 4.8. Estimated values of tendon lengthening contributed by crimp angle reduction of tendons of different stress relaxation durations (2 h, 24 h & 48 h) calculated using Eqn. 4.2.

4.3.3 Elastin Imaging and Elastin Morphology

4.3.3.1 Miller's Stain

Sections stained with Miller's elastic stain are shown in Figure 4.9. No cells can be seen in the matrix under the microscope. The collagen fibres, which are the primary ECM in the sample, appeared in a red/pinkish colour. The elastin should appear as sparse dark fibres conforming to the crimp morphology, but they are barely visible. In addition, the density of elastin in the image appears to be lower than that in an immunostained image (Figure 4.11) which will be further examined in detail in section 4.3.3.3. Overall, the Miller's stain method provides a fast and simple way to visualise the general elastin morphology in a section. However, a conventional light microscope was unable to image the ECM with higher resolution and magnification.

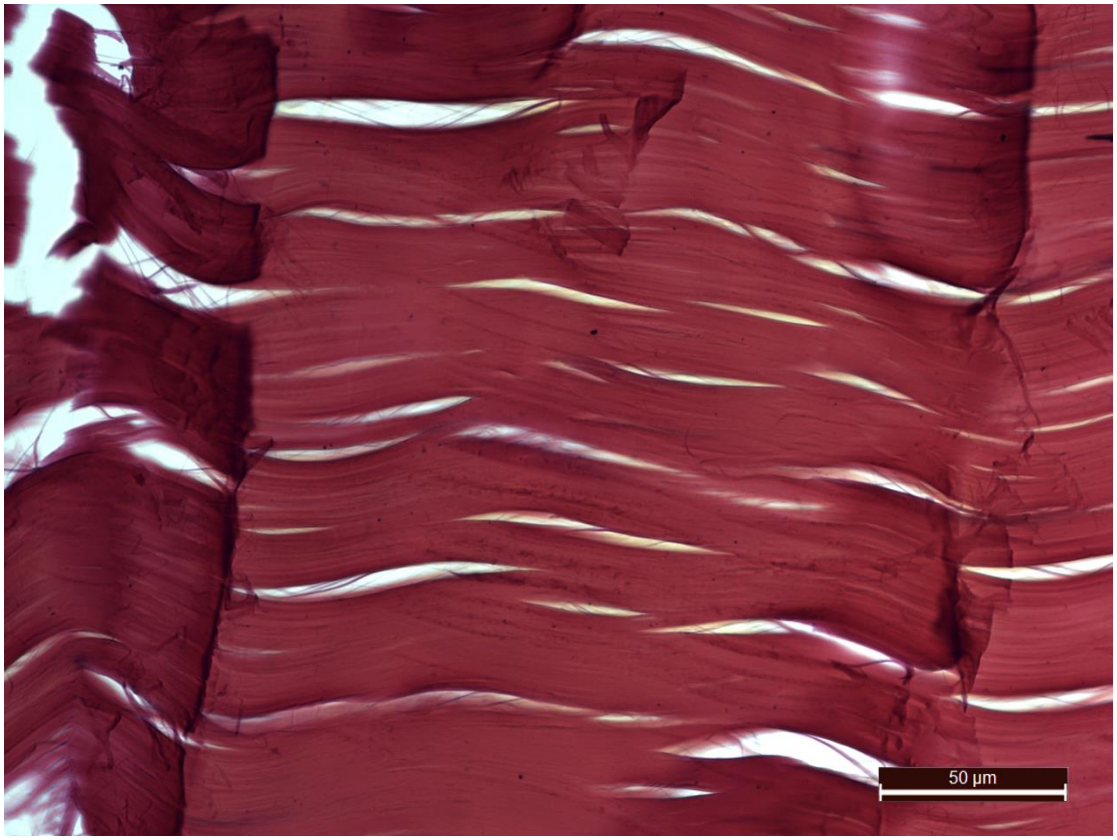

Figure 4.9. A tendon section stained with Miller's elastic stain. The collagen matrix was stained darkish red. The elastin, which should be stained black, was not observed. Scale bars are 50 µm.

4.3.3.2 SRB Dye

The results of SRB staining for elastin are shown in Figure 4.10 and Figure 4.11. Control samples, which did not treat with SRB, displayed a blank view under 559 nm excitation with a bandpass filter at 565-600 nm. Fixing with 10% formalin or treatment with hyaluronidase or collagenase did not improve image clarity nor enhance the fluorescence intensity of elastin. Treating an unfixed sheet with hyaluronidase or

collagenase would cause it to fall apart; hence, the effect of hyaluronidase or collagenase was only experimented on fixed samples.

Although the collagen fibres appear to also have an affinity to SRB molecules, elastin was present as fibres with higher fluorescence intensity (marked by white arrows in Figure 4.11) and were distributed throughout the collagen matrix following the crimp morphology. Background subtraction could reduce noise from collagen which made elastin more visually apparent as shown in Figure 4.11. However, emissions from collagen are still visible in several regions (yellow circles).

Decreased SRB concentration and increased washing time both reduced the fluorescence intensity from the ECM, implying this method displays not only non-specific but also weak binding to the ECM.

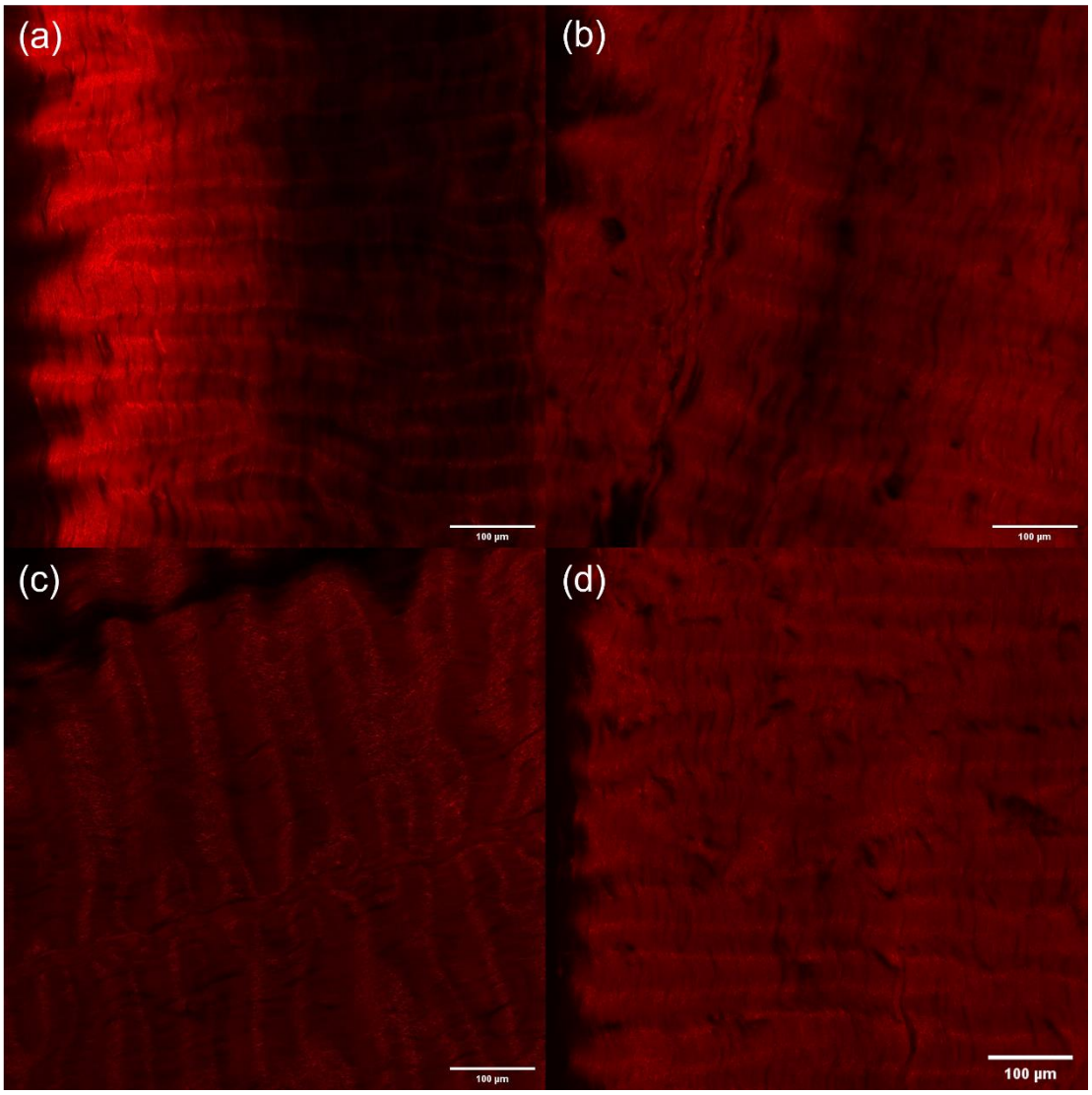

Figure 4.10. Fluorescence images of tendon sections stained with SRB: (a) unfixed section; (b) fixed section; (c) section treated with hyaluronidase; (d) section treated with hyaluronidase and collagenase. Scale bars are 100 µm.

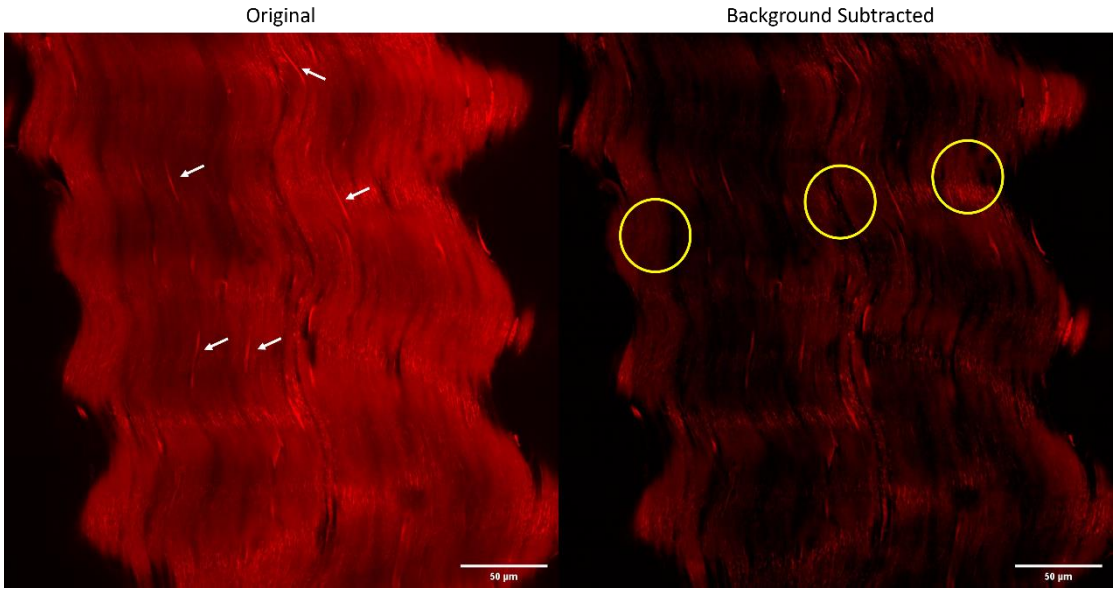

Figure 4.11. Fluorescence image of tendon section stained with SRB before and after background subtraction. Scale bars are 50 µm.

4.3.3.3 Fluorescence Immunohistochemistry

Elastin imaging with fluorescence IHC displays better clarity than the other two methods. Compared to SRB staining, IHC stained images show consistent elastin signal intensity and low background emission throughout the sample. As seen in Figure 4.12, within a tendon fascicle matrix (FM), Elastin fibres run in accord with the collagen crimp morphology along the tendon long axis and are evenly distributed throughout the sample. These shape and distribution can also be justified by viewing the cross-sectional sections in which the elastin fibres sparsely appear as points and dots in the FM. Outside the FM, in the regions of interfascicle matrix (IFM), the elastin fibres do not appear as aligned/organised fibres but rather as clusters spreading all over

the IFM. In addition, the emission intensity of elastin in the IFM was higher than that in the FM, indicating a higher amount/density of elastin in the IFM.

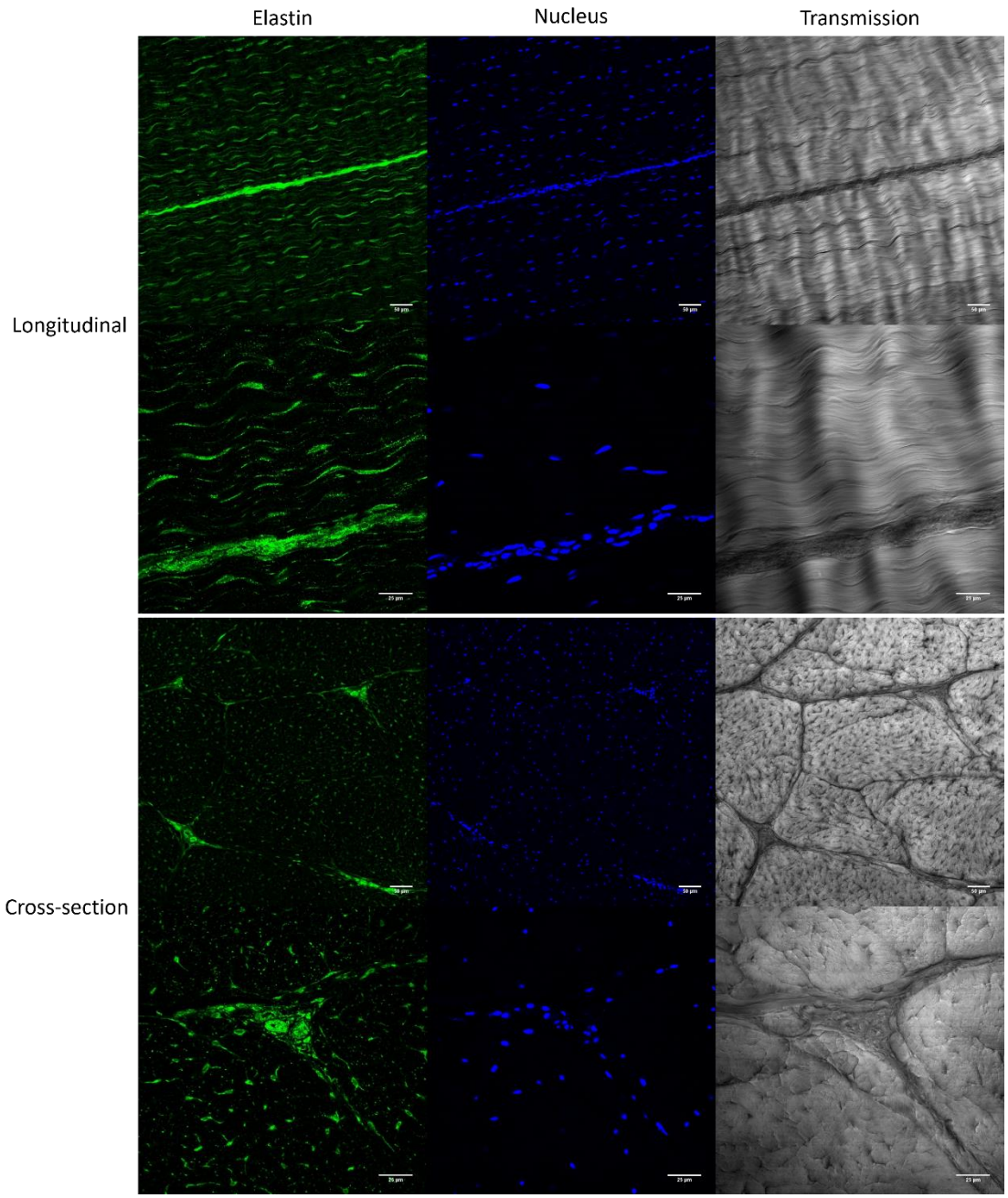

Figure 4.12. Fluorescence images of immunostained elastin and DAPI-stained cell nuclei. Representative immunostained tendon images captured by confocal microscopy revealing the morphology of elastin (green; left column), cell nuclei (blue; mid column) and tendon matrix (grey; right column) in bovine DDFTs. Images are displayed in the longitudinal view (top 2 rows) and the cross-sectional view (bottom 2

rows). Scale bars in the 1st and 3rd rows are 50 μm; scale bars in the 2nd and 4th rows are 25 μm.

Through DAPI staining, cell nuclei were visible in both the FM and IFM. From both the longitudinal and transverse section of the sample, a large portion of elastin was seen to be localized around cells in both the FM and IFM.

Elastin imaging on stress-relaxed tendon samples, which is shown in Figure 4.13, discovered altered elastin morphology. The results discovered fragmentation of elastin distributing throughout the tendon matrix. The features of elastin fragmentation commonly seen in cardiovascular tissues include: (I) cluster-forming elastin fragments (mostly spherical shape); (II) assembly or localization of these clusters; (III) higher elastin fluorescence intensity from these clusters compared to the surrounding unfragmented elastin. These features were also seen in the stress-relaxed tendon samples displayed in Figure 4.13. The level of elastin fragmentation was quantified based on image analysis (2D) using ImageJ. Briefly, as illustrated in Figure 4.14, (I) the regions containing fragmented elastin clusters were selected and cropped from the original image; (II) the cropped images were converted to 8-bit grayscale; (III) the threshold of the image was adjusted based on the mean fluorescence level of the local

healthy/intact elastin (mean of 5 intensity maxima) where all fluorescence signals lower than this mean were excluded; finally, (IV) the total area of these elastin fragments were measured using particle analysis where only particles of size larger than 5 pixel^2 were included. Because the elastin fluorescence intensity was much higher in the IFM compared to that in the FM, and the elastin in the IFM did not appear as fibres in the IFM, differentiating the fragmentated elastin from the healthy elastin in IFM based on fibre shape and fluorescence level was not viable. Hence, only the area of the fragmented elastin in the FM was considered for the elastin fragment quantification. Similarly, the fragmentation level shown in Figure 4.15 also corresponded to both the levels of crimp angle reduction and tissue lengthening (2 h < 24 h = 48 h) shown in the previous sections.

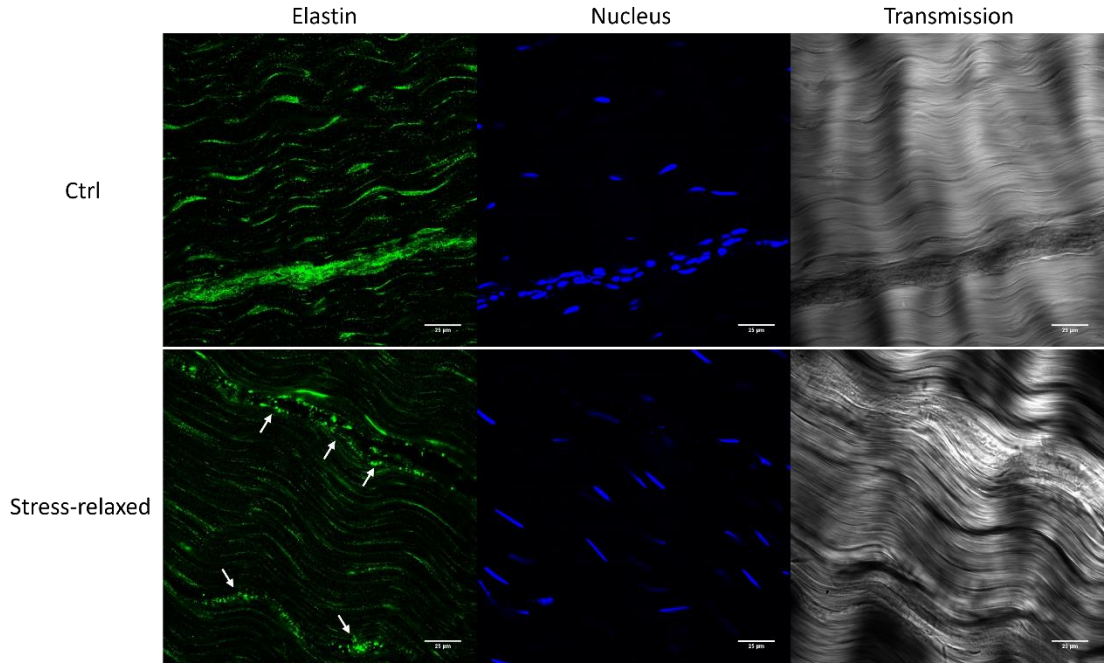

Figure 4.13. Comparison of the elastin morphology (left column), cell nuclei (mid column) and tissue matrix background (right column) of a healthy tendon (top row) to those of a stress-relaxed tendon (bottom row). Fragmentated elastin is marked by white arrows. Scale bars are 25 µm.

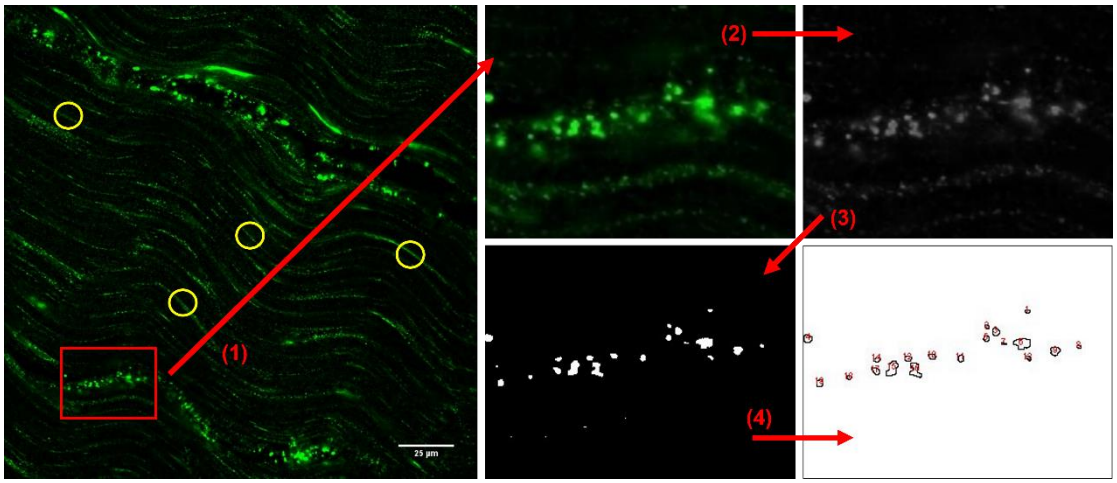

Figure 4.14. Illustration of the collection and the quantification (particle analysis) of elastin fragments. The quantification process was conducted as follows: (I) The regions containing fragmented elastin clusters were selected and cropped from the original image; (II) the cropped images were converted to 8-bit grayscale; (III) the threshold of the image was adjusted based on the mean fluorescence level (mean of 5 intensity maxima) of the local healthy/intact elastin (yellow circles) where all fluorescence signals lower than this mean were excluded; finally, (IV) the total area of

these elastin fragments were measured using particle analysis where only particles of size larger than 5 pixel^2 were included.

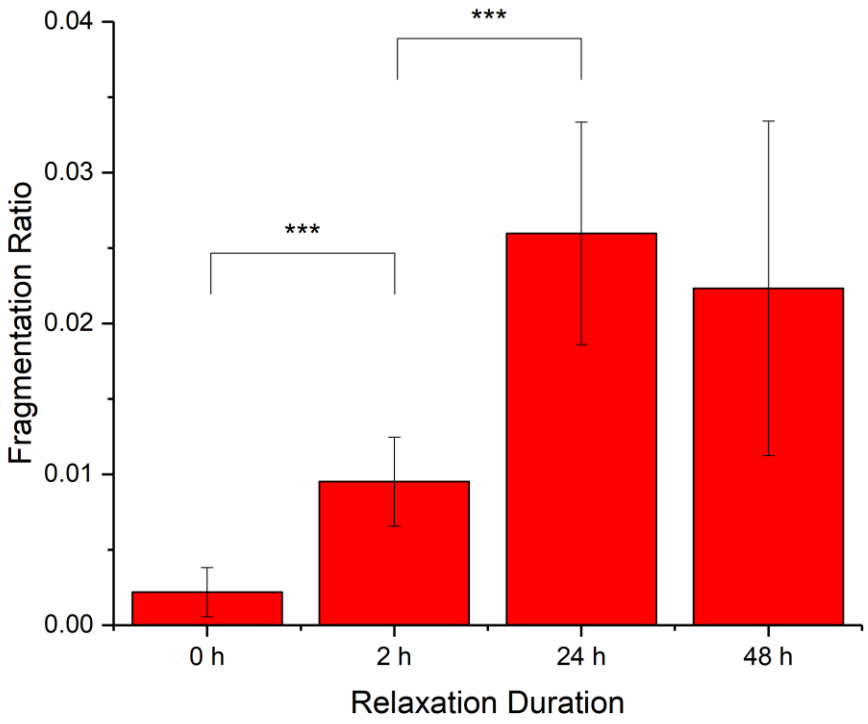

Figure 4.15. The elastin fragmentation ratio in the tendon matrix after the treatment of stress relaxation. Values of fragmentation ratio of young bovine DDFTs treated with stress relaxation of different durations (0 h, 2 h, 24 h & 48 h). Data are displayed as the mean ± SD (n=20). Fragmentation ratio is defined as the total area of elastin fragments over the image area (tendon matrix area) for each fluorescence image. Significant differences were analyzed by 2-sample t-test. *$P < 0.05$, ***$P < 0.001$.

4.4 Discussion

A long-term stress relaxation modelling the Ponseti method successfully lengthened a tendon without the loss of elastic modulus *in vitro* in less than 24 hours. From the lengthening results (Figure 4.3), 83% of the maximum lengthening value could be

achieved in 2 hours of treatment. While the actual time required to produce the maximum lengthening is still unclear, it is likely to fall within the first few hours of the casting period. This time length for generating the lengthening, which is a material-based adaptation to mechanical loading in this *ex vivo* experiment, is much shorter than the duration of existing experiments studying the biological adaptation of the tendon responding to loading (145,152–154). In general, a 2 h duration is not sufficient for ECM deposition or degradation by cellular activities to occur or to be detected, which suggests that this lengthening response for the long-term stress relaxation would also be a material-based adaption primarily in an *in vivo* condition within 2 h to 24 h. In addition, studies that examined the effect of mechanical treatment has centred on dynamic or cyclic loading (145,244–247); hence, the biological response from a long-term stress relaxation has not yet been well-studied.

Mechanically, the second tensile test performed on the stress-relaxed tendons discovered decreased stress values throughout the whole 8% strain. This reduction of stresses was likely caused by the long-term stress relaxation treatment which might plastically deformed certain ECM components in the tendon. However, no loss of the Young's modulus has been observed. Existing studies (247,248) have studied the

effect of preconditioning on tendon microstructure and tensile properties and have discovered augmented stiffness and modulus which suggests that collagen fibre realignment could be a potential mechanism of preconditioning. Hence, the increase of modulus after the stress relaxation test may be the result of progressive fibre rearrangement/realignment occurred during stress relaxation as more collagen fibres were responding when the tendon was stretched in the linear region in the second test. Furthermore, the capability/capacity of inter-fibre sliding, which is known as a mechanism for force damping and stress dissipation during tension, could have been consumed during the first long-term stress relaxation test (76,134,135,249). Besides the deviations in stresses and modulus, the transition region from toe to linear was reduced and became sharper after the stress relaxation. Although from Figure 4.3, the onset strains of the transition from toe to linear for the first and second curves are ~6% and ~7%, respectively, the actual test starting point (where the sample experienced tension) for the second curve is about 2% strain on the X-axis where detectable stress values appeared, meaning the actual transition occurred at ~5% strain for the second curve.

The stress-relaxed tendons also displayed flattening of the collagen crimps revealed under SEM imaging (Figure 4.5). As no tension was applied on the stress-relaxed tendon, this crimp angle reduction was irreversible, and thus the capacity for uncrimping in response to loading would be reduced. This angle reduction also contributes to the lengthening of the tendon tissue as shown in Figure 4.8. However, the value of the percentage of lengthening due to crimp angle reduction (Figure 4.8) was smaller than that of the bulk tissue lengthening (Figure 4.3) in each experimental group which suggests additional lengthening mechanism contributing to the tissue lengthening. As no change was found on the fibre side length of the crimps due to stress relaxation, irreversible sliding of the collagen fibres was most likely to be the additional contribution to lengthening. This angle reduction in the absence of loading is also responsible for the reduction of toe region after the stress relaxation treatment seen in section 4.3.1. As the 'uncrimping' behaviour would progressively occur during tension in the toe region (250–252), it is reasonable to expect a reduction of toe region after the treatment.

The function and mechanical properties of a tendon is highly dependent on the structural arrangement of collagen fibres. Crimp, a unique planar sinusoidal waviness

of the fibres, plays a vital role in the mechanical behaviour of tendon including natural shock-absorbing, elastic recoil and physiological toe region (252–255), and is believed to be formed during the embryonic development stage (255,256). Changes in crimp morphology such as crimp size, crimp angle and crimp periodicity length are known to be influenced by tendon types, age, training, injuries, and even pathological conditions (250,257–264). Generally, for a certain type of tendon, aging, injuries, and training would result in the reduction of crimp angle (257–260,262,264). Franchi *et al.* (262) stated that the crimp angle reduction is a consequence of a functional adaptation of ECM to exercise to increase tendon stiffness and force transmission efficiency; however, in the case of an aged or injured tendon, a reduced crimp angle could predispose the fibres to overstretching and further damage. The microtrauma could accumulate with further high load cycles and eventually result in tendonitis (258,259). Although the crimp angle reduction observed in this experiment was independent of tissue remodelling and biological adaptation of the tendon, these studies provide insights on the potential risk brought by the Ponseti casting. As the disruption of crimp morphology will certainly influence the structural, functional, and mechanical integrity of a healthy tendon, the restoration of the crimp structure would need to be examined as an indication for treatment success.

Several methods for elastin imaging were explored in this chapter. To achieve better resolution, the confocal laser microscope was chosen. SRB staining on elastin was unsuccessful due to the nonspecific binding of SRB molecules on collagen which was also seen in existing studies on tendon elastin imaging (107,233). Therefore, although SRB staining has been demonstrated to be a fast and simple technique to visualise elastin in a tendon, its affinity to collagen is an issue. As the majority of the ECM in a tendon is collagen, and elastin contributes to only 1-2% of the tissue dry weight, the signal-to-noise ratio is difficult to overcome. Furthermore, due to the weak binding of SRB molecules to the ECM, the significant variance of fluorescence intensity from washing duration or dye concentration would largely disturb the imaging integrity and consistency. Overall, imaging via immunohistochemistry and confocal laser microscope produced better tendon elastin images with higher resolution, magnification, and elastin-specificity.

A healthy elastin morphology in a tendon FM (Figure 4.12), which appears as wavy fibres conforming the collagen crimp, matches the observations seen in current work (107–109,219,233). On the other hand, elastin in the IFM does not display as aligned

fibres and is higher in amount. As the IFM is mechanically softer than the FM, with a much higher content of elastin, elastin may play a key mechanical role in the IFM, most likely facilitating fascicles to slide and recoil back with respect to each other, withstanding shear stresses, and transferring load between fascicles (214,219,265,266). Similarly, elastin in the FM is also speculated to participate in inter-fibre sliding and load transfer (215,233,267). Another observation revealed from the fluorescence images is the affinity of tendon cells with elastin. This close localization implies interactions between cells and elastin, and that elastin could influence cellular function and health. In the case of mechanical loading, as the elastin is known to participate in load transfer between fibres and fascicles, mechanical cues could be introduced to cells by elastin, thus triggering mechanotransduction and in return initiating tissue remodelling and mechanical adaptation (268). In a tendon, tenocytes are the primary cells that are responsible for tendon ECM deposition and remodelling. They are "specialized" fibroblasts primarily residing in the FM which have an elongated cell shape and a spindle-like nucleus. As seen in Figure 4.12, the shape of the cell nuclei in the FM does match the spindle-like feature of the tenocytes while the cell nuclei in the IFM display a more rounded shape. Additionally, like the case of elastin content, the cell density is much higher in the IFM compared to the FM. Although tenocytes

have been reported to change their shape of nucleus in response to mechanical load/strain (245), the IFM cells are commonly believed to be different from the tenocytes in FM (265,269). Having different cell types and cell densities, the ECM remodelling and turnover rates in both regions could be different. Thorpe *et al.* (270) has discovered higher abundance of neopeptides or protein fragments in the IFM by mass spectrometry, indicating greater matrix degradation or matrix turnover in the IFM. Hence, it is reasonable to predict that these two regions may respond differently to adapt to mechanical loading.

Elastin fragmentation, which is a common degeneration seen in aged elastic tissues (271–275), was found in stress-relaxed tendons shown in Figure 4.13. Again, a time-dependency (2 h < 24 h = 48 h) matching those of tendon lengthening and crimp angle reduction was seen in elastin. These cross-supporting results indicate a possible mechanism, which may also be a potential drawback, for the Ponseti method. The irreversible crimp angle reduction, which contributed to the lengthening of tendon, was a result of elastin fragmentation as the elastin protein is known to be responsible for the extensibility and retractability of both the collagen crimp and the tendon tissue (77,105,106). To understand and speculate the cause of elastin fragmentation due to

the stress relaxation treatment, the theories of the origin of the elastin's elasticity including rubber elasticity, liberational entropic mechanism, and hydrophobic effect (276) were first studied. Among these theories, the hydrophobic effect is the most well-known theory which took the unique hydrophobic feature of elastin into account and explained the reason for the requirement of water for generating elasticity. Because elastin is composed of multiple hydrophilic and hydrophobic domains, under its relaxed state *in vivo*, the polypeptide self-arranges its conformation (folding) to minimize its hydrophobic regions exposed to the hydrophilic environment and maximize its hydrophobic-hydrophobic interactions to achieve the lowest free energy state. As tension is applied, the extended state (unfolding) of the elastin leads to increased hydrophobic-hydrophilic interactions (solvent-accessible hydrophobic regions) and decreased hydrophobic- hydrophobic interactions resulting in a higher free energy state which gives rise to its elasticity. This folding mechanism of elastin not only produces its elasticity, but also contributes to its high resilience to hydrolytic degradation (277–280). Urry *et al.* studied the effect of conversion of hydrophobic regions into polar residue on hydrophobic folding using elastin-like polypeptides and concluded that the loss of hydrophobic regions causes unfolding and makes the polypeptide more susceptible to proteolysis (278). Studies on hydrolysis or

solubilization of mature elastin using the hot alkaline method (279,281,282) also discovered the importance of unfolding the hydrophobic regions to increasing the efficiency of hydrolysis. With the addition of an organic solvent (e.g., alcohols) to the reaction solution, the hydrophobic regions of elastin were unfolded and exposed to hydrolytic attack resulting in increased reaction rate and decreased reaction temperature. For the same reason, as illustrated in Figure 4.16, the stress relaxation treatment also stretched the elastin protein for several hours, exposing the hydrophobic region for hydrolysis to occur. In addition, as the experimental group with stress relaxation time = 0 (0 h) produced no elastin fragmentation and existing studies have shown that elastin is capable of withstanding tensile strain of more than 100% (283,284), the cause of fragmentation was unlikely due to mechanical fracture but hydrolytic degradation which progresses or worsens over time. One possible location at which this hydrolytic degradation took place is the hydrophobic disulphide bonding, which are responsible for the self-assembly nature and the elastin's interaction with the microfibril scaffold of elastic fibres (277,285,286). Various studies, by means of single-molecule force spectroscopy (287–295), molecular force probes (296,297), and computational studies (298–306), have discovered a stress-induced reduction of the disulphide bond. Under tensile forces from 0 to 2 nN on a single disulphide bond, a

second-order nucleophilic substitution (S_N2) reaction, in which the hydroxide ion attacks the sulphur atom, is promoted due to a notable decrease of the activation free energy from 27 kcal/mol to about 11 kcal/mol without the addition of neither alkaline nor heat to the reaction (292,307). The result of this S_N2 reaction is the cleavage of the disulphide bond on the elastin.

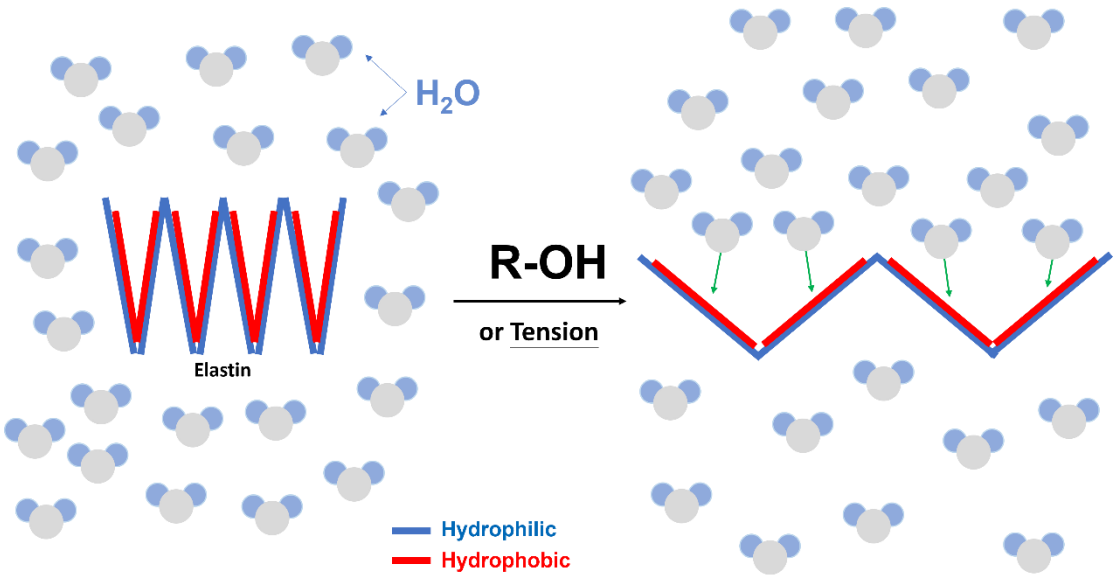

Figure 4.16. Illustration of the effect of adding alcohols or stress relaxation (prolonged tension) to the reaction solution of elastin hydrolysis. Under normal condition (left), the folded conformation of elastin shield the hydrophobic region (red bars) from the water molecules; while under tension or the addition of alcohols (right), the unfolded conformation exposes the hydrophobic region to the water molecules, allowing hydrolytic degradation to occur.

Elastin fragmentation in soft tissues could cause or trigger various health complications that would accumulate over time. For instance, cardiovascular health

issues including hypertension, arterial stiffening, calcification, and aneurysms are frequently observed in association with defects, degradation, or fragmentation in elastin (308–313). O'Rourke *et al.* in 2010 introduced a progressive deterioration in the vascular structure and function called vascular aging continuum which highlighted the fracture of elastin fibres as the main trigger (314). Due to the poor turnover rate and remodelling capability of elastin in matured tissues, although elastin is a stable and durable ECM component with longevity almost comparable with the human lifespan, they are generally irreparable for adults when damaged (271). Once damage or degradation of elastin occurs, the body tends to recover the affected region by deposition of collagens or proteoglycans (209,315), which would cause the elastic tissue to lose its extensibility and reversible recoil that allows it to withstand repeated mechanical deformation without suffering irreversible plastic damage (316). Similarly, as mentioned in the previous section, although the contribution of elastin to linear modulus is not significant in a tendon, elastin fragmentation would reduce the crimp angle and reduce the toe region which consequently predispose the collagen fibres to overstretching and plastic damage. In addition, elastin also plays a pivotal role in communication between the ECM and cells. For instance, it has been shown that functional elastin fibres promote vascular smooth muscle cells to shift from a synthetic

phenotype towards a mature, contractile phenotype by regulating the organization of specific cytoskeletal proteins (317). The loss of functional elastin not only causes mechanical, microstructural, and compositional disruptions in the ECM, the degraded or fragmentated elastin peptides are also known to be associated with the development or progression of various pathological conditions (318). These fragmentated elastin peptides or elastin-derived peptides (EDP) are liberated upon degradation of elastin mainly from the hydrophobic domains *in vivo*. Moreover, all known bioactive peptides from existing studies are derived from the non-crosslinked hydrophobic domains (318). EDPs, which consist of a type of liberated peptides known as 'matrikines' (319), are capable of regulating various cellular activities such as inhibiting elastase activity (320), inducing T-lymphocyte apoptosis (321), inducing fibroblast and monocyte migration (322), being chemotactic for white blood cells (322), acting as chemoattractants for aortic endothelial cells (323), activating phagocytic cells (324) and stimulating fibroblast proliferation (325). Some of these activities, under the normal and healthy condition, regulate tissue remodelling and maintain the health of elastic tissue. However, EDPs are also believed to promote the progression of chronic inflammation by upregulating the expression of proteases (326,327), induce cardiovascular disease including aneurysms and atherosclerosis (326,328–330), and

accelerate the progression of chronic obstructive lung disease (331,332). Although Gigante *et al.* has discovered an improved healing of the rat Achilles tendon associated with EDPs from a tenotomy with increased cellularity and vascularity (333), no other work has explored the effect of EDPs on tendon health.

4.5 Summary

A mechanical stress relaxation was performed on young bovine DDFTs to model a single manipulation/casting of the Ponseti method *ex vivo*. SEM and fluorescence IHC were performed and successfully captured microstructural details of collagen fibres and elastin fibres, respectively. Under different durations of stress relaxation (0 h, 2 h, 24 h & 48 h), the tendon tissues developed different levels of (I) tissue lengthening, (II) crimp angle reduction and (III) elastin fragmentation. The levels of these observed deviations correspond to each other under the same relaxation duration (0 h < 2 h < 24 h = 48 h). The results discovered the tissue lengthening, which is a material-based adaptation, has reached the maximum within the first 24 h, supporting the proposal of an accelerated protocol with a shorter time interval between casts of the Ponseti method (39,334,335).

The cause of tissue lengthening was primarily due to the crimp angle reduction which is a consequence of elastin fragmentation as collagen crimps are known to be maintained by elastin. Elastin fragmentation or the loss of elastic retractability is thus believed to be the main mechanism of the Ponseti method. Generally, the cause of elastin fragmentation in elastic tissues includes aging, inflammation, diseases and other pathological conditions (271,336–339). In this experiment, elastin fragmentations in young and healthy tendons were likely due to the strain-mediated hydrolytic degradation of elastin (Figure 4.16) where hydrophobic domains of elastin were forced to unfold for a long period of time, making these domains exposed to hydrolytic attacks. Further studies on elastin hydrolysis focusing on reaction kinetics are required to prove this proposed explanation.

In summary, based on this *ex vivo* experiment, elastin fragmentation is the key mechanism of tissue lengthening which is one of the objectives of the Ponseti method; however, it is also known to be an origin of the tendon's structural, mechanical and pathological issues. Therefore, how the young biological system responds to elastin fragmentation and how tendons recover the physiological function, structure and mechanical properties are the critical question for the Ponseti method.

Chapter 5: The Role of Elastin in Tendon Microstructure and Stress Relaxation

5.1 Introduction

As described earlier, each cast of the Ponseti method produces a relaxation lasting for almost a week. Based on the result demonstrated in chapter 4, this long-term mechanical treatment causes elastin fragmentation in the tendon ECM, which may suggest a potential role for elastin in tendon stress relaxation. However, to our knowledge, no study has looked at the role of elastin in stress relaxation or viscoelasticity of a tendon.

A tendon is primarily composed of collagen fibres, and they are known to provide the tissue with mechanical strength and durability to withstand significant loading. Nevertheless, as a composite material, every ECM component in a tendon shows great influence over the functional, structural, and mechanical properties of the tissue (67,76,79). The viscoelasticity of a tendon is an important mechanical property as it results in time or rate dependence in mechanical behaviour. Generally, a viscoelastic material is more deformable at lower strain rates but becomes less deformable at higher strain rates. Hence, as a tendon is strained at low rates, it would dissipate more mechanical energy but at the same time is less effective in carrying mechanical loads;

on the contrary, at high strain rates, it becomes stiffer and thus becomes more effective in transmitting large muscular loads to bone (340). The non-collagenous ECM components are believed to be responsible for the tissue's viscous characteristics and thus control the stress relaxation behaviour (67,76,79). Disruption of these components would lead to changes in the viscoelastic properties. For instance, aged tendons, which have been shown to display lower levels of PGs and elastin (341), have demonstrated a slower stress relaxation as compared to the younger tendons (342). Another example on the ground substance, which has been found to show degenerative features in an aged tendon, was demonstrated by Legerlotz *et al.* (135) who examined the effect of the removal GAG from the tendon ECM on stress relaxation and discovered an increase of stress relaxation and stress relaxation rate after GAG-removal. While studies that applied elastase treatment or elastin-deficient tendons observed decreased ultimate tensile strength and failure strain (139), increased linear stiffness (107), and decreased IFM viscoelasticity and fatigue resistance (343), the contribution of elastin to stress relaxation in a tendon remains unclear. On the other hand, extensive work has investigated the functional and mechanical role of elastin in other elastic tissues (e.g., skin, blood vessels, and lungs) rather than tendons (101,102,344–346). These tissues

are primarily elastin-rich tissues and cannot be compared to a tendon which has a relatively low elastin content (1-2% of tendon dry weight) (78,85).

Stress relaxation, which describes how a viscoelastic material relieve stress over time under constant strain, is the main mechanical event taking place in a tendon during a Ponseti casting. The most common and simple model to describe this mechanical event is the Maxwell model introduced by James Clerk Maxwell in 1867 (347). This model is composed of a spring (representing the relaxation modulus, E) connected to a dashpot (representing the viscosity, η) in series as shown in Figure 5.1. Briefly, when a tensile strain ε_0 is applied to the viscoelastic material, the spring immediately extends, and the piston would then gradually move through the viscous fluid in the dashpot. Thus, a time dependent stress response can be displayed as follow:

$$\sigma(t) = E \cdot \varepsilon_0 \cdot e^{-t/\tau} \qquad \text{(Eqn. 5.1)}$$

where τ, which is equal to η/E, is the relaxation time constant and t is the time of the experiment (347–349). Another equation used to describe the stress relaxation behaviour is the power law equation (350–353) which is shown in Eqn. 5.2

$$\sigma(t) = \sigma_c \cdot t^{-n} \qquad \text{(Eqn. 5.2)}$$

where σ_c is a constant of stress and n is the law's exponent describing the rate of relaxation (larger n indicates faster relaxation).

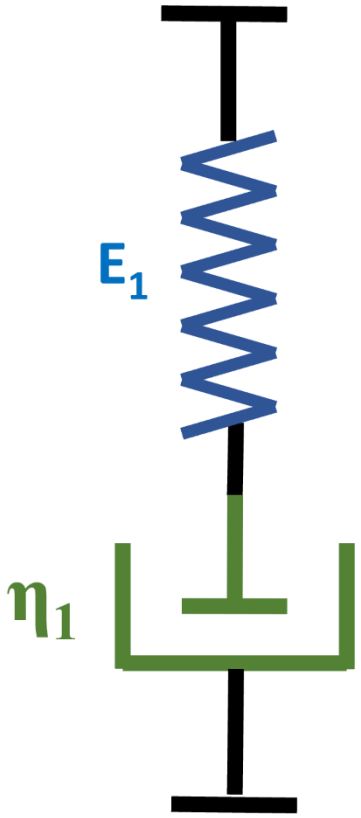

Figure 5.1. An illustrative image for the Maxwell model describing a viscoelastic material. The model contains a spring as the elastic component (modulus, E) and a dashpot as the viscous component (viscosity, η) in series. When a fixed strain is applied, the dashpot dissipates the tensile load from the spring over time.

In this chapter, the aim is to investigate the role of elastin in tendon stress relaxation by comparing the mechanical data derived from tendons (I) with and (II) without elastin in the ECM. An attempt to remove elastin from the tendon ECM was conducted by enzymatic digestion using elastase. However, a tendon tissue is known to be composed of dense collagen fibres and fibrils, thus displaying low permeability. Even

after the removal of the surface layer of fascia, molecular penetration into the bulk tissue can be challenging as shown by a work conducted by Henninger *et al.* (215) in which less than 40% of the elastin could be removed from the tendon ECM after 24 hours of elastase incubation. The low permeability issue of a tendon was also seen in studies involving tendon decellularization (354–356). To solve this problem, tendon sections of 300 µm thick were derived by cryosectioning aiming to (I) neglect the surface barrier generated by the fascia and paratenon, and (II) improve the tissue permeability by increasing the surface/volume ratio. The surface morphology of the tendon sections before and after the treatment of elastase was captured by SEM. Stress relaxation tests were also performed on the sections with and without elastase treatment. The relaxation data were then analysed using the Maxwell model.

5.2 Materials & Methods

5.2.1 Cryosectioning of Young Bovine DDFTs

Bovine DDFT sections of 300 µm thick were created following the procedures described in section 4.2.2. Briefly, fresh tendon tissues of 3-4 cm in length were cryoprotected, embedded in OCT and cryosectioned using a dry ice sliding microtome.

Before elastase treatment or mechanical testing, sections were washed in 3 changes of PBS to remove residual cryoprotectant and OCT compound.

5.2.2 Enzymatic Digestion of Elastin by Elastase Incubation

Elastin digestion was conducted by incubating the tendon sections in an enzyme solution containing 2U/ml elastase from porcine pancreas (Sigma, E1250), 0.1mg/ml soybean trypsin inhibitor (SBTI) (Fisher Scientific, 17075029), and 0.2 mg/ml sodium azide (Sigma, S2002) in PBS at 37°C for 24 h. The sections were then washed with 3 changes of PBS. Control samples were incubated in PBS or in 0.1mg/ml SBTI solution (SBTI-ctrl) at 37°C for 24 h.

The initial length (l_0) of the tendon section (long axis) before the elastase treatment and the length of the same section after treatment (l_e) were measured. The lengthening percentage was calculated using the following equation:

$$\text{Lengthening } (\%) = \frac{(l_e - l_0)}{l_0} \times 100\% \qquad \text{(Eqn. 5.3)}$$

5.2.3 Fluorescence IHC

Immunostaining of elastin in the tendon ECM was conducted to examine the effect of elastase treatment on elastin removal. Following the protocol in section 4.2.2, tendon sections were fixed with 10% formalin, permeabilized with 0.1% triton x-100 (Sigma, T8787) for 10 min, and blocked with a blocking buffer that contained 1% BSA (Sigma, A9647) and 0.05% triton x-100 for 1 hour before primary staining. Tendon elastin was immunostained with rabbit anti-elastin antibody (Abcam ab21607) as the primary antibody and with Alexa FluorTM 488 goat anti-rabbit IgG (Invitrogen, A-11034) as the secondary antibody. Cell nuclei in the tendon were stained by incubating the samples in a DAPI solution (1:1000 dilution in PBS) for 10 min at room temperature. Once staining was complete, samples were mounted on microscope slides with FluoroSave mounting media (Sigma, 345789).

Fluorescence imaging was performed on the immunostained samples using a FV1000 confocal laser scanning microscope (Olympus).

5.2.4 SEM Imaging

As described in section 4.2.2 and section 4.2.3, tendon sections were fixed in 2.5% glutaraldehyde, and dehydrated by a series of ethanol solutions and HMDS. Before imaging, samples were coated with ~6 nm of platinum. Imaging was performed using an Evo MA10 SEM (Zeiss). Crimp analysis conducted in section 4.2.3 was repeated to quantify the deviation in crimp side length (d) and crimp angle (θ) after elastin digestion.

5.2.5 Stress Relaxation Test on Tendon Sections with and without Elastin Digestion

Stress relaxation tests conducted on elastin-digested tendon sections were performed using an EZ-LZ universal testing instrument (Shimadzu) with a 200N load cell. Gripping was achieved using the default steel grips with a flat surface. No slippage was observed due to low tensile forces generated from the thin sections. Each sample was stretched at a strain rate of 0.5%/s until 8% of grip strain was reached. The sample was allowed to stress-relaxed for 1 hour with hydration maintenance using plastic film and repeated pipetting of PBS. Curve fitting of the stress relaxation data of each sample was attempted using both the Maxwell equation (Eqn. 5.1) and power law (Eqn. 5.2).

5.3 Results

5.3.1 Physical and ECM Alterations after Elastase Treatment

Tendon sections treated with elastase displayed irreversible lengthening similar to those seen in Figure 4.3 in chapter 4. The lengthening results (n = 6) are displayed in Figure 5.2. No lengthening was seen in the samples incubated in SBTI solution; and a 3.07% of lengthening was observed in the samples incubated in elastase.

Fluorescence imaging of elastase-treated sections discovered diminished elastin fluorescence level as shown in Figure 5.3. The natural elastin fibre morphology which conforms the collagen crimp morphology was lost. In addition, disruption of DAPI-stained cell nuclei where they appeared indistinct and obscure could be seen.

SEM images of tendon sections treated with PBS (PBS-ctrl), SBTI solution (SBTI-ctrl), and elastase solution for 24 h are shown in Figure 5.4. Under lower magnification (top row), loss of crimp morphology or the reduction of crimp angle could be observed after treatment of elastase; under higher magnification (bottom row), disorganized fibre orientation (deviation off the tendon long axis) was found in the elastase group.

As shown in Figure 5.5, under 5000X of magnification, which captured a surface plane within a fascicle, the directionality histograms of the collagen fibres derived by ImageJ showed a wide distribution of fibre direction in the elastase-treated tendon and an approximately $\pm 20^{o}$ of off-peak deviation of directionality in the SBTI-control group. No morphological change in collagen fibres can be found between the PBS-ctrl and the SBTI-ctrl. Quantifications of the crimp side length and crimp angle of the SBTI-ctrl and Elastase group are shown in Figure 5.6. Statistically, no difference was found in the crimp side length while an angle reduction of approximately 7.6 degree was seen after elastin digestion.

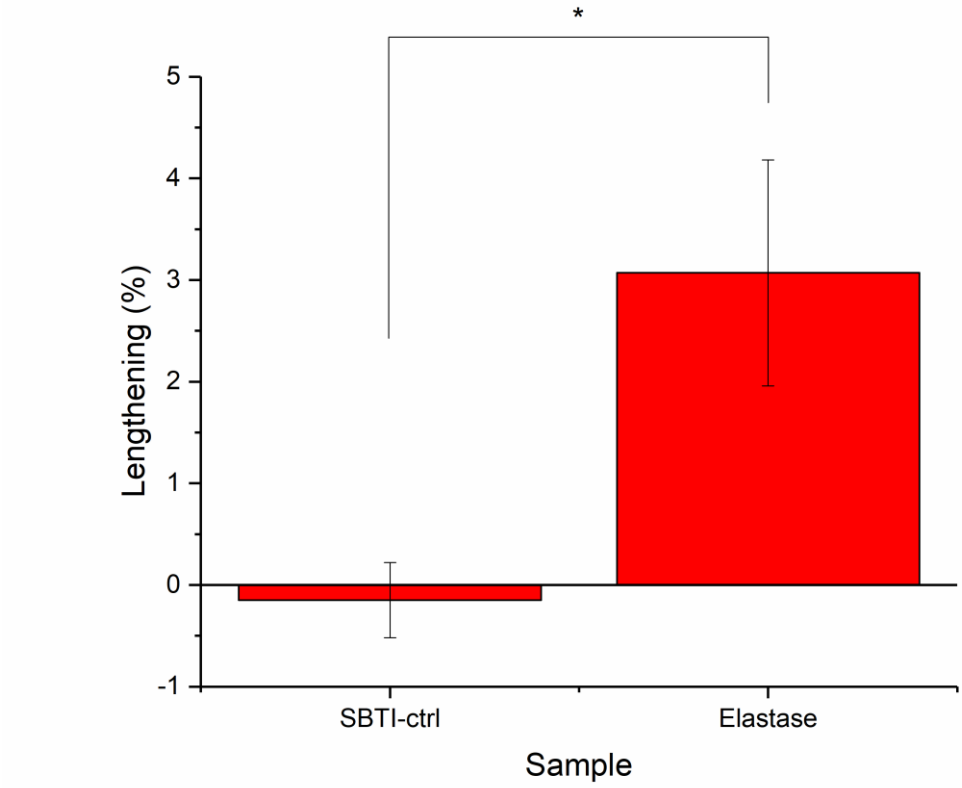

Figure 5.2. The percentage of tendon lengthening after the treatment of elastase. A control derived from tendon sections incubated with a PBS solution containing SBTI is included. All data are displayed as the mean ± SD (n=6). *P < 0.05.

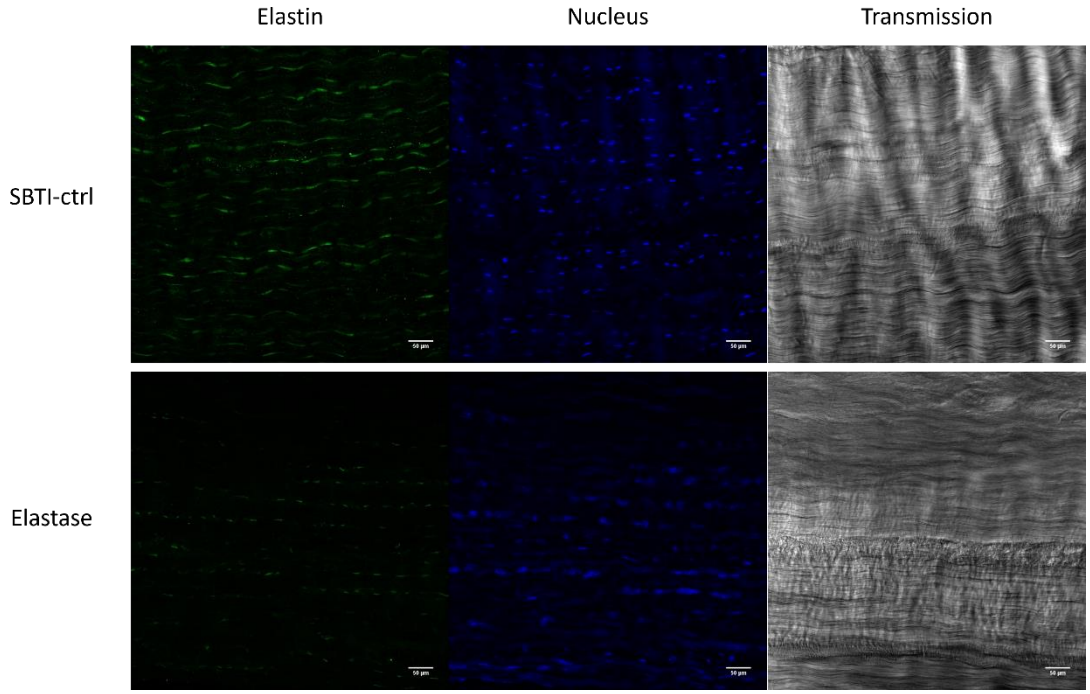

Figure 5.3. Fluorescence images of tendon sections with (bottom row) and without (top row) the treatment of elastase revealing the immunostained elastin (left column), DAPI-stained cell nuclei (mid column), and tendon matrix (right column). Scale bars are 50 µm.

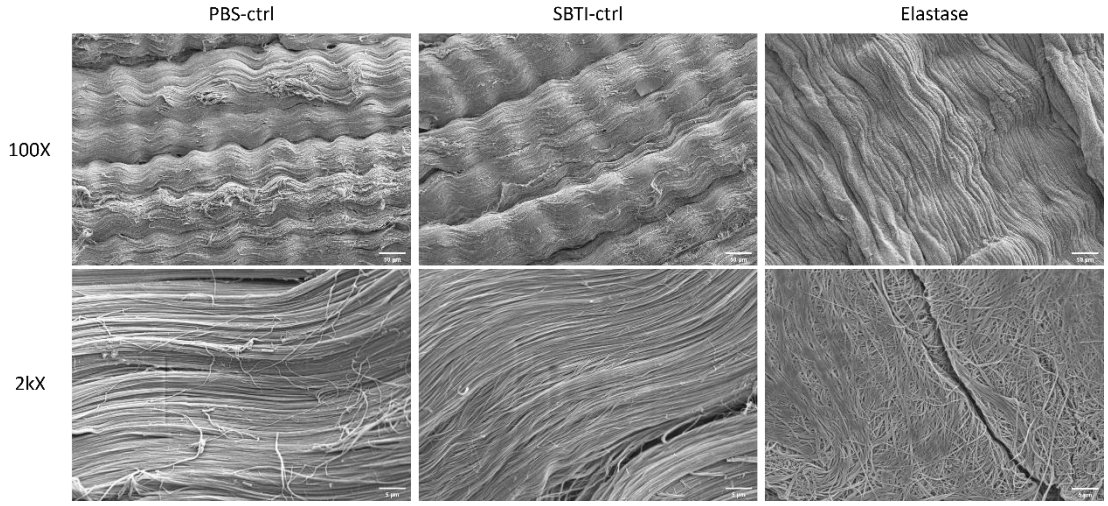

Figure 5.4. SEM images of tendon sections with (right column) and without (left row: incubated in PBS & mid row: incubated in SBTI solution) the treatment of elastase revealing the collagen fibre morphology of the tendon. Scale bars are 50 µm and 5 µm for the 100X images (top row) and the 2kX images (bottom row), respectively.

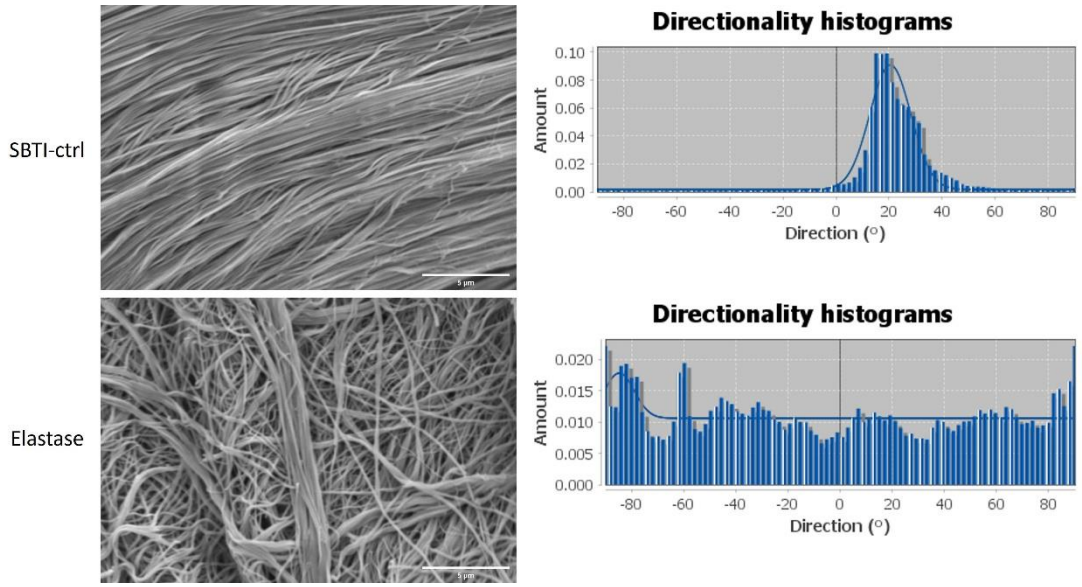

Figure 5.5. SEM images (left column) along with the histograms of directionality (right column) of tendon sections with (bottom row) and without (top row) the treatment of elastase captured under 5000X of magnification. Scale bars are 5 µm.

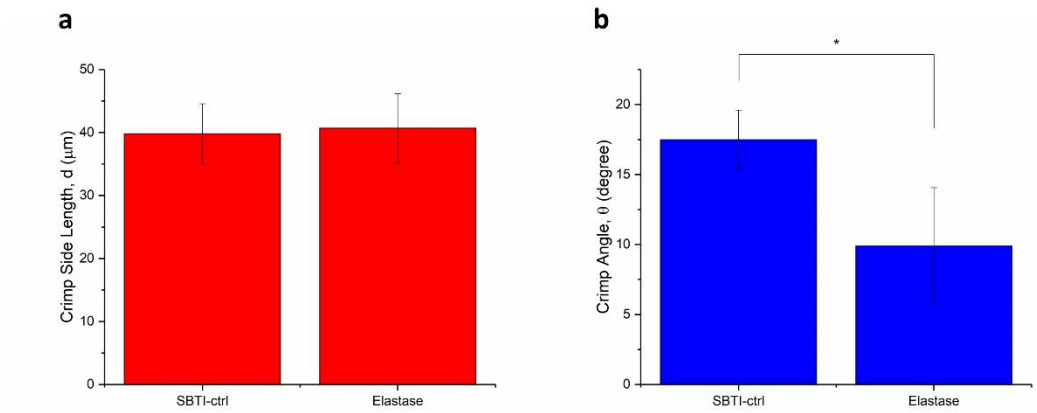

Figure 5.6. Measurement results of (a) the crimp side length and (b) crimp angle of the tendon sections treated with the SBTI solution (control) and the elastase solution. All data are displayed as the mean ± SD (n=30). *P < 0.05.

5.3.2 Alterations in Stress Relaxation Profile of a Tendon Treated with Elastase

A demonstration of the stress relaxation curves (stress-time curve) along with the curve fitting using power law and Maxwell equation is shown in Figure 5.7. From Figure 5.7, throughout the whole test, lower stress values and slower relaxation rate could be seen in the elastase-treated sample compared to the control. The percentages of the relaxed stress calculated from (I) the peak stress to the stress at t = 60 min and from (II) the stress at t = 20 min to that at t = 60 min for both the control and the elastase-treated tendons are displayed in Figure 5.8. In both cases, decreased percentages of relaxed stress were found compared to the untreated controls. Results derived from curve fitting using the power law (Eqn. 5.2) and the Maxwell model (Eqn. 5.1) are

summarised in Table 5.1. The Maxwell model was able to fit the stress-time data from time = 20 minutes after the start of the relaxation rather the whole test ($R^2 > 0.98$). A decreased relaxation rate (lower n value) was found by power fitting in elastase-treated samples. While no statistical difference was seen in either the relaxation modulus (E) or relaxation time (τ) constants, a larger τ in elastase-treated tendon, which indicates a lower relaxation rate, was derived by Maxwell equation.

(a)

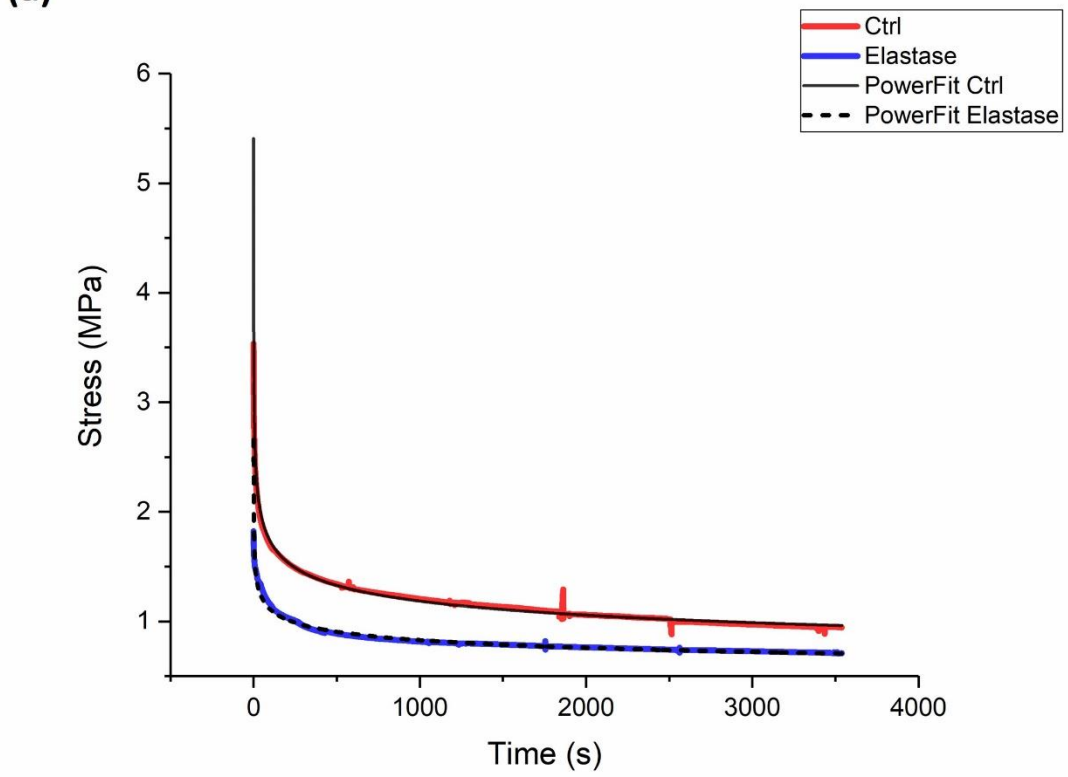
Ctrl
Elastase
PowerFit Ctrl
PowerFit Elastase
Stress (MPa)
Time (s)
1
2
3
4
5
6
0
1000
2000
3000
4000

(b)

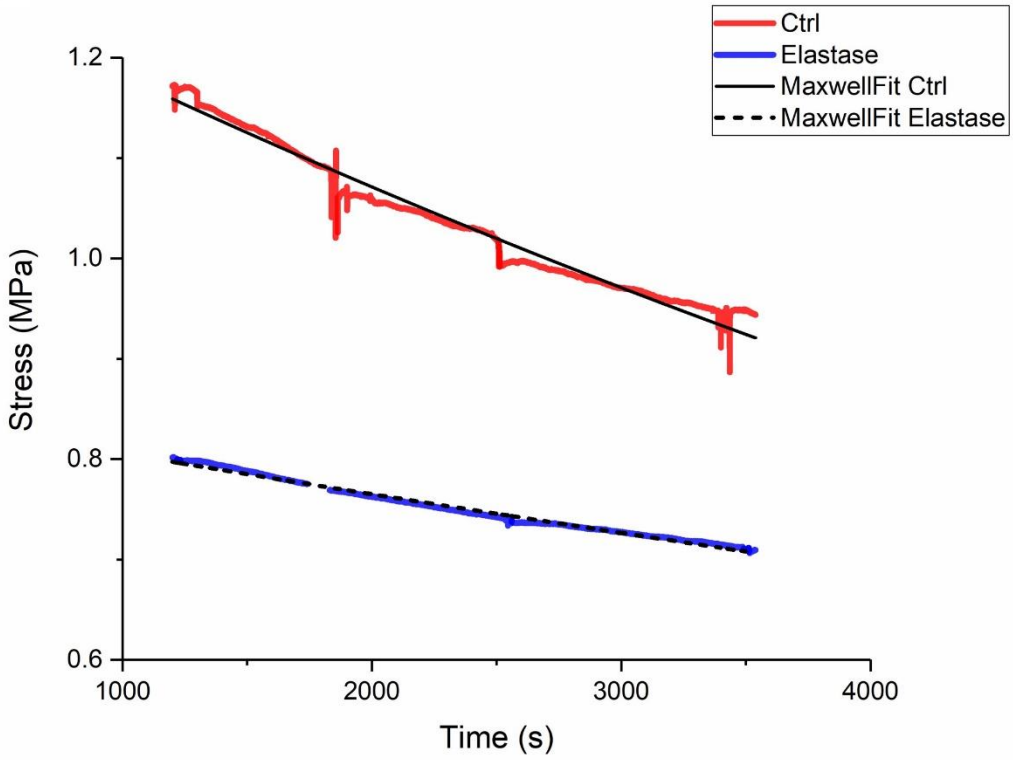
Ctrl
Elastase
MaxwellFit Ctrl
MaxwellFit Elastase
Stress (MPa)
Time (s)
0.6
0.8
1.0
1.2
1000
2000
3000
4000

Figure 5.7. Illustrative stress relaxation profiles of tendon sections with (blue) and without (red) the treatment of elastase along with the fitted curves derived from (a) power fitting of the whole curves and (b) the Maxwell fitting of stress relaxation after 20 min. Details of the curvefit constants are displayed in Table 5.1. The relaxation tests were conducted for 1 hour.

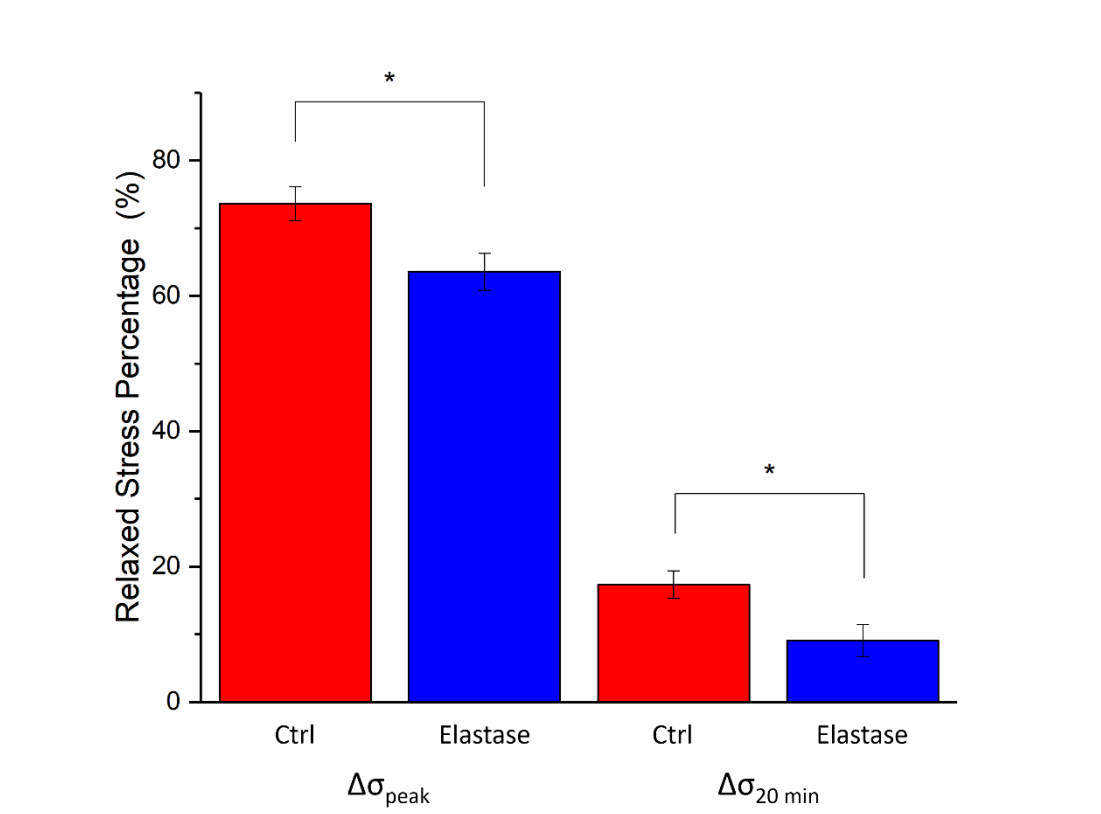

Figure 5.8. The percentages of the relaxed stress calculated from the peak stress to the stress at t = 60 min (left 2 bars) and from the stress at t = 20 min to that at t = 60 min (right 2 bars) for both the controls (red) and elastase-treated tendons (blue). All data are displayed as the mean ± SD (n=3). *P < 0.05.

Table 5.1. Tendon stress relaxation constants and exponents of elastase-treated tendon sections derived from curve fitting using the power law equation and the Maxwell equation. All data are displayed as the mean ± SD (n=3). *P < 0.05.

	Power Law	Maxwell Model (t ≥ 20 min)	
Sample	Exponent, n	Modulus, E (MPa)	Time Constant, τ (min)

Ctrl	0.164 ± 0.010	11.4 ± 1.0	226.7 ± 174.1
Elastase	0.107 ± 0.014*	10.4 ± 3.42	421.8 ± 43.85

5.4 Discussion

This chapter aims to examine the effect of elastase treatment on a tendon's stress relaxation behaviour and potentially the role of elastin in tendon stress relaxation. A 3.07% of the tendon lengthening (Figure 5.2) was generated after the incubation of elastase. This lengthening is believed to be caused by the reduction of crimp angle which was 7.6 degree as shown in Figure 5.6. As demonstrated in chapter 4, using Eqn. 4.1, the estimated lengthening produced by crimp angle reduction due to elastase treatment was calculated as 3.29% which is similar to the value acquired from the physical measurement. The result supports the proposed mechanism for the Ponseti method. The elastin digestion accomplished by elastase treatment, which simulates the functional/structural loss of elastin due to fragmentation seen in chapter 4, leads to flattening of the tendon crimp resulting in lengthening of the tissue. It is worth pointing out that although matching values of lengthening were derived from crimp angle estimation and physical measurement in this chapter, in section 4.3.1 and 4.3.2, the estimated lengthening value due to crimp angle reduction was smaller than that derived

from the physical measurement. This difference is likely due to the tissue elastic recoil contributed by the elastin exist not only in the collagen crimp but also in the interfascicular matrix (IFM) which is responsible for the reversible interfascicular sliding (108,343). A simple elastase incubation without any tension is unlikely to cause sliding between the fascicles. This result also suggest that the healthy collagen crimps are naturally pre-stressed by the elastin in the opposite direction of the normal tensile loading of a tendon since the removal of elastin causes flattening of the crimps without any loading.

Another structural disruption on the collagen matrix captured by the SEM (Figure 5.5) is the increased randomness of collagen fibre orientation (directionality) after the elastase treatment. Since several studies have shown that elastin is an important contributor to the shear and transverse mechanical properties of a tendon (214,215,233). Elastin is also thought to participate in inter-fibre load transfer (357), suggesting potential bonding between collagen fibres connected by elastin. Hence, the increase in randomness of fibre orientation may result from the loss of cohesion between collagen fibres due to elastin digestion. In addition, the treatment of elastase caused an obscureness in the DAPI-stained cell nuclei from the fluorescence images

shown in Figure 5.3. This disruption in the DAPI-stained nuclei was also seen in florescence images from a work done by Godinho *et al.* (343). As elastin in a tendon fascicle matrix is known to reside closely around the tenocytes (109) and regulate the interactions between the cells and the tendon ECM (358,359), digestion of the elastin may disturb/damage the cells localized around it.

Besides the physical and microstructural changes, elastase treatment also generated reduced stress responses (Figure 5.7 & Figure 5.8) and relaxation rate (Table 5.1) in a tendon stress relaxation test. Curve-fitting of the relaxation profile using the Maxwell model was only viable for data recorded from 20 minutes after the test. This constriction or challenge in fitting may originate the complexity of a tendon tissue. As a composite material, each ECM component can contribute to stress relaxation. For instance, Screen *et al.* (134) has shown that the collagen fibres in a tendon predominately relax stresses through inter-fibre sliding and fibre reorganization. Other studies (135,360) also explained the time-dependent microstructural changes by a diffusion thinning mechanism in which diffusion of water molecules from the PG/GAG matrix into the nano-scale collagen fibrils during stress relaxation. In short, macroscopic stress relaxation of a tendon is controlled by multiple events associated

with different ECM components; hence, a single pair of spring and dashpot may not be sufficient to describe these events. Existing studies have exploited the combination of multiple maxwell units in parallel known as the generalized Maxwell model or the Wiechert model (361,362), illustrated in Figure 5.9, to curve-fit tendon stress relaxation. However, explaining the physical meaning of each Maxwell unit and comparing the viscoelastic constants between experimental groups using this assembled model are complicated and challenging. In this experiment, for each sample, the stress relaxation behaviours before and after t = 20 min are dissimilar (higher relaxation rate before t = 20 min) as seen in Figure 5.7. It is likely that a combinational model with multiple Maxwell units would better fit the relaxation data, and that after t = 20 min, the majority of these Maxwell units became insignificant and one unit began to dominate; hence, curve-fitting with a single Maxwell unit is applicable.

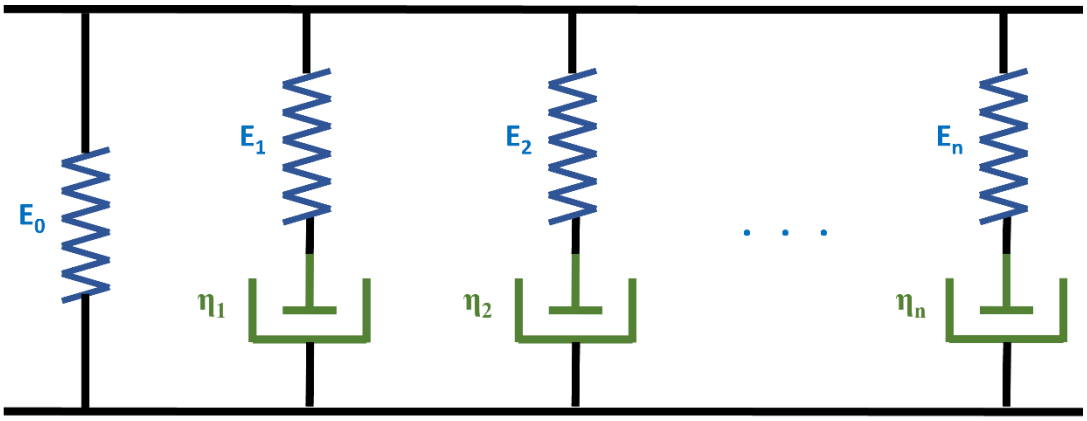

Figure 5.9. An illustrative image of a generalized Maxwell model (or Wiechert model) including multiple Maxwell units (a spring and a dashpot in series) in parallel.

Based on the results from the Maxwell curve-fitting (Table 5.1), after t = 20 min (long-term stress relaxation), an increased relaxation time constant (τ), i.e., a decreased relaxation rate, was discovered after the elastase treatment. By removing the hydrophobic elastin from the tendon, an increase in tissue water content after elastase treatment has been reported by Henninger *et al.* (215). However, this increase in tissue hydration level did not result in an increase in stress relaxation; instead, the removal of elastin, a hydrophobic elastic material, produced a slower stress relaxation. Unexpectedly, the elastin has a positive contribution to a long-term stress relaxation of a tendon. The origin of this relaxation capability may also be associated with the elastin fragmentation observed in chapter 4. An 'irreversible plastic dashpot', i.e., the dissipated part of the dashpot will not be reversible, is proposed as the role of elastin in a long-term tendon stress relaxation. A simple model will be a dashpot with a one-way valve on the piston which only allows the liquid or flowable material to pass through in the tension-damping direction. Once a tension is applied and damping has been taking effect via the piston movement controlled by liquid flowing slowly through the valve, the piston will not be able to return to its original position when unloaded, thus functioning as an irreversible plastic dashpot. As demonstrated in chapter 4, the outcome of the long-term stress relaxation is elastin fragmentation which

is speculated to be caused by exposing the hydrophobic regions of elastin to hydrolytic attacks. This strain-mediated/induced hydrolytic degradation explains why the extremely extensible elastin would experience a time-dependent fracture at a relatively small strain of 8%. Since the microstructural relaxation events discussed earlier (e.g., fibre sliding, fibre reorganization, diffusion thinning) should have reached an equilibrium state or plateaued within the first few minutes of the stress relaxation, relaxation of stresses through elastin fragmentation would then dominate over time ($t > 20$ min). This speculation also explains why the derived τ values are much higher (slower rates) than those from existing work (361,362) and why the relaxation after $t = 20$ min was much slower and subtler than that in the beginning (Figure 5.7) since these microstructural relaxation events are physical activities which plateaued within 3-4 minutes after the start of stress relaxation (134) (faster than the hydrolytic degradation) and are mostly controlled by the collagen units which are much higher in tensile strength compared to elastin. In short, the elastin contributes to stress relaxation in a tendon by relaxing the tensile loading via hydrolytic degradation of itself.

5.5 Summary

In this chapter, the effect of elastin digestion via elastase treatment on tendon stress relaxation has been experimented to examine the role of elastin. Microtome sectioning was applied on bulk tendon tissue to increase the surface/volume ratio and remove the surface barrier from the fascia layer to improve the efficiency of elastin digestion. Elastase-treated tendon samples displayed (I) the tissue lengthening and (II) the crimp-flattening feature which was also seen in the long-term stress-relaxed tendons discovered in chapter 4. Moreover, matching tissue lengthening results derived from physical measurement (3.07%) and crimp angle estimation (3.29%) of elastase-treated tendons were discovered. Increased randomness of collagen fibres in the fascicle was also observed, suggesting a contribution to inter-fibre load transfer and cohesion from the elastin. Stress relaxation results discovered (I) decreased overall stress profile and (II) decreased stress relaxation, and (III) decreased relaxation rate derived from curve-fitting using Maxwell and power law equations after the treatment of elastase. Based on these findings, elastin in the tendon ECM contributes positively to stress relaxation potentially via hydrolytic degradation, and this activity becomes more dominant compared to other relaxation events over time ($t > 20$ min).

Chapter 6: The *in Vitro* and *in Vivo* Responses of Young Tendons to a Ponseti-modelled Stress Relaxation

6.1 Introduction

With the aim to model a single Ponseti manipulation/casting, an *ex vivo* time-dependent stress relaxation experiment was discussed in chapter 4. The result showed promising tissue lengthening with no loss of mechanical strength in the linear region. Unfortunately, stress relaxation also caused the reduction of crimp angle and the fragmentation of elastin. These microstructural changes or damages resulted in the loss of extensibility in the toe region and the tissue retractability, which could predispose the fibres to overstretching and further damage (258,259). In addition, the EDPs, the bioactive fragments of elastin, have the potential to induce various biological pathways that could influence the function and health of the tendon tissue *in vivo* (319–333).

However, whether these mechanically induced observations and their levels summarised in chapter 4 will be generated in a tendon *in vivo* needs to be verified, as the biological system is way more complex than the setup in chapter 4. Additional ECM alternations other than elastin fragmentation may also be produced.

In this chapter, the aim is to study the biological response to a stress relaxation modelling the Ponseti manipulation/casting. In the first part of the chapter, a custom-made cell culture system capable of applying tensile stresses to the cells during culture was developed. To mimic the cellular response of an actual tendon in a living body, human tenocytes, which are the primary cell responsible for the formation and turnover of the ECM, and capable of reacting to mechanical stimuli and facilitate tissue adaptation (363), were seeded on decellularized bovine DDFT sections (300 μm thick). 304 stainless steel grips were used to hold both ends of the section and tension was applied using a miniature motorized linear stage (Zaber X-LSM025A-E03, Canada) connected to the steel grips. Tenocytes cultured with or without tension were compared according to their cell morphology and gene expressions.

In the second part, a rabbit model was developed for the *in vivo* experiment modelling the Ponseti method. The rabbit common calcaneal tendon (CCT) was stretched to approximately 8% of strain by manipulation and the strain was maintained by taping. This technique was applied to simulate a Ponseti manipulation/casting. After different durations of the treatment, the rabbits were sacrificed and the CCTs were collected. Histology and imaging methods done in chapter 4 were conducted on the tendons to

observe and quantify the ECM alterations. The results of the stretched tendons were compared to those of their untreated controls and the stretched tendons with different durations as well.

6.2 Materials & Method

6.2.1 *in Vitro* Tenocyte Culture under Stress Relaxation

6.2.1.1 Preparation of Tendon Scaffold for Cell Culture

Tendon sections of 300 μm thick were created following the procedures described in section 4.2.2. Briefly, fresh tendon tissues of 3 cm in length were cryoprotected, embedded in OCT and cryosectioned using a dry ice sliding microtome. After washing off the cryoprotectant and OCT using PBS, tendon sections were decellularized (native cells) by incubating the sections in a 0.1% sodium dodecyl sulphate solution (SDS) (Sigma, 74255) for 48 h to disrupt the cellular membranes. The SDS solution was prepared by dissolving SDS powder in a Tris buffer solution (Sigma 252859, UK) of pH = 8. After washing with PBS, tendon sections were treated with a solution containing DNA enzyme, deoxyribonuclease (DNase), to further remove the native DNA fragments. A concentration of 200 U/ml of the DNase (Sigma, D4527) solution was prepared in 1M sodium chloride solution. Tendon sections were incubated in the

DNase solution at 37°C for 12 h before washing with 3 changes of nuclease-free H_2O (Fisher Scientific, AM9932) with mild shaking for 24 hours.

The effect of this decellularization procedure was evaluated directly by histology and fluorescence imaging by an EvoS FL Auto 2 fluorescence microscope (Invitrogen) of the cell nuclei stained with DAPI. For histology, hematoxylin and eosin (H&E) staining was performed on the tendon scaffolds. Briefly, formalin-fixed tendon scaffolds were dehydrated through a series of ethanol solutions (50%, 70%, 80%, 95% & 100% x 3 times), cleared with xylene (Merck, 108298), and embedded in paraffin. Tissue blocks were then sectioned into 5 µm thick sections using a RM2125 RTS microtome (Leica Biosystems) and collected on microscope slides using a warm water bath. Before H&E staining, sections were first baked at 45°C overnight. The sections were de-paraffinized in 2 changes of xylene and rehydrated in a reverse series of ethanol solutions (100% x 2 times, 95% & 70%) and H_2O. Sections were then stained in Mayer's hematoxylin solution (Sigma, MHS32) for 10 min and washed in running tap H_2O for 5 min and in 95% ethanol solution for approximately 5 seconds. Once washing was complete, sections were stained in eosin solution (Sigma, HT110232) for

2 min before dehydrated with ethanol (95% and 100%) and cleared with xylene. The samples were mounted with DPX (Solmedia, REA219).

For fluorescence staining, as described in section 4.2.2, sections were first permeabilized with 0.1% triton x-100 solution (Sigma, T8787) and stained with DAPI for 10 min at room temperature. Additionally, DNA quantification, which will be discussed in the next section, was also performed on the decellularized sections to quantify the amount of residual DNA on the tendon tissue after decellularization.

6.2.1.2 Native DNA Extraction & Quantification of Tendon Scaffolds

A PureLink™ Genomic DNA Mini Kit (Life Technologies, K182000) was used to extract DNA from the cells residing the tendon tissue. Air-dried decellularized sections were cut into pieces of 20-22 mg. Each sample piece was added into a sterile microcentrifuge tube with 180 µl of PureLink™ Genomic Digestion Buffer and 20 µl of Proteinase K. Each tube was incubated in 55°C with occasional vortexing for 4 h to allow lysis to complete. To collect the lysate, each tube was centrifuged at maximum speed for 3 min and the supernatant was collected and transferred to a new microcentrifuge tube. Before proceeding to the purification protocol, 20 µl of RNase

A, 200 µl of PureLink™ Genomic Lysis/Binding Buffer and 100% ethanol were added (mixed well with brief vortexing) successively to the lysate.

The purification protocol began with preparing the wash buffers by adding 100% ethanol to the provided PureLink™ Genomic Wash Buffer I & II according to the provided instructions. The lysate mix was transferred to the provided PureLink™ Spin Column in a collection tube and centrifuged at 10,000 x g for 1 min at room temperature. The collection tube was discarded, and the remaining spin column was placed into a new collection tube before adding 500 µl of wash buffer I prepared with ethanol. The column was centrifuged again at 10,000 x g for 1 min at room temperature. The collection tube was discarded, and the remaining spin column was placed into a new collection tube before adding 500 µl of wash buffer II prepared with ethanol. The column was then centrifuged at maximum speed for 3 min at room temperature. After discarding the collection tube, the spin column was placed into a sterile 1.5-ml microcentrifuge tube. 40 µl of PureLink™ Genomic Elution Buffer provided by the kit was added to the column to allow incubation at room temperature for 1 min. Once centrifugation at maximum speed for 1 min at room temperature was completed, the solution collected in the microcentrifuge tube was saved in -20^{o}C before DNA

quantification. DNA quantification is assessed using a Nanodrop UV-VIS spectrophotometer (Thermo Scientific™, NanoDrop™ 2000).

6.2.1.3 Cell Culture with Stress Relaxation Treatment

Figure 6.1 shows the illustrative image (top) and a photograph (bottom) of the customized setup for the tenocyte cell culture. This setup consists of a miniature linear motor, custom-made 304 stainless-steel grips, a cylindrical stainless-steel chamber, a cell culture dish, and a tendon scaffold (from section 6.2.1.1) seeded with tenocytes. From figure 6.1 and figure 6.2, the steel arm on the right side could extend out from the hole of the steel chamber wall with one end fixed to stage. The other end of the arm stayed in the chamber to grip the tendon scaffold. Similarly, the steel arm on the left side, which was also used to grip the scaffold, could extend out of the chamber and attach to the motor. Under this setup, a tension can be applied to the scaffold during a cell culturing experiment. Culturing media can be exchanged from the top of the chamber by pipetting. All components except the motor were washed with soap water, sterilized using 70% ethanol or autoclave and then brought to the culture hood before cell seeding. Adult human tenocytes (OMB 0924) were extracted from an anterior cruciate ligament repair procedure in Nuffield Orthopaedic Centre with a Research

Ethics Committee approval code: 09/H0606/11. The hamstring tenocyte cells were cultured from tissue explants and expanded using a culture medium containing the Dulbecco's Modified Eagle Medium F12 (Lonza/SLS, LZBE12-719F), 10% foetal bovine serum (Labtech International, FCS-SA/500-41213.) and 1% penicillin–streptomycin (Life Technologies, 15070063). Before gripping the tendon scaffolds, the scaffolds (n=3) were sterilized in the culture hood using a series of ethanol solution (25%, 50% & 70%). Once the scaffolds were fixed on the stainless-steel grips in a warm sterile PBS bath in the chamber, the scaffolds were sterilized again in 70% ethanol. The same setup was adopted in the control group with no tension being applied during the whole experiment as shown in Figure 6.2 (left petri dish in the right image marked with a red arrow). After washing the scaffolds with 3 changes of sterile PBS, the scaffolds were immersed in the culture medium. Before cell seeding, the scaffolds were allowed to partially air-dry in the hood for 20 min to increase seeding efficiency. 100,000 cells (passage 2) were seeded dropwise onto each scaffold with a seeding volume of 63.5 µl. Once the cells have attached to the surface of the tendon scaffolds, additional culture medium (25 ml) was added to each group to allow full immersion. Cells were allowed to stabilize in the incubator for 20 h before a strain of 8% was applied to each sample by the command codes inputted using Zaber Console

software. Culture medium was exchanged for each group for every 48-h interval. The whole culturing experiment lasted 21 days.

Once cell culture was complete, each scaffold sample was cut into half with one piece fixed in 2.5% glutaraldehyde (Fluorochem, 358208) for SEM imaging and the other one used for RNA extraction. To prepare samples for RNA extraction, cultured scaffolds were immersed in 700 µl of an acid-guanidinium-phenol based reagent - TRIzol (Invitrogen, 15596). The mixture was gently mixed with repeated pipetting before storing in -80^{o}C.

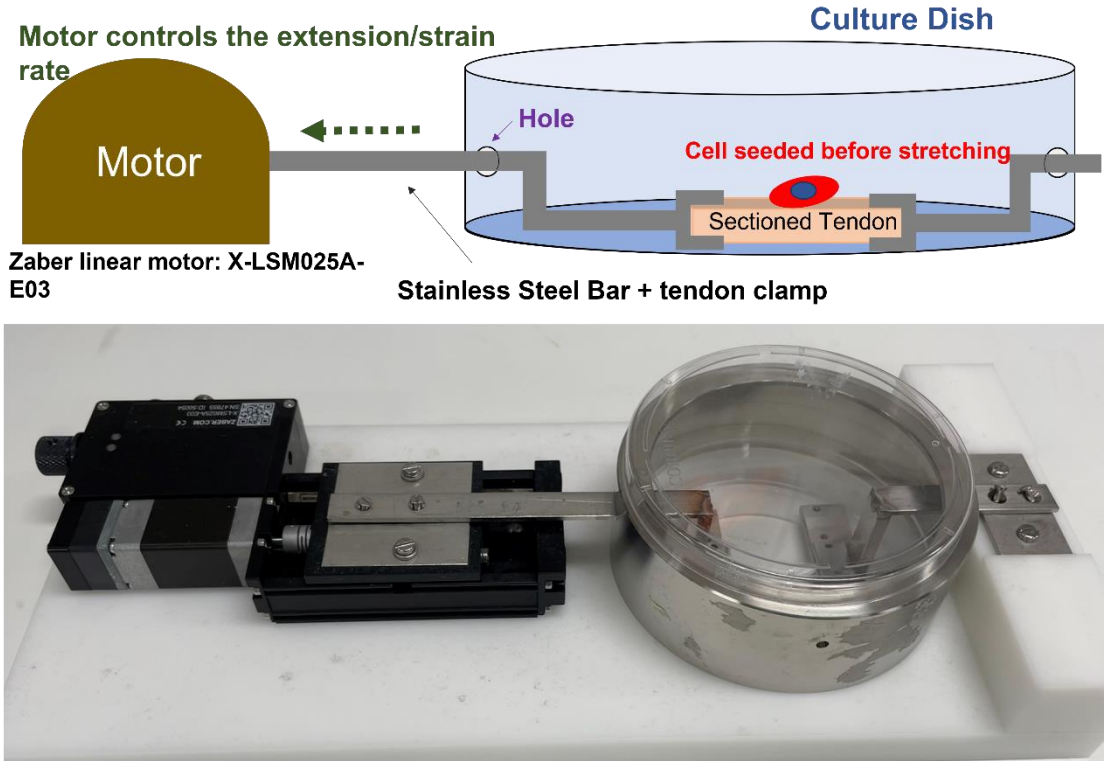

Figure 6.1. Tenocyte culture setup.

The illustrative images of the setup of the culturing system capable of performing stress relaxation during tenocyte culture. Decellularized tendon scaffolds (n=3) were gripped by 304 stainless steel arms at both ends with one side fixed and the other side connected to the motor. After cell seeding, stress relaxation was applied at a strain rate of 0.5%/s. The 304 stainless steel chamber and the cell culture cover prevented contamination during transfer and media exchange.

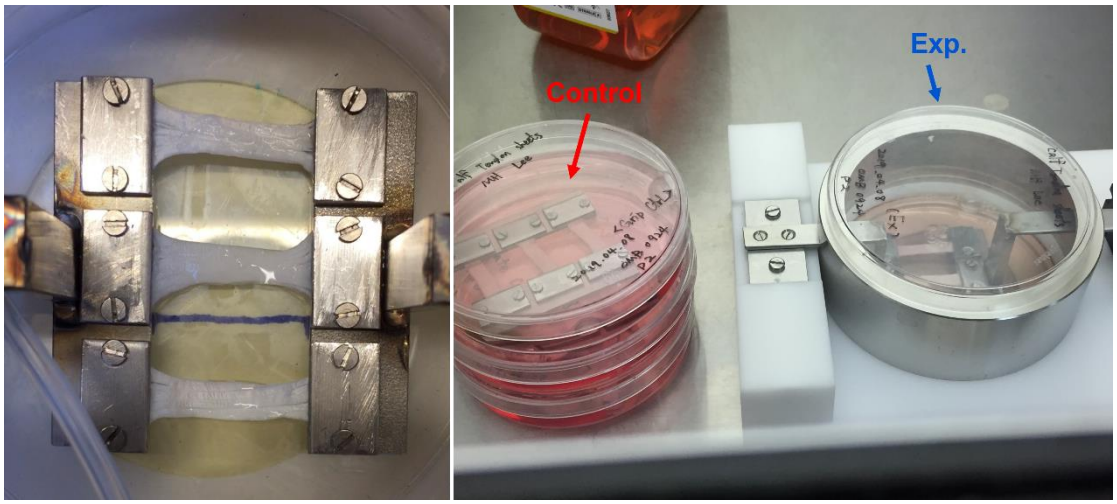

Figure 6.2. Illustrative images displaying the in-vitro experiment.
Illustration of the *in vitro* setup shown in Figure 6.1 with the insertion of tendon scaffolds. The scaffolds of the experimental groups (blue) were gripped by stainless steel arms attached to the motor; the controls (red) were also gripped by stainless steel plates and were cultured in petri dishes without any mechanical treatment.

6.2.1.4 RNA Extraction, Reverse Transcription & qPCR

RNA was extracted and isolated using a Direct-zol RNA MicroPrep Kit (Zymo Research, R2061). Briefly, the liquid phase of the tissue-TRIzol was collected and transferred into an RNase-free tube. For each tube, 700 µl of 100% ethanol was added. After mixing thoroughly, the sample mixture was transferred into a Zymo-Spin™ IC Column in a collection tube and centrifuged at 10,000 x g for 1 min at room temperature. The collection tube was discarded, and the column was transferred into a new collection tube. 400 µl RNA Wash Buffer (RNA Wash Buffer Concentrate:100% Ethanol = 1:4) was added to the column and centrifuged at 10,000 x g for 1 min. A

mixture of 5 µl DNase I (6 U/µl) and 35 µl DNA Digestion Buffer was added to the column to allow incubation at room temperature for 15 minutes to allow DNA digestion. 400 µl of Direct-zol™ RNA PreWash (Direct-zol™ RNA PreWash Concentrate:100% Ethanol = 4:1) was added to the column and centrifuged at 10,000 x g for 1 min. After discarding the flow-through, 400 µl of Direct-zol™ RNA PreWash was added and centrifuged again. 700 µl of RNA Wash Buffer was added to the column and centrifuged at 10,000 x g for 2 min. The column was then transferred to a RNase-free tube. To elute RNA, 15 µl of DNase/RNase-Free Water was directly added to the column matrix and centrifuged at 10,000 x g for 1 min. The eluted liquid containing purified RNA was collected and stored at -80°C prior to reverse transcription.

The concentrations of the purified RNA samples were measured using a Nanodrop UV-VIS spectrophotometer and all samples had 260/280 value greater than 1.6. Through dilution using nuclease-free H_2O, 215.8 ng of RNA with a solution volume of 13 µl was used to perform a reverse transcription to prepare cDNA for each RNA sample. A High Capacity cDNA Reverse Transcription kit (Applied Biosystems,

4368814) was used. Following the provided protocol, a final volume of 20 µl of sample solution was used to create cDNAs.

The quantitative polymerase chain reaction (qPCR) reaction was performed using a ViiA7 real-time PCR machine (Applied Biosystems). Final cDNA was diluted to 1.25 ng / µL and 4 µL was used in a 10 µL reaction with Fast SYBR Master Mix (Applied Biosystems, 43856) according to manufacturer's protocol. Glyceraldehyde 3-phosphate dehydrogenase (GAPDH) (Primerdesign) was used as an endogenous reference gene and gene expression was calculated using the comparative cycle threshold (CT) method according to Schmittgen and Livak (364). QuantiTect primers for COL1A1 (Primerdesign) and ELN (Qiagen) were used in the qPCR reaction.

6.2.1.5 SEM Imaging

As described in section 4.2.2, scaffolds were fixed in 2.5% glutaraldehyde, dehydrated by a series of ethanol solutions and HMDS (Sigma, 440191), and coated with ~6 nm of platinum before imaging. The surface morphology of the cells on the scaffold was visualised by an Evo MA10 SEM (Zeiss).

6.2.2 *in Vivo* Rabbit Model for the Ponseti Method

6.2.2.1 Rabbit Model

The animal work was conducted at Master Laboratory Co., Ltd. - Animal laboratory, Taiwan. Experimental procedures using animals were performed in accordance with the Institutional Animal Care and Use Committee (IACUC) guidelines (IACUC number: 20T10-10).

To model the effect of a Ponseti cast on a tendon using a rabbit foot, the correcting manipulation for hindfoot equinus, which is last correction for clubfoot, was chosen for the model. Three adult New Zealand White (NZW) rabbits were used for the preliminary experiments and measurements. Like the situation in a human equinus correction where the Achilles' tendon or the CCT is stretched, the CCT of a rabbit foot was also stretched by manipulation, and the resulting engineering strain of the CCT was measured. To perform the measurement, after the rabbit was anesthetized by the injection of Telazol (50 mg/ml) into the muscles of the rabbit (0.12 ml/kg), the fur of the foot was shaved with electric animal shaver, and the skin covering the calf muscle and the CCT was removed using surgical blades. Two markings were made using a marker pen to create two reference points. The initial length (L_0) between the two

reference points was measure before stretching. Through manipulation, the knee was straightened while the foot was slowly dorsiflexed to an angle of approximately 100° to create an elongation and tension on the CCT as shown in Figure 6.3. The final length (L) of the two reference points on the CCT due to this manipulation was measured. The mean strain ($\bar{\varepsilon}$) (n = 6) created by the manipulation to produce a strain value of approximately 8% on the CCT was calculated using the following equation:

$$\bar{\varepsilon} = \sum_{i}^{n} \frac{(L_i - L_{0,i})}{L_{0,i}} \Big/ n \qquad \text{(Eqn. 6.1)}$$

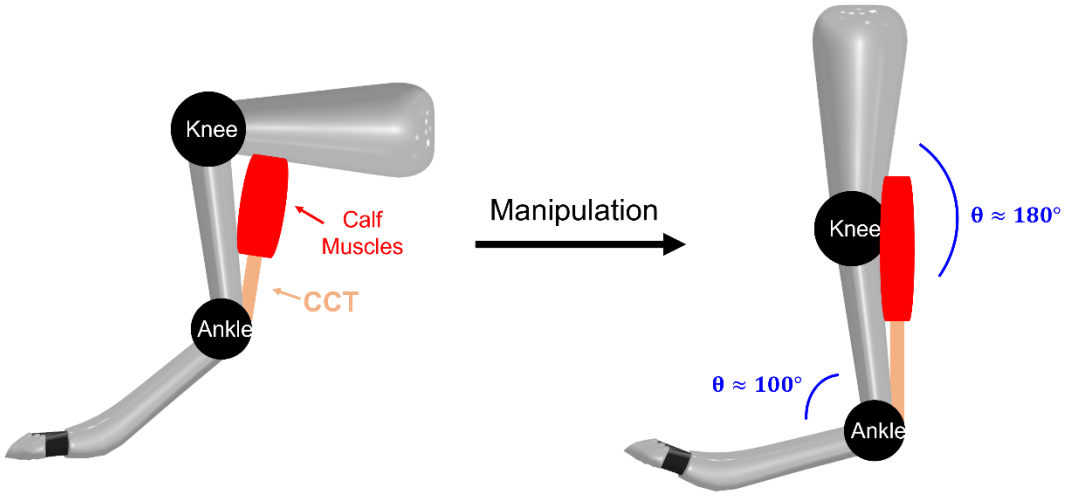

Figure 6.3. Illustrative image of the manipulative procedure.
The manipulation was done by straightening the knee followed by dorsiflexing the foot to approximately achieve a 100-degree angle between the foot and the tibia. This manipulation aims to produce an 8% strain on the rabbit CCT.

Eight 45-day-old NZW rabbits, shown in Figure 6.4, were used in the animal study. For every foot to be manipulated, the fur was shaved with electric animal shaver. Similar to the procedures mentioned in the previous paragraph, the knee was straightened and fixed with taping, and the foot was then slowly dorsiflexed to an angle of approximately 100^{o} and fixed with taping (right image of Figure 6.4). The whole manipulative procedures were done without anesthetization. The progression of the dorsiflexion of the rabbit foot would be stopped and fixed before reaching an angle of 100^{o} if the animal displayed any sign of pain during the process. For every rabbit, only one foot received manipulation and taping while the other foot was left untreated and free to use as a control. Because 1 day of stress relaxation produced the maximum level of ECM alterations in chapter 4, and a 7-day casting is normally practiced in the Ponseti method, taping in this study was maintained for 2 different durations (2 experimental groups): 1 day and 7 days before euthanasia with CO_2. Four rabbits (n = 4) were studied in each experimental group. The design layout of the animal work was illustrated in Figure 6.5. As the CCT of a rabbit is composed of 2 tendons: a superficial digital flexor tendon (SDFT) and a gastrocnemius tendon (GT), both tendons were dissected and analysed, separately.

Figure 6.4. Demonstrative images of the 45-day-old NZW rabbit (left) and the tapping to produce an 8% strain on the CCT (right).

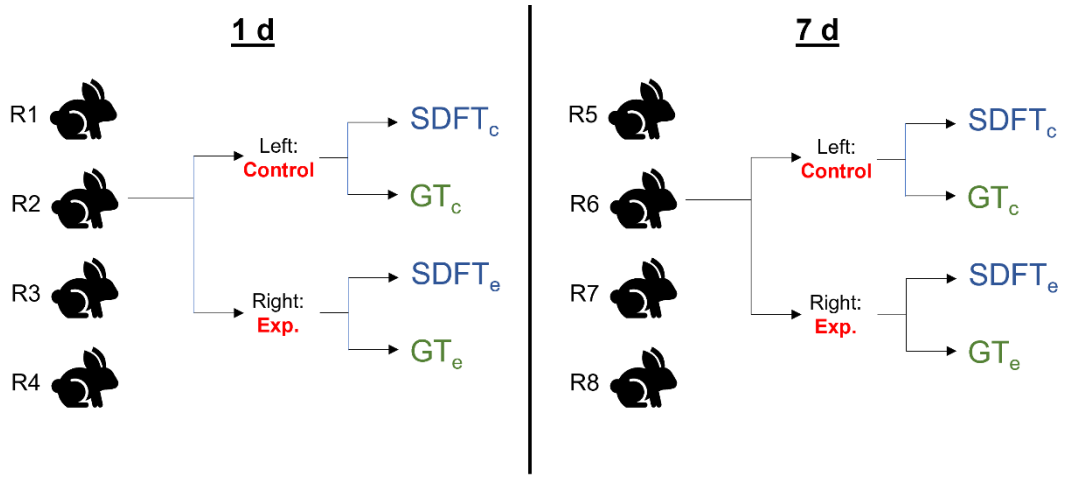

Figure 6.5. Illustrative images of the experimental design of the rabbit study. Experimental layout of the rabbit study displaying the experimental groups (1 d & 7 d), the tested tendons (GT & SDFT), and the control samples.

6.2.2.2 SEM

As described in section 4.2.2 and section 4.2.3, fresh rabbit SDFTs and GTs were cryoprotected, sectioned into 50 µm thick sections using a CM1800 cryostat (Leica Biosystems). The microstructure and collagen crimp morphology of the tendon

samples were observed by SEM. Prior to imaging, the sample sections were fixed in 2.5% glutaraldehyde, dehydrated in ethanol solutions in ascending concentrations and HMDS (Alfa Aesar, A15139), and coated with ~6 nm of gold. Imaging was performed using a JSM-6360 SEM (JOEL).

The crimp angle (θ) and fibre side length (d) in each crimp were measured (30 sets of data points) using ImageJ to compare the crimp morphology changes between the treated group and the control group from the same rabbit.

6.2.2.3 Fluorescence IHC

Following the protocol in section 4.2.2, tendon sections (50 μm) were fixed with 10% formalin, permeabilized with 0.1% triton x-100 (Sigma, T8787) for 10 min, and blocked with a blocking buffer that contained 1% BSA (Merck, P02769) and 1% goat serum (Sigma, G9023) for 1 hour before primary staining. Tendon elastin was immunostained with rabbit anti-elastin antibody (Abcam, ab21607) as the primary antibody and with goat anti-rabbit IgG (H+L)-FAM (LEADGENE®, 21001) as the secondary antibody. Cell nuclei in the tendon were stained during mounting using a

DAPI mountant (Sigma, F6057). Fluorescence imaging was performed using a LSM 700 confocal laser microscope (Zeiss).

Elastin fragmentation ratio were measured and analysed using ImageJ. The level of elastin protein for each sample was also quantified by measuring the mean fluorescence intensity of the images (n=16) of each experimental group using ImageJ. Following the equation displayed below:

$$\frac{\Delta I_{7d}}{\Delta I_{1d}} = \frac{(I_{7d} - I_{7d,\,ctrl})/I_{7d,ctrl}}{(I_{1d} - I_{1d,\,ctrl})/I_{1d,ctrl}} \qquad \text{(Eqn. 6.2)}$$

for each type of tendon, the intensity difference between the treatment group and the control normalized by the control intensity was first calculated. The calculated intensity differential ratio of 7 d to 1 d was derived.

6.2.2.4 Histology

Tendon tissues fixed in 10% formalin were transported to BioLASCO Taiwan Co., Ltd. for sample preparation for histological staining. Briefly, tendon samples were dehydrated using the Histo-Tek® VP1 Vacuum Tissue Processor (Sakura), cleared with xylene (BURNETT, 00015B1) and embedded in paraffin. Tissue blocks were sectioned into 4 μm thick sections using an AEM460 microtome (Amos Scientific).

H&E staining (Leica Biosystems, 3801522 & 3801602) was then performed on the tendon sections using a DRS-2000 automated slide stainer (Sakura). Imaging was done by an optical microscope (Olympus).

Quantification of vascularity of the ECM was performed using ImageJ. Briefly, the ratio (R_v) of the area sum of vascular regions within the ECM over the total ECM area was derived for every single section. The change of vascularity (ΔV) due to the stress relaxation treatment was then calculated using the following equation:

$$\Delta V = {(R_{v,stress-relaxed} - R_{v,ctrl})}/{R_{v,ctrl}} \qquad \text{(Eqn. 6.3)}$$

Quantification of cell number in the rabbit tendon ECM was performed on images acquired from DAPI-stained sections. The mean number of cells (n = 10) captured over the total area of an image (N) was derived using particle analysis in ImageJ for each rabbit. The change of cell number (ΔN_{cell}) due to the stress relaxation treatment was then calculated using the following equation:

$$\Delta N_{cell} = {(N_{stress-relaxed} - N_{ctrl})}/{N_{ctrl}} \times 100\% \qquad \text{(Eqn. 6.4)}$$

6.3 Results

6.3.1 *in Vitro* Tenocyte Culture under Stress Relaxation

6.3.1.1 Decellularization of Tendon Scaffold – Fluorescence Microscopy & DNA Quantification

The results of decellularization using SDS solution was shown by fluorescence imaging in Figure 6.6. Compared to the control, in which the long, thin, and spindle-shaped nuclei of the tenocytes could be seen to be scattered in the matrix of collagen fibres, the fluorescence signals in the SDS-treated tendon showed only the background noise (wavy patterns) from the collagen fibres under higher excitation intensity. H&E staining, shown in Figure 6.7, further confirmed the removal of cells from the collagen matrix of a tendon post-treatment. After the incubation of DNase, the concentrations of residual DNA in the tendon scaffold are displayed in Figure 6.8. The result showed that the combination of SDS and DNase treatment was able to remove approximately 46% of the DNA materials in the tissue.

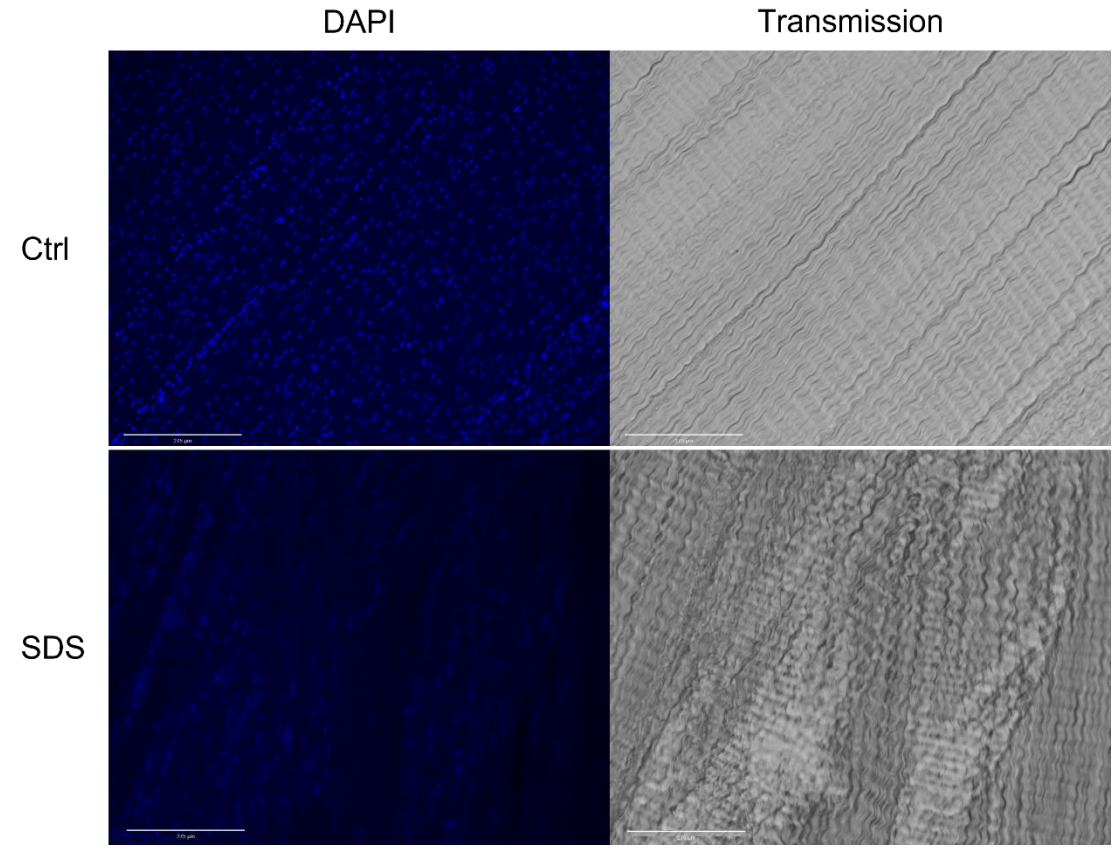

Figure 6.6. Decellularization results revealed by fluorescence DAPI staining. The fluorescence images of DAPI-stained cell nuclei (left column) in the tendon ECM along with the transmission channel (right column) from DDFT samples treated with and without decellularization (control). Scale bars are 275 µm.

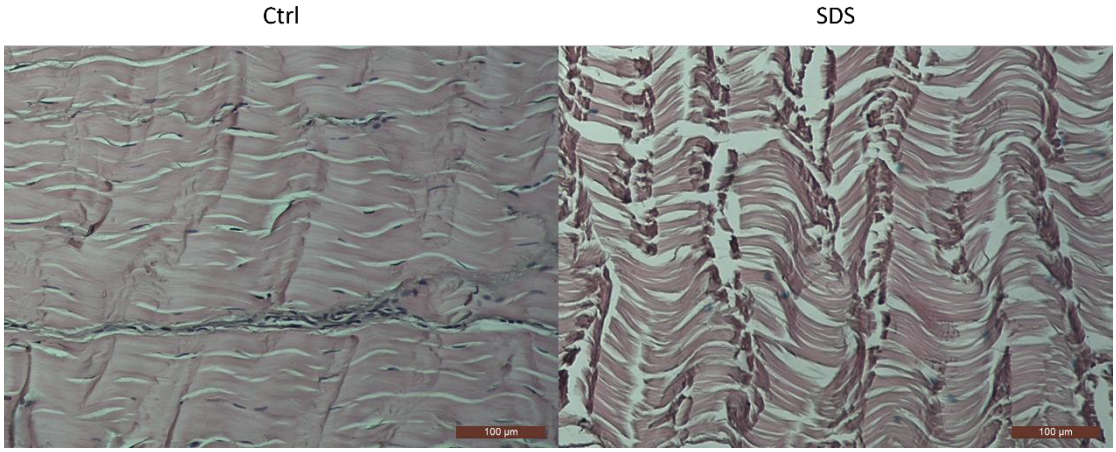

Figure 6.7. Decellularization results revealed by H&E staining. Tendon ECM stained by H&E from DDFT samples treated with and without decellularization (control). Scale bars are 100 µm.

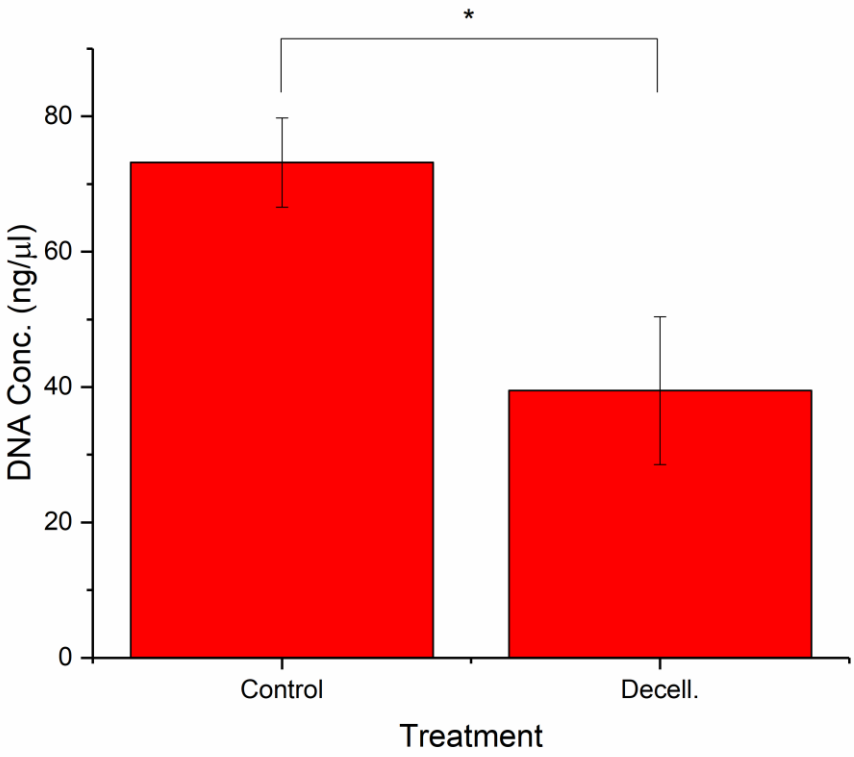

Figure 6.8. Quantification of residual DNA in the tendon after decellularization. DNA concentrations in tendon ECM from samples treated with and without decellularization (control). All data are displayed as the mean ± SD (n=3). *P < 0.05.

6.3.1.2 Cellular Response to a Long-Term Stress Relaxation

SEM imaging revealed a drastic morphological change of stress-relaxed tenocytes compared to those in the control group. As shown in Figure 6.9, stress-relaxed tenocytes displayed a more elongated shape than the unstretched tenocytes (marked by red arrows). Since chemical fixation was conducted after the tension was removed, this morphological elongation of tenocytes was likely an active adaptation to the tension during culture rather than a passive elongation due to stretching. The result

from qPCR, which is displayed in Figure 6.10, showed upregulation on both gene expressions of COL1A1 and ELN from tenocytes stress-relaxed for 21 days compared to the control.

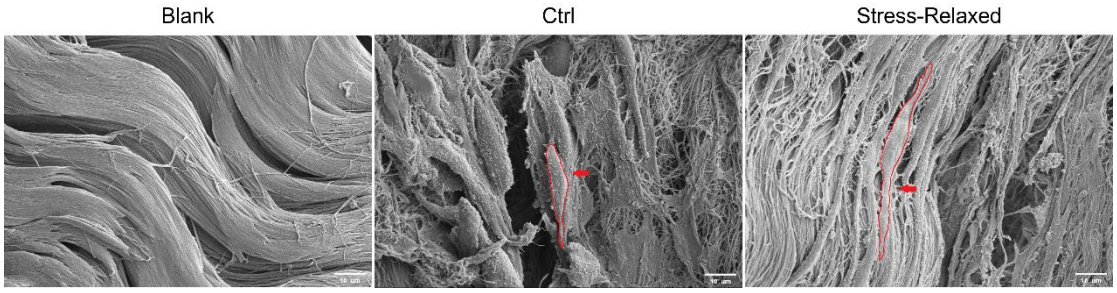

Figure 6.9. SEM images of the decellularized tendon sections or scaffolds.
The decellularized tendon scaffold: blank scaffold with no cell seeding (left), the scaffold seeded with human tenocytes without stress relaxation (mid), and the scaffold seeded with human tenocytes treated with stress relaxation for 21 d (right). Seeded tenocytes are marked with red lines and red arrows. Scale bars are 10 μm.

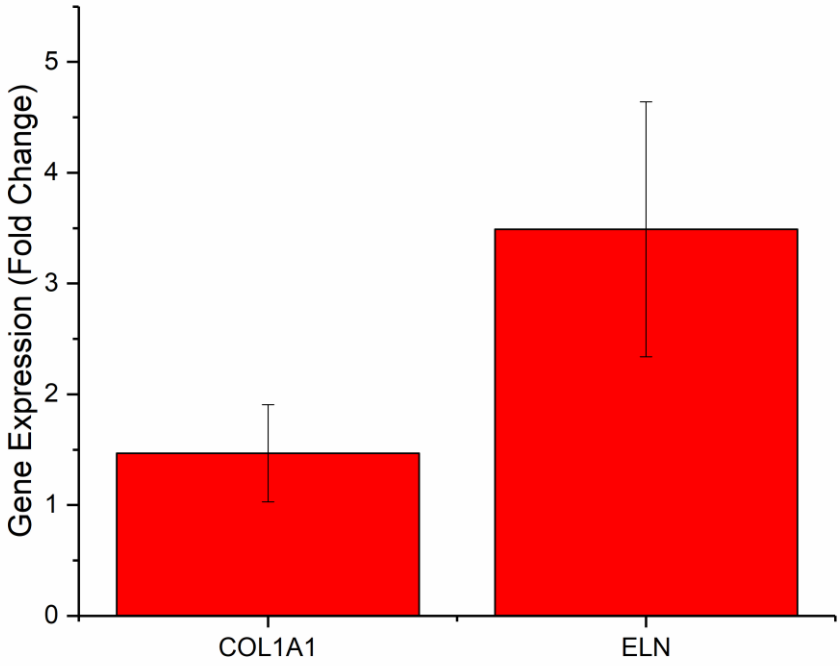

Figure 6.10. Elastin and collagen type I gene expression levels due to the treatment of stress relaxation. Fold changes of gene expressions of COL1A1 and ELN of human tenocytes cultured on decellularized tendon treated with 21-d stress relaxation compared to tenocytes without stress relaxation. Data are displayed as the mean ± SD (n=3 for COL1A1 and n=2 for ELN). One data point of ELN level was excluded as an outlier. Significant differences were analysed by 2-sample t-test. No statistical difference was found in all groups in both experiments.

6.3.2 *in Vivo* Rabbit Model for the Ponseti Method

6.3.2.1 Rabbit Model

For both experimental groups (1 d & 7 d), no rabbit died nor was forced to terminate the experiment due to the manipulation and taping. Redness and swelling can be seen on the muscles at the back of the leg as displayed in Figure 6.11 (left). Once sacrificed,

the CCT was collected for each rabbit. As illustrated in Figure 6.12, both stress-relaxed tendon-muscle units from the 1 d and 7 d groups showed appearance of redness and swelling compared to their controls, while apparent lengthening of the tendon-muscle unit was only seen on samples from the 7 d group. For tendon samples collected from 2 rabbits in the 7 d group, blood vessels in parallel with the long axis were observed in the centre of the tissue (Figure 6.13). Further investigation through histology will be elaborated in section 6.3.2.4.

Figure 6.11. Demonstrative image of a 45-day-old NZW rabbit after the stress relaxation treatment via manipulation and tapping. Redness and swelling can be seen on the muscles at the back of the left leg.

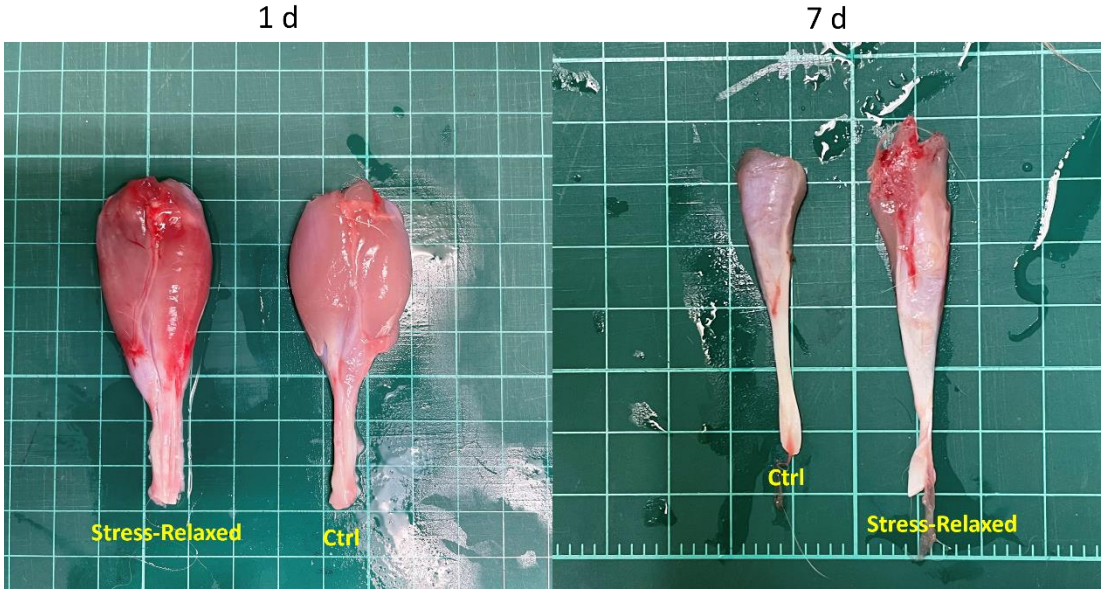

Figure 6.12. Demonstrative images of the CCT-muscle complex collected from NZW rabbits treated with stress relaxation for 1 day (left image) and 7 days (right image).

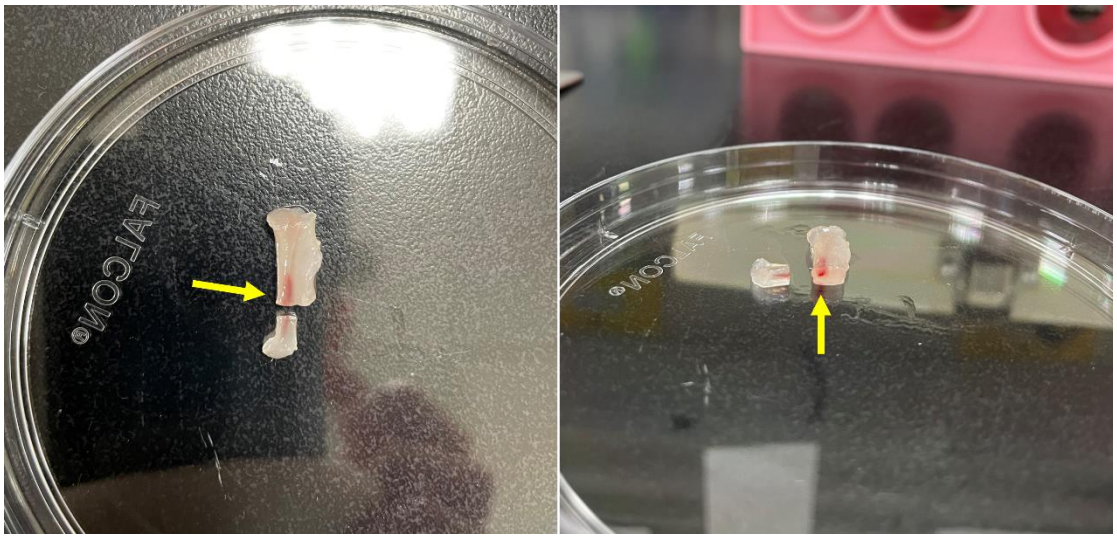

Figure 6.13. Demonstrative images of blood vessels presenting in rabbit CCTs which were stress-relaxed for 7 days. CCT samples were incubated in 30% sucrose cryoprotectant to increase transparency.

6.3.2.2 Tendon Crimp Analysis

Collagen crimp morphologies of the stress-relaxed GTs and SDFTs (1 d and 7 d) are illustrated in Figure 6.14. Similar to the results demonstrated in section 4.3.2, besides the relaxation/reduction of collagen crimps, no structural damage was observed in the stress-relaxed tendons compared to the controls. As displayed in Figure 6.14, both the GT and SDFT of young rabbits stress-relaxed for 7 days appeared to show lower levels of crimp angle reduction compared to those of rabbits stress-relaxed for 1 day. The mean crimp angle reduction ($\Delta\theta$) calculated based on the control foot of each individual rabbit of the 1 d and 7 d experimental groups are shown in Figure 6.15. For both the GT and SDFT, lower values of angle reduction were spotted in the 7 d group compared to the 1 d group. Unlike the *ex vivo* stress relaxation experiment in chapter 4, the $\Delta\theta$ value for the 1 d experimental group was slightly lower for the rabbit tendons. In addition, instead of plateauing after 1 day, the $\Delta\theta$ value has decreased over time (day 7), suggesting the possibility of the restoration of collagen crimp.

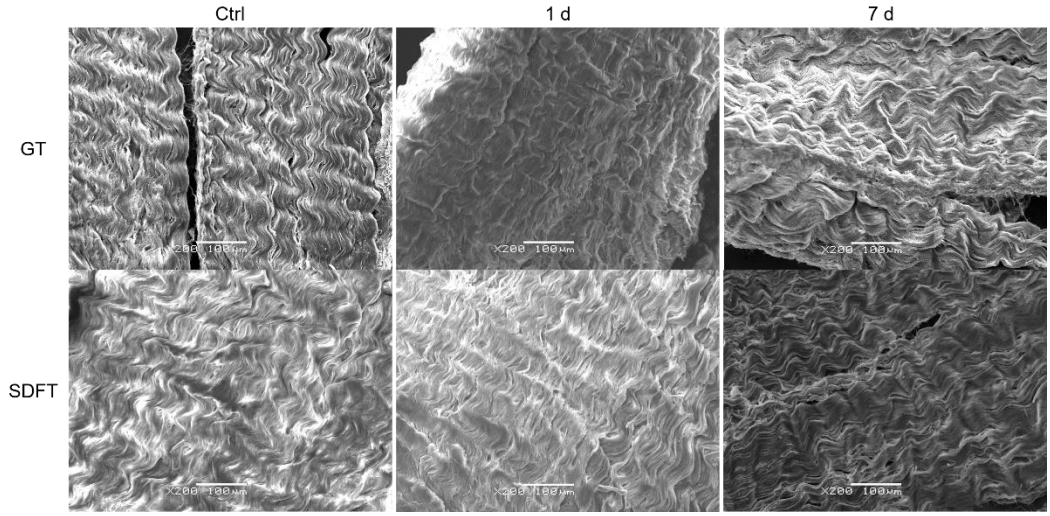

Figure 6.14. SEM images of the tendon sections.
Tendon surface morphology of the young rabbit GT (top row) and SDFT (bottom row) sections of the control (left column), the foot stress-relaxed for 1 d (mid column), and the foot stress-relaxed for 7 d (right column). Scale bars are 100 μm.

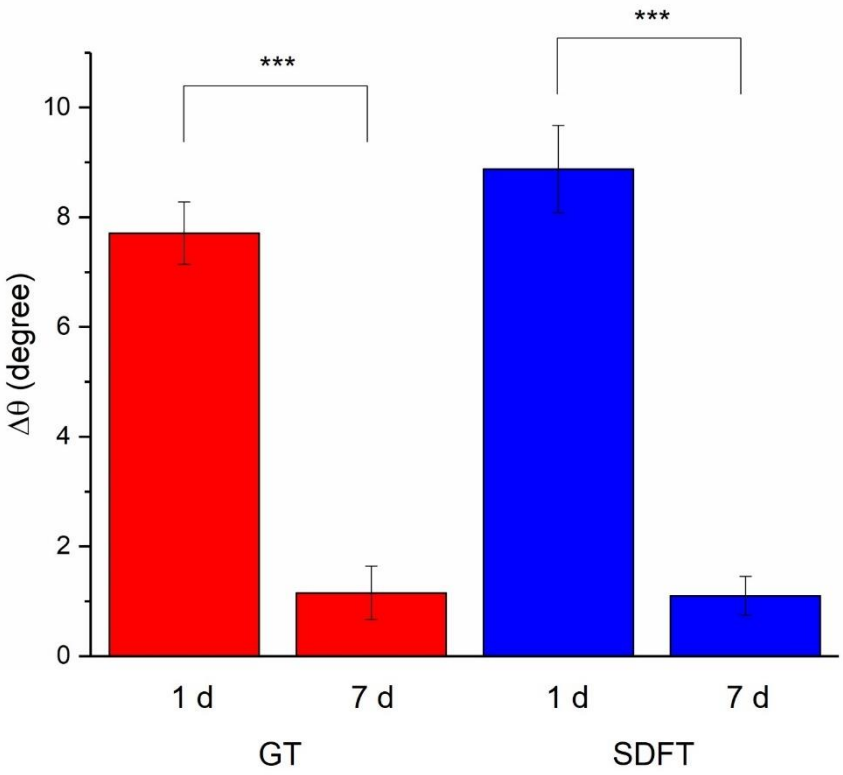

Figure 6.15. Summary of the values of crimp angle reduction due to stress relaxation. The amount of the crimp angle reduced after the treatment of stress relaxation plotted

over different relaxation durations (1 d & 7 d) for both GT and SDFT of the young rabbits. Data are displayed as the mean ± SD (n=4). Each Δθ value is calculated by subtracting the stress-relaxed angle from the mean angle of the control ($\overline{\theta_{ctrl}} - \theta_{exp.}$). Significant differences were analysed by 2-sample t-test. *P < 0.05, ***P < 0.001.

6.3.2.3 Elastin Fragmentation, Elastin Fluorescence Level, and Cell Number

Fluorescence images of the stress-relaxed GT and SDFT derived from IHC are illustrated in Figure 6.16(a) and Figure 6.16(b), respectively. For tendons treated for 1 day, like the results demonstrated in chapter 4, elastin fragmentation could be spotted in the ECM. For the 7 d group, on the other hand, (I) fewer elastin fragments, (II) larger regions of intact elastin fibres and (III) higher overall elastin fluorescence intensity compared to the 1 d group were observed.

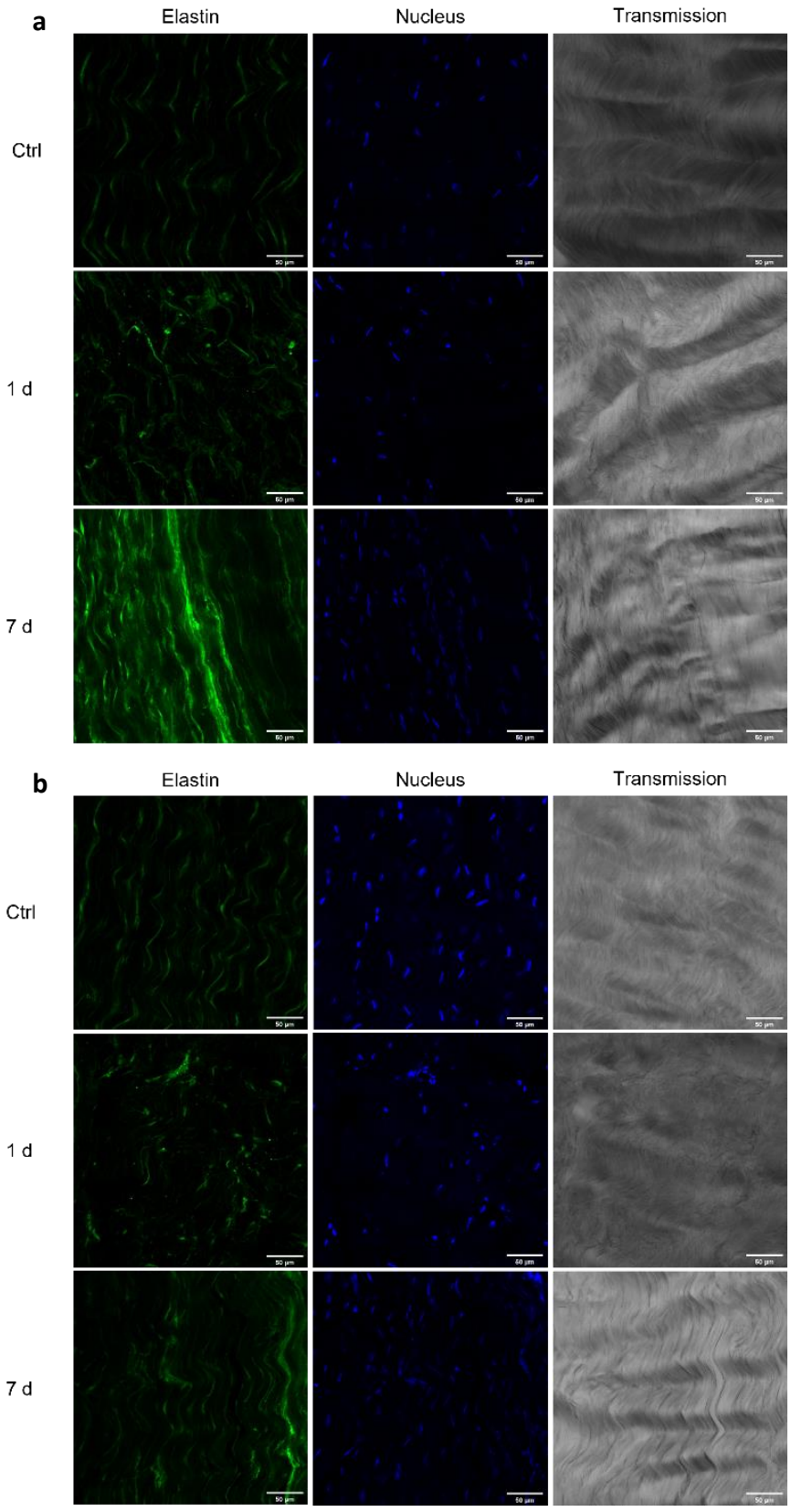

Figure 6.16. Representative immunostained tendon images captured by confocal microscopy revealing the morphology of elastin (green), cell nuclei (blue) and tendon

matrix (grey) in (a) a rabbit GT and (b) a rabbit SDFT after the treatment of stress relaxation for 1 d & 7 d. Examples of elastin fragmentation caused by stress relaxation appear as aggregated clusters with higher fluorescence intensity compared to the intact elastin fibres. No elastin fragment can be found in the controls. Scale bars are 50 μm.

The results of the quantifications of the elastin fragmentation and the elastin fluorescence level are displayed in Figure 6.17 and Figure 6.18, respectively. Quantification of elastin fragmentation (Fig. 6b) also found decreased values of fragmentation ratio in the 7 d group for both GT and SDFT, which again coincides with the findings in crimp angle reduction, i.e., lower $\Delta\theta$ corresponds to lower elastin fragmentation ratio. The decrease in elastin fragmentation ratio implies potential healing/remodelling taking place after day 1. Nevertheless, compared to the results of crimp angle reduction, smaller gaps were seen between the fragmentation ratios of the 1 d group and the 7 d group for both GT and SDFT. The change of elastin level (Figure 6.18) in the ECM of rabbit CCTs was quantified based on the fluorescence intensity from IHC. For both tendon types, the increase of elastin fluorescence level of the 7 d group was 2-4 times higher than the 1 d group. Regarding the change in cell number (ΔN_{cell}) shown in Figure 6.19, GT displayed an increase in ΔN_{cell} (+61.4%) in day 7 compared to day 1; while SDFT displayed a decrease in ΔN_{cell} (-71.7%) in day 7 compared to day 1.

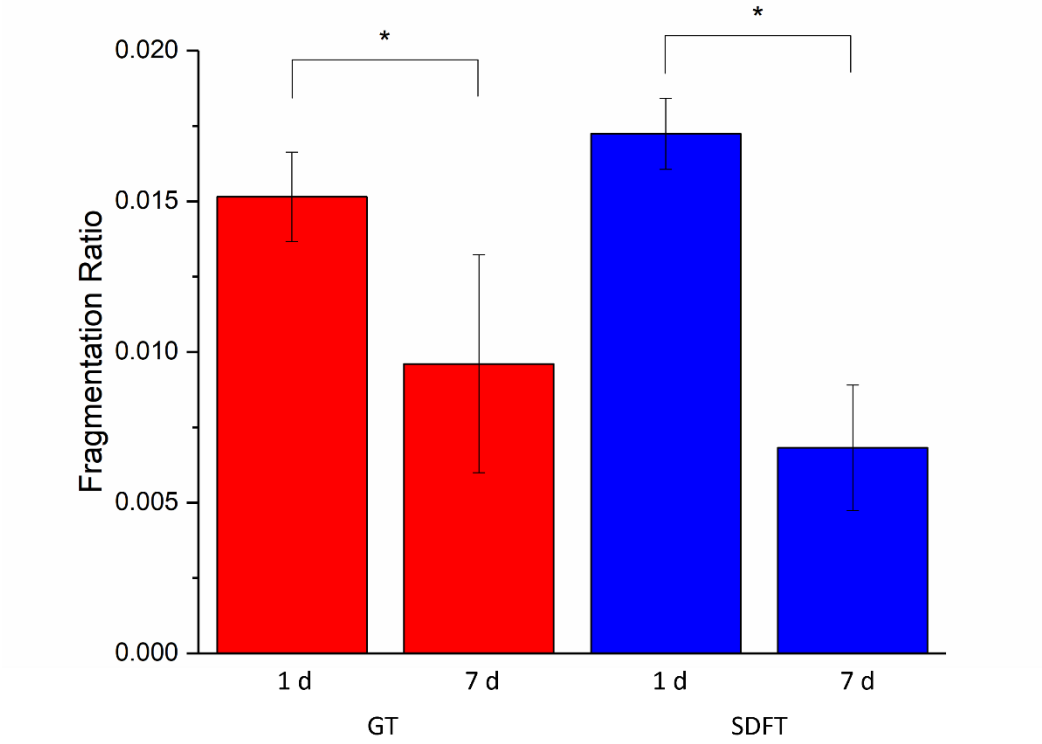

Figure 6.17. The elastin fragmentation ratio in the tendon matrix after the treatment of stress relaxation.

Values of fragmentation ratio of young rabbit GTs and SDFTs treated with stress relaxation for 1 d and 7 d. Fragmentation ratio is defined as the total area of elastin fragments over the image area (tendon matrix area) for each fluorescence image. Data are displayed as the mean ± SD (n=4). Significant differences were analysed by 2-sample t-test. *$P < 0.05$.

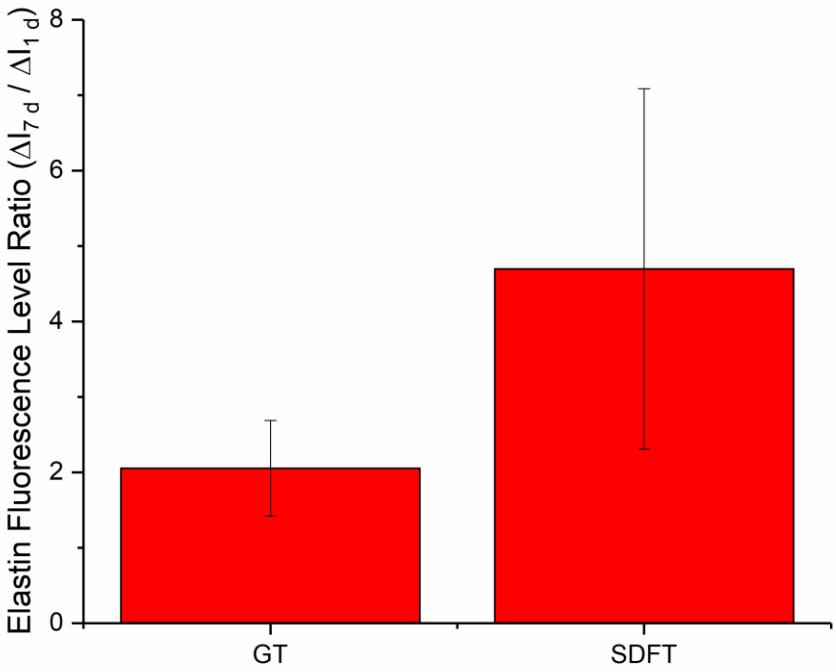

Figure 6.18. Changes in Elastin fluorescence levels due to the treatment of stress relaxation.

Elastin protein level ratios of 7-d stress relaxation over 1-d stress relaxation of young rabbit GTs and SDFTs calculated based on Eqn. 6.2 using fluorescence level changes normalized by the controls. Data are displayed as the mean ± SD (n=4). Significant differences were analysed by 2-sample t-test. No statistical difference was found between the two tendon groups.

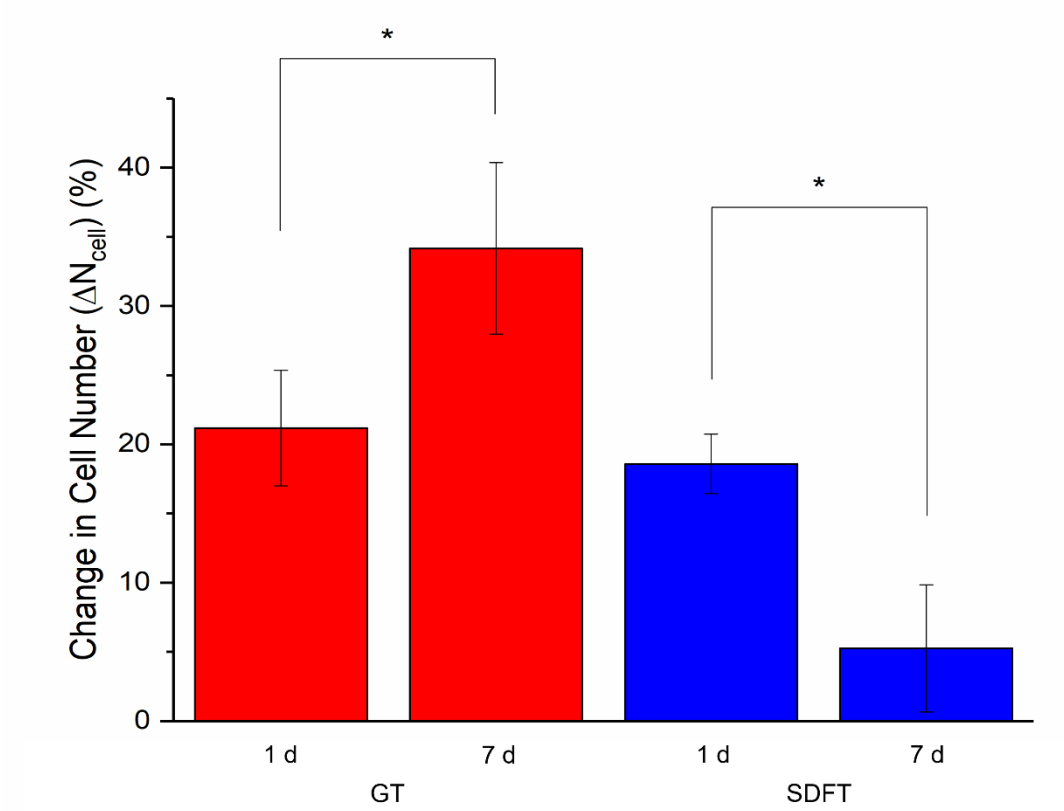

Figure 6.19. Quantification of cell number alterations due to stress relaxation. Changes in cell numbers in the rabbit GTs and SDFTs after 1 d and after 7 d compared to their corresponding controls. Data are derived based on Eqn. 6.4 and are displayed as the mean ± SD (n=4). Significant differences were analysed by 2-sample t-test. *P < 0.05.

6.3.2.4 Histological Analysis

Results of the control GTs and SDFTs stained with H&E are illustrated in the left column of Figure 6.20. The collagen matrix displaying the usual wavy crimp pattem was stained pink, and the cell nuclei were stained purplish blue. On the other hand, stress-relaxed GTs and SDFTs (mid and right column of Figure 6.20) showed apparent ECM alterations including (I) increased vascularity (marked with white arrows) and

(II) migration/infiltration of inflammatory cells (e.g., macrophages, heterophils, and lymphocytes which are marked with yellow arrows, blue arrows, and green arrows, respectively). The existence of inflammation was seen both in day 1 and day 7 for both tendon types. Quantification of vascularity changes (ΔV) is shown in Figure 6.21. Both tendon types display similar increase in vascularity level (ΔV≈80%) after 1 day of treatment. While ΔV on day 7 was higher than the day 1 in the GTs (+56.7%), no statistical difference was found between them. For the SDFTs, the ΔV was statistically lower on day 7 (-92.9%) compared to day 1.

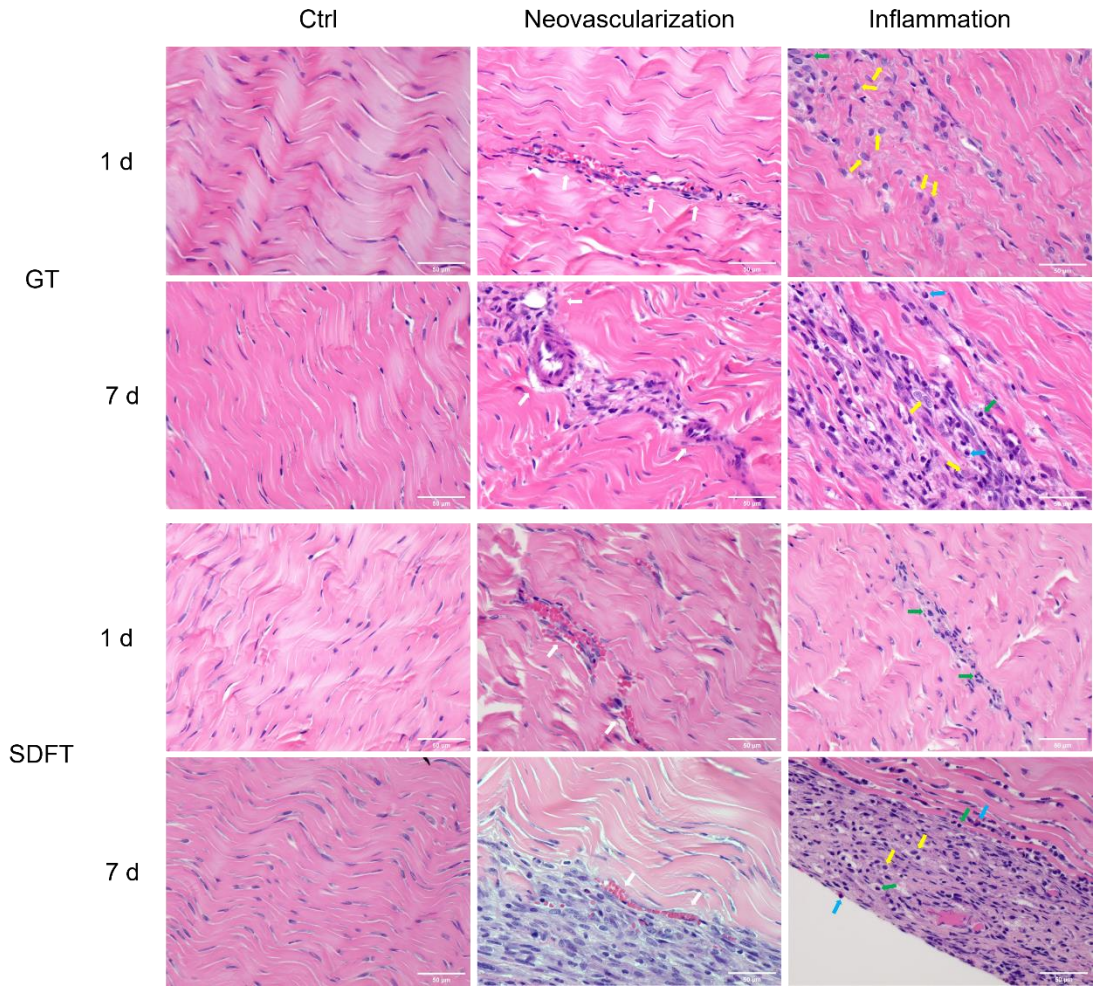

Figure 6.20. H&E-stained GT and SDFT.

Optical images of rabbit GTs and SDFTs treated with 1-d and 7-d stress relaxation from H&E staining. A control image of each group is displayed in the 1st column. The collagen matrix displaying the usual wavy crimp pattern was stained pink, and the cell nuclei were stained purplish blue. Representative regions of neovascularization (2nd column) and inflammation (3rd column) of the tendon FM are displayed for each experimental group. Neovascularization (marked with white arrows) and inflammatory cells including macrophages (marked with yellow arrows), heterophils (marked with blue arrows), and lymphocytes (marked with green arrows) could be observed. Scale bars are 50 μm.

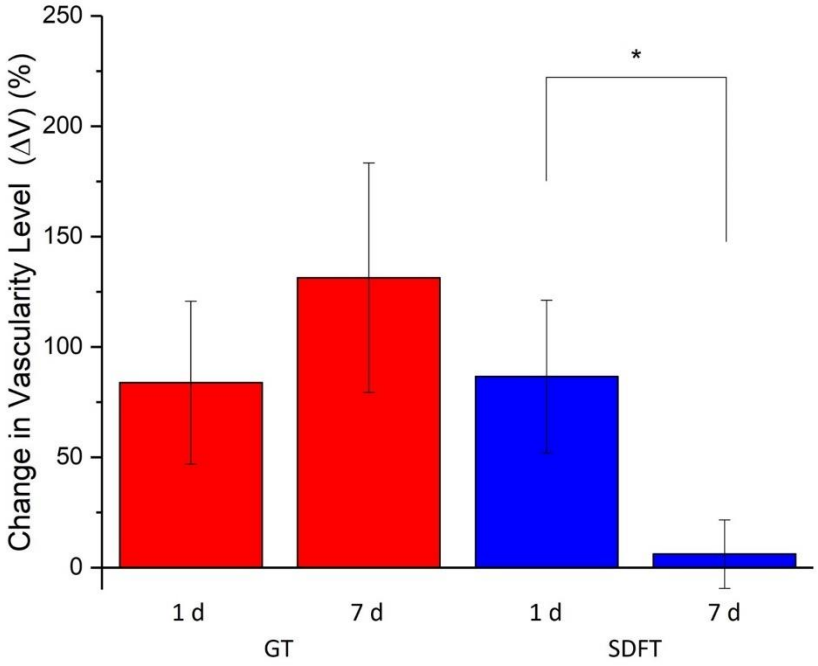

Figure 6.21. Quantification of vascularity alterations due to stress relaxation.
Changes in vascularity level of the rabbit GTs and SDFTs after 1 d and after 7 d compared to their corresponding controls were quantified based on Eqn. 6.3. Data are displayed as the mean ± SD (n=4). Significant differences were analysed by 2-sample t-test. *$P < 0.05$.

6.4 Discussion

In the first part of this chapter, a tendon scaffold created by removing the native cellular components was used to study the cellular response to a long-term stress relaxation. Various methods to remove native cellular components from the tissue have been studied in the field of biomaterials and tissue engineering (365–367). In tendon repair, the use of decellularized tendons as scaffolds to aid tissue regeneration has shown promising results due to their similarity to the native ECM (356,368,369).

Adopting this advantage to better mimic the *in vivo* condition under an *in vitro* setting, a decellularized tendon was used in this experiment to investigate the effect of stress relaxation on tenocytes. Although the DNA quantification showed that more than half of the DNA materials remained in the scaffold after the decellularization treatment, no intact tenocyte nucleus was observed in the ECM by fluorescence imaging and histology. The decellularization treatment should thus limit the interference of native cellular components with seeded tenocytes during culture and the analyses after culture.

After 3 weeks of culturing along with stress relaxation applied to the cells, tenocyte morphology has shifted to an elongated shape (Figure 6.9) and the expressions of elastin and collagen type I have increased. Zhu *et al.* (370) demonstrated in an *in vitro* experiment that an enforced elongated tenocyte morphology (using microgroove silicone membrane) could encourage passaged tenocytes to retain their phenotype and function by maintaining the expression of tenomodulin and collagen type I. As shown by several studies (371,372), tenocyte morphology is associated with tendon health and pathologies. Tenocytes with a more rounded, as opposed to the normal spindle-shaped morphology, were seen in a higher density in a tendon with tendinosis. In addition to cell shape, mechanical stimuli during culture have also shown to influence

tenocyte phenotype and health (373–376). However, existing research has not focused on the expression of elastin in tendons. One work conducted by Fleischhacker *et al.* in 2020 (377) examined multiple gene expressions of tenocytes in response to intervals of cyclic loading but could not evaluate ELN expression from the experiment. While other studies have looked at ELN expression (378,379), none of them was involved in mechanical straining. To compensate the tendon lengthening resulted from crimp angle reduction and elastin fragmentation (plastic deformation), the formation and deposition of new collagen and elastin proteins would be the key factor in the tendon healing and recovery period in the Ponseti method. Therefore, the upregulation of elastin and collagen type I in this experiment based on an *in vitro* mechanical model has provided promising results to support the treatment of Ponseti method.

To further investigate the biological response of a tendon to stress relaxation in an *in vivo* setting, a manipulation/tapping method was applied on 45-day-old NZW rabbits under two different time durations (1 d & 7 d). Cross-supporting results of crimp angle reduction ($\Delta\theta$) and elastin fragmentation ratio, which were also seen in chapter 4, were discovered from this experiment (Figure 6.15 & 6.17). In both GTs and SDFTs, a higher degree of $\Delta\theta$ corresponded to a higher degree of elastin fragmentation. The

reappearance of these two findings also recognized the viability of the *ex vivo* experimental method demonstrated in chapter 4. As mentioned earlier in chapter 4, crimp angle reduction and elastin fragmentation would disrupt the mechanical profile of a normal tendon and put the load-bearing tissue at a higher risk of injury, thus affecting the tendon health and function (258,259). Furthermore, the fragmented elastin peptides (or EDPs) are bioactive and could induce various biological pathways (326,327,333). Nevertheless, with the passage of time, the crimp angle has partially restored (Figure 6.15), and the level of elastin fragmentation has levelled down on day 7 (Figure 6.17), providing evidence of the healing and recovery of a young tendon from the damage inflicted by the Ponseti method. Since these microstructural damages are linked to the success of the Ponseti method, the tendon's capability of healing and recovering from the treatment is crucial. The upregulation of both elastin and collagen expressions discussed earlier also indicates the occurrence of healing as newly formed elastin and collagen would be required to restore crimp morphology while the tendon was being stretched. Additionally, for both tendon types, the increase of elastin fluorescence level of the 7 d group was 2-4 times higher than the 1 d group (Figure 6.18). These results suggest the formation of new elastin in the ECM and may further support the occurrence of healing and recovery. Although not all fragmentated elastin

proteins could be repaired to restore crimp morphology on day 7, new elastin was formed in the tendon ECM.

However, elastin exists not only in the matrix of a tendon fascicle (FM) but also in blood vessels as it provides the blood vessels important rheological properties, such as the post-systolic elastic recoil (380). Since elastin comprises up to 50% of the dry weight of blood vessels (87), the increase in elastin fluorescence level on day 7 might partially come from the newly formed blood vessels. This speculation is verified by the histological staining displayed in Figure 6.20. Image analysis for vascularity level (Figure 6.21) discovered an increase of vascularity within the tendon FM soon after 24 hours of stress relaxation. However, blood vessels are rarely seen within the FM in a healthy tendon as shown in the left column of Figure 6.20, as tendons are known to be relatively avascular. A main source of blood supply comes from the paratenon as illustrated in Figure 6.22. Blood vessels travel within the paratenon and penetrate the IFM, creating an anastomotic vascular network (381,382). In this study, the increased FM vascularity indicates an outcome of tendon adaptation to a long-term stress relaxation. The formation of new blood vessels was likely a result of increased need for nutrient supply. Within several hours after tapping, an impediment of blood supply

could be caused by the mechanical treatment. As the tensile strain was applied along the long axis of the tendon, a compressive strain perpendicular to the axis would be produced by the Poisson's effect. This compressive strain would decrease the inter-fascicle and the inter-fibre distance, generate internal pressure, cause fluid exudation, and hinder blood flow (383–386), thus inducing neovascularization. Another cause of increased vascularity was due to the increased cellular activities to remodel/repair the tendon ECM. Several studies (387–389) have observed increased vascularity at the injury site (e.g., tenotomy, division, suture) of tendons to aid healing and recovery from the damage. In this work, the recovery processes from the ECM micro-damages including crimp angle reduction (Figure 6.15) and elastin fragmentation (Figure 6.17) would require remodelling of fractured or dysfunctional elastin and collagen. These processes involve migration and proliferation of various cell types (increased cell numbers displayed in Figure 6.19), enzymatic degradation or digestion of dysfunctional ECM components, and synthesis of new units of these components. All of them consumes energy and nutrients (390), resulting in the formation of new blood vessels as a response/adaptation to the reparative processes. Lastly, the EDPs generated due to elastin fragmentation were also reported to promote angiogenesis (formation of new blood vessels) (323,328,333,391,392). On the other hand, some

studies argued that while forming new blood vessels to provide blood and nutrients appears to be aiding tendon healing and recovery, the incidence of neovascularization has been interpreted as a sign of both persisting hypoxia and failed tissue repair attempt (393), since hypervascularity and neovascularization along with the existence of inflammation in the tendon FM, which can be found in Figure 6.20, have been shown to be the features of chronic inflammation or tendinopathy (393–401). Unlike the vasculature developed during development and tissue growth, these newly formed blood vessels are believed to be hyperpermeable, i.e., they leak and do not have proper perfusion. As a result, these vessels fail to deliver oxygen and nutrients to tissue regions under hypoxia, creating a vicious cycle in which hypoxia continues to exist in the regions of neovascularization (393,402). Nevertheless, the development of chronic tendinopathy in this experiment was unlikely. First, a time length of 7 days is not sufficient to develop chronic tendinopathy (403). Second, tissue repair was present during the mechanical treatment as demonstrated from the restoration of crimp angle (Figure 6.15) and ameliorated elastin fragmentation level (Figure 6.17). Third, chronic tendinopathy has a low incidence rate in young tendons (404,405).

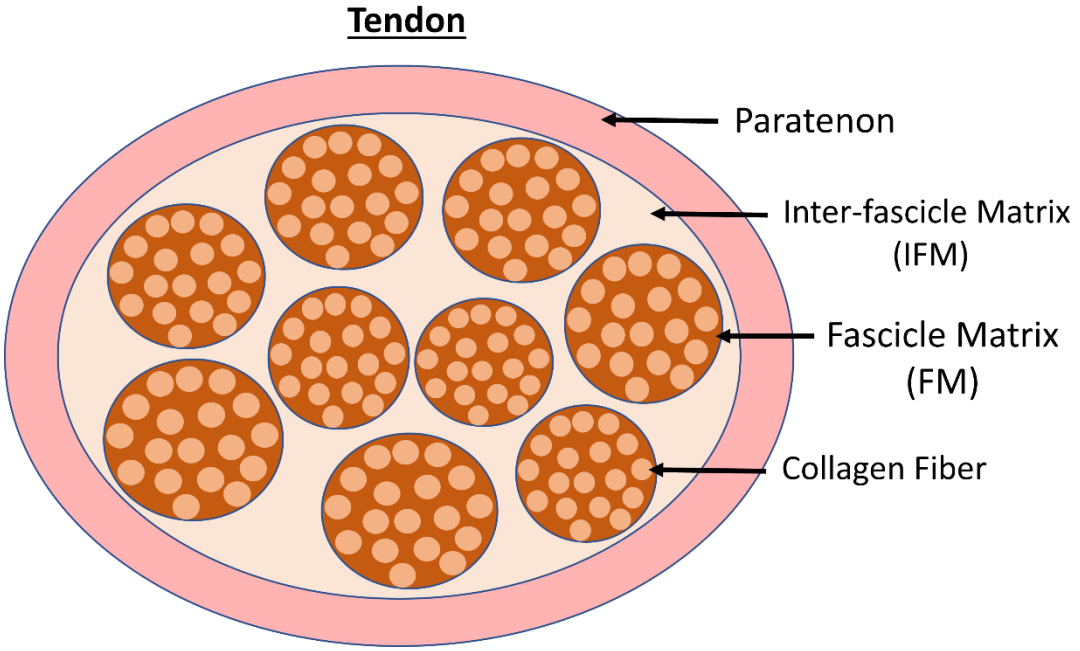

Figure 6.22. Illustrative image showing the cross-section microstructure/components including the collagen fibre, FM, IFM, and paratenon.

Unfortunately, the increase of vascularity may still produce several issues for a tendon tissue. The immediate problem created is the loss of mechanical strength and function due to the alteration of the tendon matrix. Based on current studies, compared to the elastic moduli of fascicles of several tendons ranging from 216-800 MPa (266,406–408), the moduli of various blood vessels ranging from 2.25-23.7 MPa (409–412) are much lower. As the majority of the tendon's dry weight is composed of collagen fibres (66), the partial replacement of these fibres with a relatively softer material in a FM would certainly weaken the tendon's mechanical strength. Furthermore, the substitution of blood vessels for collagen fibres in the FM could result in matrix

inhomogeneity which could cause abnormal stress/strain distribution during loading. Wiesinger *et al.* (413) has discovered a reduced elastic modulus in human chronic tendinopathic patellar tendons which exhibited neovascularization in the matrix. A work done by Wunderli *et al.* (414) in 2020, focusing on mechanical loading response in hypervascular tendon, reported a rapid cell-mediated tissue breakdown upon mechanical unloading, in contrast to the unloaded physiologically normal hypovascular tendon. Under high temperature and oxygen level (modelling hypervascularity), a higher level of reactive oxygen species (ROS) was produced, which altered the regulation of several ECM proteases, causing proteolytic ECM degradation and thus the loss of mechanical strength. Furthermore, the presence of blood vessels in the FM has been reported to be the source of pain in patellar tendons of jumping athletes (415). Therefore, whether the increased vascularity in this study persist or not over time after the treatment requires further investigation. Moreover, despite the features of healing and recovery mentioned above, inflammation in the tendon ECM (Figure 6.20) also persisted even after 7 days, suggesting the duration of 1 week may not be enough to fully recover a tendon from a Ponseti-modelled stress relaxation. If complications are caused due to this increased vascularity, additional treatment for anti-inflammation or anti-angiogenesis may be required.

Overall, the stress relaxation generated by the Ponseti method was demonstrated to be effective. Although this mechanical treatment resulted in structural, compositional, and cellular alterations including crimp angle reduction, elastin fragmentation, increased vascularity, and inflammation, signs of healing and recovery (i.e., the restoration of crimp, alleviated elastin fragmentation, and increased elastin level) after 7 days of treatment were observed. Still, the persisted inflammation and increased vascularity have brought new concerns to this treatment. While concerning, these complications point out a possible reason explaining why the Ponseti method was aimed to correct clubfoot of young children below 9 years of age (416–418): the healing and remodelling capabilities of the ECM are better in younger individuals, which is the reason why young rabbits of 45 days of age were chosen in this study to model the Ponseti method. Whether the ECM alterations observed can be recovered over time will require further investigation.

6.5 Summary

In this chapter, the cellular response to a stress relaxation was investigated using an *in vitro* model. Human tenocytes derived from hamstring tendons were seeded and

cultured on decellularized bovine DDFT sections. Stress relaxation was applied to these sections through a miniature motorized linear stage in a custom-made culture system. Results from cellular adaptation and gene expression showed elongated tenocyte morphology after loading and upregulation of COL1A1 and ELN, supporting the need for new collagen and elastin formation in the ECM after the material-based microstructural alterations (tissue lengthening, crimp angle reduction & elastin fragmentation) observed in chapter 4 inflicted by the stress relaxation.

An animal model using 45-day-old NZW rabbits to study the effect of stress relaxation on tendon ECM was performed. Through manipulation and taping, a rabbit CCT (GT & SDFT) was strained to an engineering strain of approximated 8% for 1 day or 7 days. ECM alterations including crimp angle reduction, elastin fragmentation, increased vascularity, and inflammation were discovered. For both GT and SDFT, lower levels of crimp angle reduction and elastin fragmentation along with higher elastin fluorescence level were found in day 7 compared to day 1, indicating restoration of crimp morphology, remodelling of elastin fragments and new elastin formation over time in the tendon matrix. However, the increased vascularity and persisted inflammation in the FM also created concerns such as matrix inhomogeneity, loss of

mechanical integrity, risk of proteolytic ECM degradation, source of pain, and potential risk of chronic tendinopathy. Hence, further investigations and experiments are needed to examine whether these ECM complications persist over time. Furthermore, additional therapies for stabilising vascularity and reducing inflammation should be considered during and after the treatment of Ponseti method to ensure the health, integrity, and function of the treated tendon tissue.

Chapter 7 Conclusion and Future Work

7.1 Conclusion

The aim of this work is to (I) reveal the mechanical effect of a long-term stress relaxation on a tendon, (II) discover the changes of tendon microstructures due to this mechanical treatment, (III) probe the mechanism behind the Ponseti method, (IV) investigate the role of elastin in tendon stress relaxation, and (V) study the biological response to the Ponseti treatment.

A simple but effective tensile setup was first developed to solve the common issues including slippage, failure at clamp region, and high strain concentration due to grip compression in tendon tensile testing. The setup uses selective air-drying and polymeric teeth for gripping, and its efficacy was verified by matching engineering strains derived by grip displacement and surface marker displacement. Reduced strain rate-dependency of modulus was found in tendons strained at rates below 1%/s as the rate decreases; on the other hand, no rate-dependency was observed on strain at UTS. This result suggests the probability of minimizing resistance from the clubfoot by lowering the rate of the Ponseti manipulation procedure.

Tendons treated with long-term stress relaxations (modelling a Ponseti cast) displayed treatment time-dependent (0 h, 2 h, 24 h & 48 h) and cross-matching alterations including (I) irreversible tendon lengthening, (II) crimp angle reduction and (III) elastin fragmentation. The maximum lengthening value was achieved within 2-24 hours of the stress relaxation which supports the efficacy of the accelerated protocols with a shorter time interval between casts proposed by existing studies (38–40). The association between the alterations mentioned above indicates a mechanism of the Ponseti method based on elastin. As the elastin is known to be responsible for maintaining the crimp morphology, elastin fragmentation would result in irreversible reduction of crimp angle under tension. A reduced crimp angle would also produce a mechanical profile with shorter toe region which was seen in this study. Hence, the tendon lengthening spotted was simply a result of reduced elastic recoil generated by elastin fragmentation. This angle reduction in crimp caused by elastin fragmentation was further proved by elastin digestion via elastase treatment of tendon where the elastase-treated tendons also displayed irreversible tissue lengthening and crimp angle reduction. A strain-mediated hydrolytic degradation of elastin, which exposes the hydrophobic regions of elastin to water molecules, was proposed as the cause of elastin fragmentation from the stress relaxation treatment since the fragmentation was time-

dependent, and the elastin is capable of withstanding strains much larger than 8%. Particularly, the degradative reaction is likely to occur at the disulphide bond of the elastin molecule as various studies have found a load-mediated S_N2 reaction on the disulphide bond where a tensile load of 2nN was enough to diminish approximately 60% of the activation free energy of the reaction without the addition of neither alkaline nor heat. The results of stress relaxation on elastase-treated tendons discovered (I) decreased overall stress profile and (II) decreased stress relaxation, and (III) decreased relaxation rate derived from curve-fitting using Maxwell and power law equations. Based on these findings, elastin in the tendon ECM contributes positively to stress relaxation potentially via hydrolytic degradation, and this activity may become more dominant compared to other relaxation events (e.g., inter-fibre sliding, fibre reorganization and water diffusion from the PG/GAG matrix) over time.

Regarding the biological response to a long-term stress relaxation, (I) restoration of the reduced crimp angle, (II) alleviated elastin fragmentation, (III) increased elastin level in the ECM, (4) increased vascularity, and (5) persisted inflammation were found in 45-day-old rabbit CCTs stress-relaxed for 7 days compared to those for 1 day. The changes in crimp and elastin suggested healing and recovery occurring in the tendon

ECM. Additionally, cellular response derived from the *in vitro* experiment discovered increased gene expressions of COL1A1 and ELN, supporting the incidence of recovery. The increased vascularity and persisted inflammation were both important biological adaptation in response to the mechanical treatment. While the increased vascularity along with inflammation were features of chronic tendinopathy in tendons, the incidence of tendinopathy was unlikely to develop on young tendons within 7 days. These biological adaptations were more likely to be the results from the increased need for nutrients and blood supply, and increased cellular activities for ECM synthesis, deposition, and remodelling.

However, although the signs of recovery were observed, whether these ECM alterations (crimp angle reduction, elastin fragmentation, increased vascularity, and persisted inflammation) will be fully-recovered in time remains unclear. The reduced crimp angle would change the mechanical profile and may predispose the tendon to overstretching (258,259). Moreover, the bioactive EDPs from the fragmented elastin may cause undesired biological events such as promoting the progression of chronic inflammation (326,327). Lastly, the increased vascularity and inflammation could

result in complications including matrix inhomogeneity, loss of mechanical integrity, and source of pain (415).

In summary, this study shows that a long-term stress relaxation modelling the Ponseti method 'time-dependently' lengthens the tendon by elastin fragmentation possibly due to a strain-mediated hydrolytic degradation. Elastin was found to maintain the collagen crimp morphology, contribute to the 'toe' region in the mechanical profile, and positively contribute to tendon stress relaxation and relaxation rate. Although signs of healing and recovery were present after 7 days of stress relaxation, the influence of several remaining ECM alterations requires further observation and evaluation.

7.2 Future Work

This thesis is the first work to (I) examine the ECM alterations in response to the Ponseti method from the microstructural and histological perspectives, (II) investigate the effect of casting time and discover a time-dependency from the treatment, and (III) probe the role of elastin in a stress relaxation of a tendon; yet additional experiments may be added in the future.

First, the stress relaxation setup, which utilizes selective air-drying, successfully removed slippage and enabled long-term testing, but the transitional interface between the hydrated and air-dried regions requires further investigations. Instead of a sharp interface, a transitional 'gap' with a width is more likely to exist between the two regions. Moreover, this gap would display a gradient of hydration level, and if a significant width of gap exists, the mechanical properties derived by testing would be inaccurate. Hence, an experiment may be conducted to discover this gap width. For instance, indentation experiment can be performed along the long axis of the selective air-dried tendon, and the stiffness profile along the long axis can be plotted to see if a transitional gap exists.

Second, additional tests under relaxation durations between 0 h and 24 h can be conducted (e.g., 10 min, 20 min, 30 min, and 1 h) with the focus on tendon lengthening, crimp angle reduction, and elastin fragmentation. With enough duration time points, plots of the above-mentioned alterations against relaxation duration can be plotted, and potentially the relationships between relaxation duration and the three alterations can be derived. The results of elastin fragmentation versus time may not only help determine the optimal casting duration for the accelerated protocols of Ponseti method,

but also help prove the proposed strain-mediated hydrolysis theory for elastin fragmentation.

Third, experiments need to be conducted to prove the validity of the strain-mediated hydrolysis theory. If the cause of fragmentation is not mechanical fracture but hydrolytic degradation, adjusting several conditions such as temperature, pH, and alcohol addition of the long-term stress relaxation treatment should change the rate of the elastin fragmentation. Furthermore, examination of the speculation of disulphide bond reduction (from -S-S- to 2 -SH) in elastin could be conducted using infrared (IR) spectroscopy (stretching vibrations of S-S bonds: 500–550 cm^{-1}) (419).

Fourth, extended work should be conducted following the *in vivo* experiments. As discussed earlier in chapter 6, whether the ECM alterations including crimp angle reduction, elastin fragmentation, increased vascularity, and inflammation persist over time is an important research question as they would affect the function, health, and mechanical properties of a tendon. An additional 'recovery' period without any tapping or tension on the rabbit foot could be added as an experimental group, and the levels of these ECM alterations could then be compared. IHC staining or western blot

experiments using antibodies that target endothelial cells (vascular cells) or inflammatory cells such as CD31 and CD11b can be applied to quantify the levels of vascularization and inflammation. Furthermore, the effect of anti-inflammatory treatment or anti-angiogenic treatment in addition to the mechanical stretch can be explored as well.

Lastly, future work needs to provide further scientific evidence for supporting the accelerated protocol of the Ponseti method. In this thesis, the maximum level of material deformation/lengthening of a tendon was achieved within 24 hours which is even shorter than the casting intervals of the accelerated protocols proposed by existing studies (38–40). However, the *in vivo* results in chapter 6 only discovered signs of recovery when comparing rabbits treated with 7-day duration of stress relaxation with those treated with 1-day duration. Additional studies need to look at time durations between 7 days and 1 day (e.g., 3 days of stress relaxation) to compare the levels of recovery within the tendon ECM. The same studies and experiments are also worth conducting on rabbits of younger and older ages to examine the difference of younger and older tendons responding to stress relaxation. Because there is a consensus that treatment for club foot should start not later than within the first month of life (12,13),

how an older tendon adapt to the treatment is an important research question. Furthermore, in addition to tendons and ligaments, other tissues such as nerves and blood vessels are being strained in the treatment; hence, future studies focused on these tissues responding to stretching are also important to improve or accelerate the Ponseti method. A possible protocol to hyper-accelerate the Ponseti casting intervals may be achieved if the tendons and ligaments of a clubfoot can avoid consecutive stretching throughout the treatment. For instance, the first manipulation aims to correct cavus which strains the tendons and ligaments at the bottom of the foot. The second manipulation will concentrate on correcting adductus which in theory should only strain the medial side of the foot, giving the already strained tendons and ligaments at the bottom of the foot time to recover without additional straining. Hence, it is likely that the interval between the first and second manipulations can be as short as 24 hours. Clinical studies may attempt to discover the strain-heavy tissues in each manipulation and casting, and reset the sequence of manipulation and casting to avoid consecutive tissue stretching to accelerate the treatment. A non-invasive method to detect elastin fragmentation due to the Ponseti casting can also be done by measuring the desmosine level in urine, as desmosine is a stable breakdown product of elastin that can be reliably measured in urine samples (420,421).

Bibliography

1. Liu Y, Zhao D, Zhao L, Li H, Yang X. Congenital clubfoot: early recognition and conservative management for preventing late disabilities. Indian J Pediatr. 2016 Nov;83(11):1266–74.
2. Gray K, Pacey V, Gibbons P, Little D, Frost C, Burns J. Interventions for congenital talipes equinovarus (clubfoot). Cochrane Database Syst Rev. 2012 Apr;(4):CD008602.
3. Cooke SJ, Balain B, Kerin CC, Kiely NT. Clubfoot. Curr Orthop. 2008 Apr 1;22(2):139–49.
4. Garg N. Update on club foot. Paediatr Child Health. 2016;26(6):257–60.
5. Atar D, Lehman WB, Grant AD. Complications in clubfoot surgery. Orthop Rev. 1991 Mar;20(3):233–9.
6. Dobbs MB, Gurnett CA. Update on clubfoot: etiology and treatment. Clin Orthop Relat Res. 2009 May;467(5):1146–53.
7. Dobbs MB, Nunley R, Schoenecker PL. Long-term follow-up of patients with clubfeet treated with extensive soft-tissue release. J Bone Joint Surg Am. 2006 May;88(5):986–96.
8. Faldini C, Traina F, di Martino A, Nanni M, Acri F. Can selective soft tissue release and cuboid osteotomy correct neglected clubfoot? Clin Orthop Relat Res. 2013 Aug;471(8):2658–65.
9. Kocaoğlu M, Eralp L, Atalar AC, Bilen FE. Correction of complex foot deformities using the Ilizarov external fixator. J Foot Ankle Surg. 2002;41(1):30–9.
10. Weseley MS, Barenfeld PA, Barrett N. Complications of the treatment of clubfoot. Clin Orthop Relat Res. 1972;84:93–6.
11. Ponseti I v, Smoley EN. The classic: congenital club foot: the results of treatment. 1963. Clin Orthop Relat Res. 2009 May;467(5):1133–45.
12. Radler C. The Ponseti method for the treatment of congenital club foot: review of the current literature and treatment recommendations. Int Orthop. 2013 Sep;37(9):1747–53.
13. Jowett CR, Morcuende JA, Ramachandran M. Management of congenital talipes equinovarus using the Ponseti method: a systematic review. J Bone Joint Surg Br. 2011 Sep;93(9):1160–4.
14. Zionts LE, Zhao G, Hitchcock K, Maewal J, Ebramzadeh E. Has the rate of extensive surgery to treat idiopathic clubfoot declined in the United States? JBJS. 2010;92(4):882–9.

15. Howard CB, Benson MKD. Clubfoot: its pathological anatomy. Journal of Pediatric Orthopaedics. 1993;13(5):654–9.
16. Fried A. Recurrent congenital clubfoot; the role of the M. tibialis posterior in etiology and treatment. J Bone Joint Surg Am. 1959 Mar;41-A(2):243–52.
17. Ippolito E, Ponseti I v. Congenital club foot in the human fetus. A histological study. J Bone Joint Surg Am. 1980 Jan;62(1):8–22.
18. Masala S, Manenti G, Antonicoli M, Morosetti D, Claroni G, Simonetti G. Real time evaluation of monolateral clubfoot with sonoelastography. Preliminary results. Muscles Ligaments Tendons J. 2012 Jan;2(1):49–52.
19. Arkin C, Ihnow S, Dias L, Swaroop VT. Midterm results of the Ponseti method for treatment of clubfoot in patients with Spina Bifida. J Pediatr Orthop. 2018;38(10):e588–92.
20. Gelfer Y, Wientroub S, Hughes K, Fontalis A, Eastwood DM. Congenital talipes equinovarus: a systematic review of relapse as a primary outcome of the Ponseti method. Bone Joint J. 2019 Jun;101-B(6):639–45.
21. Chen C, Wang TM, Wu KW, Huang SC, Kuo KN. Comparison of two methods for idiopathic clubfoot treatment: A case-controlled study in Taiwan. J Formos Med Assoc. 2019 Feb;118(2):636–40.
22. Jeans KA, Karol LA, Erdman AL, Stevens WRJ. Functional outcomes following treatment for clubfoot: ten-year follow-up. J Bone Joint Surg Am. 2018 Dec;100(23):2015–23.
23. Smythe T, Chandramohan D, Bruce J, Kuper H, Lavy C, Foster A. Results of clubfoot treatment after manipulation and casting using the Ponseti method: experience in Harare, Zimbabwe. Trop Med Int Health. 2016 Oct;21(10):1311–8.
24. Shabtai L, Hemo Y, Yavor A, Gigi R, Wientroub S, Segev E. Radiographic indicators of surgery and functional outcome in Ponseti-treated clubfeet. Foot Ankle Int. 2016 May;37(5):542–7.
25. Radler C, Manner HM, Suda R, Burghardt R, Herzenberg JE, Ganger R, et al. Radiographic evaluation of idiopathic clubfeet undergoing Ponseti treatment. J Bone Joint Surg Am. 2007 Jun;89(6):1177–83.
26. O'Halloran CP, Halanski MA, Nemeth BA, Zimmermann CC, Noonan KJ. Can radiographs predict outcome in patients with idiopathic clubfeet treated with the Ponseti method? J Pediatr Orthop. 2015;35(7):734–8.
27. Baghdadi T, Bagheri N, Najafi A, Mansouri P, Farzan M. Ponseti casting method in idiopathic congenital clubfoot and its correlation with radiographic features abstract. Arch Bone Jt Surg. 2017 May;5(3):168–73.

28. Mishima K, Kitoh H, Matsushita M, Sugiura H, Hasegawa S, Kitamura A, et al. Early radiographic risk factors for rigid relapse in idiopathic clubfoot treated with the Ponseti method. Foot Ankle Surg. 2018 Dec;24(6):509–13.
29. Chandirasegaran S, Gunalan R, Aik S, Kaur S. A comparison study on hindfoot correction, Achilles tendon length and thickness between clubfoot patients treated with percutaneous Achilles tendon tenotomy versus casting alone using Ponseti method. J Orthop Surg (Hong Kong). 2019;27(2):2309499019839126.
30. Jochymek J, Turek J. The ultrasonography evaluation of talar dysplasia as a potential prognostic factor for predicting the course and outcomes of clubfoot deformity treatment using Ponseti technique. Acta Orthop Traumatol Turc. 2018 Mar;52(2):87–91.
31. Bedford KJA, Chidothi P, Sakala H, Cashman J, Lavy C. Clubfoot in Malawi: treatment-seeking behaviour. Trop Doct. 2011 Oct;41(4):211–4.
32. Kazibwe H, Struthers P. Barriers experienced by parents of children with clubfoot deformity attending specialised clinics in Uganda. Trop Doct. 2009 Jan;39(1):15–8.
33. Kingau NW, Rhoda A, Mlenzana N. Barriers experienced by service providers and caregivers in clubfoot management in Kenya. Trop Doct. 2015 Apr;45(2):84–90.
34. Harmer L, Rhatigan J. Clubfoot care in low-income and middle-income countries: from clinical innovation to a public health program. World J Surg. 2014 Apr;38(4):839–48.
35. Dibello D, Colin G, Galimberti AMC, di Carlo V. Ten year challenge with Ponseti method for clubfoot: our experience. Acta Biomed. 2019 Dec;90(12-S):127–30.
36. Ko KR, Shim JS, Kim JH, Cha YT. Difficulties during Ponseti casting for the treatment of idiopathic clubfoot. J Foot Ankle Surg. 2020;59(1):100–4.
37. Evans A, Chowdhury M, Karimi L. Factors affecting parents to “drop-out” from Ponseti method and children’s clubfoot relapse. Orthopedic Research Online Journal. 2020;6(3):601–9.
38. Ahmad AA, Aker L. Accelerated Ponseti method: First experiences in a more convenient technique for patients with severe idiopathic club feet. Foot Ankle Surg. 2020 Apr;26(3):254–7.
39. Barik S, Nazeer M, Mani BT. Accelerated Ponseti technique: efficacy in the management of CTEV. Eur J Orthop Surg Traumatol. 2019 May;29(4):919–24.

40. Islam MS, Masood QM, Bashir A, Shah FY, Halwai MA. Results of a standard versus an accelerated Ponseti protocol for clubfoot: a prospective randomized study. Clin Orthop Surg. 2020 Mar;12(1):100–6.
41. Walker LB, Harris EH, Benedict J v. Stress-strain relationship in human cadaveric plantaris tendon: a preliminary study. Med Electron Biol Eng. 1964 Mar;2:31–8.
42. Maganaris CN, Paul JP. In vivo human tendon mechanical properties. J Physiol. 1999 Nov 15;521 Pt 1(Pt 1):307–13.
43. Liao X, Kemp S, Corner G, Eisma R, Huang Z. Elastic properties of Thiel-embalmed human ankle tendon and ligament. Clin Anat. 2015 Oct;28(7):917–24.
44. Kongsgaard M, Nielsen CH, Hegnsvad S, Aagaard P, Magnusson SP. Mechanical properties of the human Achilles tendon, in vivo. Clin Biomech (Bristol, Avon). 2011 Aug;26(7):772–7.
45. Ji Y, Tang X, Li Y, Xu W, Qiu W. Analysis of 3-dimensional finite element after reconstruction of impaired ankle deltoid ligament. Exp Ther Med. 2016 Dec;12(6):3913–6.
46. Siegler S, Block J, Schneck CD. The mechanical characteristics of the collateral ligaments of the human ankle joint. Foot Ankle. 1988 Apr;8(5):234–42.
47. An Y, Ji C, Li Y, Wang J, Zhang X, Huang Y. In vivo measurements of human neck skin elasticity using MRI and finite element modeling. Med Phys. 2017 Apr;44(4):1402–7.
48. Sutradhar A, Miller MJ. In vivo measurement of breast skin elasticity and breast skin thickness. Skin Res Technol. 2013 Feb;19(1):e191-9.
49. Khatyr F, Imberdis C, Vescovo P, Varchon D, Lagarde JM. Model of the viscoelastic behaviour of skin in vivo and study of anisotropy. Skin Res Technol. 2004 May;10(2):96–103.
50. Pailler-Mattei C, Bec S, Zahouani H. In vivo measurements of the elastic mechanical properties of human skin by indentation tests. Med Eng Phys. 2008;30(5):599–606.
51. Zahouani H, Pailler-Mattei C, Sohm B, Vargiolu R, Cenizo V, Debret R. Characterization of the mechanical properties of a dermal equivalent compared with human skin in vivo by indentation and static friction tests. Skin Res Technol. 2009 Feb;15(1):68–76.
52. Chao CYL, Zheng YP, Cheing GLY. Epidermal thickness and biomechanical properties of plantar tissues in diabetic foot. Ultrasound Med Biol. 2011;37(7):1029–38.

53. Li HY, Hua YH. Achilles Tendinopathy: Current concepts about the basic science and clinical treatments. Biomed Res Int. 2016;2016:6492597.
54. Kjaer M. Role of extracellular matrix in adaptation of tendon and skeletal muscle to mechanical loading. Physiol Rev. 2004 Apr;84(2):649–98.
55. Thorpe CT, Screen HRC. Tendon structure and composition. Adv Exp Med Biol. 2016;920:3–10.
56. Tang H, Buehler MJ, Moran B. A constitutive model of soft tissue: from nanoscale collagen to tssue continuum. Ann Biomed Eng. 2009;37(6):1117–30.
57. Böl M, Ehret AE, Leichsenring K, Ernst M. Tissue-scale anisotropy and compressibility of tendon in semi-confined compression tests. J Biomech. 2015;48(6):1092–8.
58. Ciarletta P, Micera S, Accoto D, Dario P. A novel microstructural approach in tendon viscoelastic modelling at the fibrillar level. J Biomech. 2006;39(11):2034–42.
59. Natali AN, Pavan PG, Carniel EL, Lucisano ME, Taglialavoro G. Anisotropic elasto-damage constitutive model for the biomechanical analysis of tendons. Med Eng Phys. 2005;27(3):209–14.
60. Wagner M, Kääb MJ, Schallock J, Haas NP, Weiler A. Hamstring tendon versus patellar tendon anterior cruciate ligament reconstruction using biodegradable interference fit fixation: a prospective matched-group analysis. Am J Sports Med. 2005 Sep;33(9):1327–36.
61. Xie X, Liu X, Chen Z, Yu Y, Peng S, Li Q. A meta-analysis of bone-patellar tendon-bone autograft versus four-strand hamstring tendon autograft for anterior cruciate ligament reconstruction. Knee. 2015 Mar;22(2):100–10.
62. Amiel D, Frank C, Harwood F, Fronek J, Akeson W. Tendons and ligaments: a morphological and biochemical comparison. J Orthop Res. 1984;1(3):257–65.
63. Mienaltowski MJ, Birk DE. Structure, physiology, and biochemistry of collagens. Adv Exp Med Biol. 2014;802:5–29.
64. Netti P, D'amore A, Ronca D, Ambrosio L, Nicolais L. Structure-mechanical properties relationship of natural tendons and ligaments. J Mater Sci Mater Med. 1996;7(9):525–30.
65. Rumian AP, Wallace AL, Birch HL. Tendons and ligaments are anatomically distinct but overlap in molecular and morphological features--a comparative study in an ovine model. J Orthop Res. 2007 Apr;25(4):458–64.
66. Lin TW, Cardenas L, Soslowsky LJ. Biomechanics of tendon injury and repair. J Biomech. 2004;37(6):865–77.

67. Taye N, Karoulias SZ, Hubmacher D. The “other” 15-40%: The role of non-collagenous extracellular matrix proteins and minor collagens in tendon. J Orthop Res. 2020 Jan;38(1):23–35.
68. Fang M, Holl MMB. Variation in type I collagen fibril nanomorphology: the significance and origin. Bonekey Rep. 2013 Aug;2:394.
69. Gautieri A, Vesentini S, Redaelli A, Buehler MJ. Hierarchical structure and nanomechanics of collagen microfibrils from the atomistic scale up. Nano Lett. 2011 Feb;11(2):757–66.
70. Kastelic J, Galeski A, Baer E. The multicomposite structure of tendon. Connect Tissue Res. 1978;6(1):11–23.
71. Herchenhan A, Uhlenbrock F, Eliasson P, Weis M, Eyre D, Kadler KE, et al. Lysyl oxidase activity is required for ordered collagen fibrillogenesis by tendon cells. J Biol Chem. 2015 Jun;290(26):16440–50.
72. Kadler KE, Holmes DF, Trotter JA, Chapman JA. Collagen fibril formation. Biochem J. 1996 May;316 (Pt 1(Pt 1):1–11.
73. Buehler MJ. Nature designs tough collagen: explaining the nanostructure of collagen fibrils. Proc Natl Acad Sci U S A. 2006 Aug;103(33):12285–90.
74. Costa-Almeida R, Gonçalves AI, Gershovich P, Rodrigues MT, Reis RL, Gomes ME. Tendon Stem Cell Niche. In: Turksen K, editor. Tissue-specific stem cell niche. Cham: Springer International Publishing; 2015. p. 221–44.
75. Uzel SGM, Buehler MJ. Nanomechanical sequencing of collagen: tropocollagen features heterogeneous elastic properties at the nanoscale. Integr Biol. 2009;1(7):452–9.
76. Screen HRC, Berk DE, Kadler KE, Ramirez F, Young MF. Tendon functional extracellular matrix. J Orthop Res. 2015 Jun;33(6):793–9.
77. Robi K, Jakob N, Matevz K, Matjaz V. The physiology of sports injuries and repair processes. In: Jakob N, editor. Current Issues in Sports and Exercise Medicine. Rijeka: IntechOpen; 2013. p. 43–86.
78. Kannus P. Structure of the tendon connective tissue. Scand J Med Sci Sports. 2000 Dec;10(6):312–20.
79. Thorpe CT, Birch HL, Clegg PD, Screen HRC. The role of the non-collagenous matrix in tendon function. Int J Exp Pathol. 2013 Aug;94(4):248–59.
80. Bosch U, Gässler N, Decker B. Alterations of glycosaminoglycans during patellar tendon autograft healing after posterior cruciate ligament replacement. A biochemical study in a sheep model. Am J Sports Med. 1998;26(1):103–8.

81. Ryan CNM, Sorushanova A, Lomas AJ, Mullen AM, Pandit A, Zeugolis DI. Glycosaminoglycans in tendon physiology, pathophysiology, and therapy. Bioconjug Chem. 2015 Jul 15;26(7):1237–51.
82. Vogel KG, Thonar EJ. Keratan sulfate is a component of proteoglycans in the compressed region of adult bovine flexor tendon. J Orthop Res. 1988;6(3):434–42.
83. Yoon JH, Halper J. Tendon proteoglycans: biochemistry and function. J Musculoskelet Neuronal Interact. 2005 Mar;5(1):22–34.
84. Benjamin M, Ralphs JR. Tendons and ligaments--an overview. Histol Histopathol. 1997;12(4):1135—1144.
85. Montes GS. Structural biology of the fibres of the collagenous and elastic systems. Cell Biol Int. 1996 Jan;20(1):15–27.
86. Kristensen JH, Thorlacius-Ussing J, Rønnow SR, Karsdal MA. Chapter 30 - Elastin. In: Karsdal MA, editor. Biochemistry of Collagens, Laminins and Elastin (Second Edition). Second Edi. Academic Press; 2019. p. 265–73.
87. Mithieux SM, Weiss AS. Elastin. in: fibrous proteins: coiled-coils, collagen and elastomers. Academic Press; 2005. p. 437–61. (Advances in Protein Chemistry; vol. 70).
88. Gosline J, Lillie M, Carrington E, Guerette P, Ortlepp C, Savage K. Elastic proteins: biological roles and mechanical properties. Philos Trans R Soc Lond B Biol Sci. 2002 Feb;357(1418):121–32.
89. Kielty CM, Sherratt MJ, Shuttleworth CA. Elastic fibres. J Cell Sci. 2002 Jul;115(Pt 14):2817–28.
90. Hinek A. The 67 kDa spliced variant of beta-galactosidase serves as a reusable protective chaperone for tropoelastin. Ciba Found Symp. 1995;192:185–6.
91. Uitto J, Christiano AM, Kähäri VM, Bashir MM, Rosenbloom J. Molecular biology and pathology of human elastin. Biochem Soc Trans. 1991 Nov;19(4):824–9.
92. Yeo GC, Keeley FW, Weiss AS. Coacervation of tropoelastin. Adv Colloid Interface Sci. 2011 Sep;167(1–2):94–103.
93. Fukuda Y, Nakazawa N, Yamanaka N. Interactions of elastin and microfibrils in elastogenesis of human pulmonary fibroblasts in culture. Connect Tissue Res. 1993;29(4):301–10.
94. Kozel BA, Rongish BJ, Czirok A, Zach J, Little CD, Davis EC, et al. Elastic fiber formation: a dynamic view of extracellular matrix assembly using timer reporters. J Cell Physiol. 2006 Apr;207(1):87–96.

95. Sato F, Wachi H, Starcher BC, Murata H, Amano S, Tajima S, et al. The characteristics of elastic fiber assembled with recombinant tropoelastin isoform. Clin Biochem. 2006 Jul;39(7):746–53.
96. Kagan HM, Sullivan KA. Lysyl oxidase: preparation and role in elastin biosynthesis. Methods Enzymol. 1982;82 Pt A:637–50.
97. Schräder CU, Heinz A, Majovsky P, Karaman Mayack B, Brinckmann J, Sippl W, et al. Elastin is heterogeneously cross-linked. J Biol Chem. 2018 Sep;293(39):15107–19.
98. Claes E, Atienza JM, Guinea G v, Rojo FJ, Bernal JM, Revuelta JM, et al. Mechanical properties of human coronary arteries. Conf Proc IEEE Eng Med Biol Soc. 2010;2010:3792–5.
99. Mecham RP. Elastin in lung development and disease pathogenesis. Matrix Biol. 2018 Nov;73:6–20.
100. Mozafari H, Zhou C, Gu L. Mechanical contribution of vascular smooth muscle cells in the tunica media of artery. Nanotechnol Rev. 2019;8(1):50–60.
101. Oxlund H, Manschot J, Viidik A. The role of elastin in the mechanical properties of skin. J Biomech. 1988;21(3):213–8.
102. Wagenseil JE, Mecham RP. Elastin in large artery stiffness and hypertension. J Cardiovasc Transl Res. 2012 Jun;5(3):264–73.
103. Wang Y, Hahn J, Zhang Y. Mechanical properties of arterial elastin with water loss. J Biomech Eng. 2018 Apr;140(4):410121–8.
104. Armentano RL, Levenson J, Barra JG, Fischer EI, Breitbart GJ, Pichel RH, et al. Assessment of elastin and collagen contribution to aortic elasticity in conscious dogs. Am J Physiol. 1991 Jun;260(6 Pt 2):H1870-7.
105. Caldini EG, Caldini N, De-Pasquale V, Strocchi R, Guizzardi S, Ruggeri A, et al. Distribution of elastic system fibres in the rat tail tendon and its associated sheaths. Acta Anat (Basel). 1990;139(4):341–8.
106. Cooper RR, Misol S. Tendon and ligament insertion. A light and electron microscopic study. J Bone Joint Surg Am. 1970 Jan;52(1):1–20.
107. Eekhoff JD, Fang F, Kahan LG, Espinosa G, Cocciolone AJ, Wagenseil JE, et al. Functionally distinct tendons from elastin haploinsufficient mice exhibit mild stiffening and tendon-specific structural alteration. J Biomech Eng. 2017 Nov;139(11):1110031–9.
108. Godinho MSC, Thorpe CT, Greenwald SE, Screen HRC. Elastin is localised to the interfascicular matrix of energy storing tendons and becomes increasingly disorganised with ageing. Sci Rep. 2017;7(1):9713.

109. Grant TM, Thompson MS, Urban J, Yu J. Elastic fibres are broadly distributed in tendon and highly localized around tenocytes. J Anat. 2013/04/15. 2013 Jun;222(6):573–9.
110. Maganaris CN, Narici M v. Mechanical Properties of Tendons. In: Maffulli N, Renström P, Leadbetter WB, editors. Tendon injuries: basic science and clinical medicine. London: Springer London; 2005. p. 14–21.
111. Martin RB, Burr DB, Sharkey NA. Mechanical properties of ligament and tendon. In: Skeletal Tissue Mechanics. New York, NY: Springer New York; 1998. p. 309–48.
112. Özkaya N, Leger D, Goldsheyder D, Nordin M. Mechanical properties of biological tissues. In: Fundamentals of Biomechanics: Equilibrium, Motion, and Deformation. Cham: Springer International Publishing; 2017. p. 361–87.
113. Danto MI, Woo SL. The mechanical properties of skeletally mature rabbit anterior cruciate ligament and patellar tendon over a range of strain rates. J Orthop Res. 1993 Jan;11(1):58–67.
114. Kösters A, Wiesinger HP, Bojsen-Møller J, Müller E, Seynnes OR. Influence of loading rate on patellar tendon mechanical properties in vivo. Clin Biomech (Bristol, Avon). 2014 Mar;29(3):323–9.
115. Svensson RB, Hassenkam T, Hansen P, Magnusson SP Viscoelastic behavior of discrete human collagen fibrils. J Mech Behav Biomed Mater. 2010;3(1):112–5.
116. Theis N, Mohagheghi AA, Korff T. Method and strain rate dependence of Achilles tendon stiffness. J Electromyogr Kinesiol. 2012 Dec;22(6):947–53.
117. Bonner TJ, Newell N, Karunaratne A, Pullen AD, Amis AA, M J Bull A, et al. Strain-rate sensitivity of the lateral collateral ligament of the knee. J Mech Behav Biomed Mater. 2015 Jan;41:261–70.
118. Lewis G, Shaw KM. Tensile properties of human tendo Achillis: effect of donor age and strain rate. J Foot Ankle Surg. 1997;36(6):435–45.
119. Shaw KM, Lewis G. Tensile properties of human Achilles tendon. In: Proceedings of the 1997 16 Southern Biomedical Engineering Conference. 1997. p. 338–41.
120. Pioletti DP, Rakotomanana LR, Leyvraz PF. Strain rate effect on the mechanical behavior of the anterior cruciate ligament-bone complex. Med Eng Phys. 1999 Mar;21(2):95–100.
121. Woo SL, Peterson RH, Ohland KJ, Sites TJ, Danto MI. The effects of strain rate on the properties of the medial collateral ligament in skeletally immature and

mature rabbits: a biomechanical and histological study. J Orthop Res. 1990 Sep;8(5):712–21.

122. Maganaris CN, Paul JP. Hysteresis measurements in intact human tendon. J Biomech. 2000;33(12):1723–7.
123. Finni T, Peltonen J, Stenroth L, Cronin NJ. Viewpoint: On the hysteresis in the human Achilles tendon. J Appl Physiol (1985). 2013 Feb;114(4):515–7.
124. Wilson AM, Goodship AE. Exercise-induced hyperthermia as a possible mechanism for tendon degeneration. J Biomech. 1994 Jul;27(7):899–905.
125. Ker RF. Dynamic tensile properties of the plantaris tendon of sheep (Ovis aries). J Exp Biol. 1981 Aug;93:283–302.
126. Butler DL, Grood ES, Noyes FR, Zernicke RF. Biomechanics of ligaments and tendons. Exerc Sport Sci Rev. 1978;6:125–81.
127. Woo SL, Debski RE, Zeminski J, Abramowitch SD, Saw SS, Fenwick JA. Injury and repair of ligaments and tendons. Annu Rev Biomed Eng. 2000;2:83–118.
128. Wren TAL, Lindsey DP, Beaupré GS, Carter DR. Effects of creep and cyclic loading on the mechanical properties and failure of human Achilles tendons. Ann Biomed Eng. 2003 Jun;31(6):710–7.
129. Gupta HS, Seto J, Krauss S, Boesecke P, Screen HRC. In situ multi-level analysis of viscoelastic deformation mechanisms in tendon collagen. J Struct Biol. 2010 Feb;169(2):183–91.
130. Paxton JZ, Baar K. Tendon mechanics: the argument heats up. Vol. 103, Journal of applied physiology (Bethesda, Md. : 1985). United States; 2007. p. 423–4.
131. Wu JJ. Quantitative constitutive behaviour and viscoelastic properties of fresh flexor tendons. Int J Artif Organs. 2006 Sep;29(9):852–7.
132. Pal S. Mechanical properties of biological materials. In: Pal S, editor. Design of Artificial Human Joints & Organs. Boston, MA: Springer US; 2014. p. 23–40.
133. Screen HRC. Investigating load relaxation mechanics in tendon. J Mech Behav Biomed Mater. 2008 Jan;1(1):51–8.
134. Screen HRC, Toorani S, Shelton JC. Microstructural stress relaxation mechanics in functionally different tendons. Med Eng Phys. 2013 Jan;35(1):96–102.
135. Legerlotz K, Riley GP, Screen HRC. GAG depletion increases the stress-relaxation response of tendon fascicles, but does not influence recovery. Acta Biomater. 2013 Jun;9(6):6860–6.
136. Robinson PS, Huang TF, Kazam E, Iozzo R v, Birk DE, Soslowsky LJ. Influence of decorin and biglycan on mechanical properties of multiple tendons in knockout mice. J Biomech Eng. 2005 Feb;127(1):181–5.

137. Elliott DM, Robinson PS, Gimbel JA, Sarver JJ, Abboud JA, Iozzo R v, et al. Effect of altered matrix proteins on quasilinear viscoelastic properties in transgenic mouse tail tendons. Ann Biomed Eng. 2003 May;31(5):599–605.
138. Robinson PS, Lin TW, Reynolds PR, Derwin KA, Iozzo R v, Soslowsky LJ. Strain-rate sensitive mechanical properties of tendon fascicles from mice with genetically engineered alterations in collagen and decorin. J Biomech Eng. 2004 Apr;126(2):252–7.
139. Grant TM, Yapp C, Chen Q, Czernuszka JT, Thompson MS. The mechanical, structural, and compositional changes of tendon exposed to elastase. Ann Biomed Eng. 2015 Oct;43(10):2477–86.
140. Magnusson SP, Narici M v, Maganaris CN, Kjaer M. Human tendon behaviour and adaptation, in vivo. J Physiol. 2008 Jan;586(1):71–81.
141. Halper J. Advances in the use of growth factors for treatment of disorders of soft tissues. Adv Exp Med Biol. 2014;802:59–76.
142. Chiquet M, Gelman L, Lutz R, Maier S. From mechanotransduction to extracellular matrix gene expression in fibroblasts. Biochim Biophys Acta. 2009 May;1793(5):911–20.
143. Riley GP, Curry V, DeGroot J, van El B, Verzijl N, Hazleman BL, et al. Matrix metalloproteinase activities and their relationship with collagen remodelling in tendon pathology. Matrix Biol. 2002 Mar;21(2):185–95.
144. Hannafin JA, Arnoczky SP, Hoonjan A, Torzilli PA. Effect of stress deprivation and cyclic tensile loading on the material and morphologic properties of canine flexor digitorum profundus tendon: an in vitro study. J Orthop Res. 1995 Nov;13(6):907–14.
145. Henshaw DR, Attia E, Bhargava M, Hannafin JA. Canine ACL fibroblast integrin expression and cell alignment in response to cyclic tensile strain in three-dimensional collagen gels. J Orthop Res. 2006 Mar;24(3):481–90.
146. Miyaki S, Ushida T, Nemoto K, Shimojo H, Itabashi A, Ochiai N, et al. Mechanical stretch in anterior cruciate ligament derived cells regulates type I collagen and decorin expression through extracellular signal-regulated kinase 1/2 pathway. Materials Science and Engineering: C. 2001;17(1):91–4.
147. Park SA, Kim IA, Lee YJ, Shin JW, Kim CR, Kim JK, et al. Biological responses of ligament fibroblasts and gene expression profiling on micropatterned silicone substrates subjected to mechanical stimuli. J Biosci Bioeng. 2006 Nov;102(5):402–12.

148. Yang G, Crawford RC, Wang JHC. Proliferation and collagen production of human patellar tendon fibroblasts in response to cyclic uniaxial stretching in serum-free conditions. J Biomech. 2004 Oct;37(10):1543–50.
149. Zeichen J, van Griensven M, Bosch U. The proliferative response of isolated human tendon fibroblasts to cyclic biaxial mechanical strain. Am J Sports Med. 2000;28(6):888–92.
150. Toyoda T, Matsumoto H, Fujikawa K, Saito S, Inoue K. Tensile load and the metabolism of anterior cruciate ligament cells. Clin Orthop Relat Res. 1998 Aug;(353):247–55.
151. Kim SG, Akaike T, Sasagaw T, Atomi Y, Kurosawa H. Gene expression of type I and type III collagen by mechanical stretch in anterior cruciate ligament cells. Cell Struct Funct. 2002 Jun;27(3):139–44.
152. Michna H, Hartmann G. Adaptation of tendon collagen to exercise. Int Orthop. 1989;13(3):161–5.
153. Woo SL, Ritter MA, Amiel D, Sanders TM, Gomez MA, Kuei SC, et al. The biomechanical and biochemical properties of swine tendons--long term effects of exercise on the digital extensors. Connect Tissue Res. 1980;7(3):177–83.
154. Reeves ND, Maganaris CN, Narici M v. Effect of strength training on human patella tendon mechanical properties of older individuals. J Physiol. 2003 May;548(Pt 3):971–81.
155. Buckley MR, Evans EB, Matuszewski PE, Chen YL, Satchel LN, Elliott DM, et al. Distributions of types I, II and III collagen by region in the human supraspinatus tendon. Connect Tissue Res. 2013;54(6):374–9.
156. Majima T, Marchuk LL, Sciore P, Shrive NG, Frank CB, Hart DA. Compressive compared with tensile loading of medial collateral ligament scar in vitro uniquely influences mRNA levels for aggrecan, collagen type II, and collagenase. J Orthop Res. 2000 Jul;18(4):524–31.
157. Robbins JR, Evanko SP, Vogel KG. Mechanical loading and TGF-beta regulate proteoglycan synthesis in tendon. Arch Biochem Biophys. 1997 Jun;342(2):203–11.
158. Shim JW, Elder SH. Influence of cyclic hydrostatic pressure on fibrocartilaginous metaplasia of Achilles tendon fibroblasts. Biomech Model Mechanobiol. 2006 Nov;5(4):247–52.
159. Benjamin M, Ralphs JR. Fibrocartilage in tendons and ligaments--an adaptation to compressive load. J Anat. 1998 Nov;193 (Pt 4(Pt 4):481–94.

160. Sun HB, Li Y, Fung DT, Majeska RJ, Schaffler MB, Flatow EL. Coordinate regulation of IL-1beta and MMP-13 in rat tendons following subrupture fatigue damage. Clin Orthop Relat Res. 2008 Jul;466(7):1555–61.
161. Zhou D, Lee HS, Villarreal F, Teng A, Lu E, Reynolds S, et al. Differential MMP-2 activity of ligament cells under mechanical stretch injury: an in vitro study on human ACL and MCL fibroblasts. J Orthop Res. 2005 Jul;23(4):949–57.
162. Kalson NS, Holmes DF, Herchenhan A, Lu Y, Starborg T, Kadler KE. Slow stretching that mimics embryonic growth rate stimulates structural and mechanical development of tendon-like tissue in vitro. Dev Dyn. 2011 Nov;240(11):2520–8.
163. Ng BH, Chou SM, Krishna V. The influence of gripping techniques on the tensile properties of tendons. Proc Inst Mech Eng H. 2005 Sep;219(5):349–54.
164. Cheung JTM, Zhang M. A serrated jaw clamp for tendon gripping. Med Eng Phys. 2006 May;28(4):379–82.
165. Kiss MO, Hagemeister N, Levasseur A, Fernandes J, Lussier B, Petit Y. A low-cost thermoelectrically cooled tissue clamp for in vitro cyclic loading and load-to-failure testing of muscles and tendons. Med Eng Phys. 2009 Nov;31(9):1182–6.
166. Riemersa DJ, Schamhardt HC. The cryo-jaw, a clamp designed for in vitro rheology studies of horse digital flexor tendons. J Biomech. 1982;15(8):619–20.
167. Bowser JE, Elder SH, Rashmir-Raven AM, Swiderski CE. A cryogenic clamping technique that facilitates ultimate tensile strength determinations in tendons and ligaments. Vet Comp Orthop Traumatol. 2011;24(5):370–3.
168. Wieloch P, Buchmann G, Roth W, Rickert M. A cryo-jaw designed for in vitro tensile testing of the healing Achilles tendons in rats. J Biomech. 2004 Nov;37(11):1719–22.
169. Sharkey NA, Smith TS, Lundmark DC. Freeze clamping musculo-tendinous junctions for in vitro simulation of joint mechanics. J Biomech. 1995 May;28(5):631–5.
170. KarisAllen JJ, Veres SP. Effect of testing temperature on the nanostructural response of tendon to tensile mechanical overload. J Biomech. 2020 May;104:109720.
171. Bass CR, Planchak CJ, Salzar RS, Lucas SR, Rafaels KA, Shender BS, et al. The temperature-dependent viscoelasticity of porcine lumbar spine ligaments. Spine (Phila Pa 1976). 2007 Jul;32(16):E436-42.

172. Lam TC, Thomas CG, Shrive NG, Frank CB, Sabiston CP. The effects of temperature on the viscoelastic properties of the rabbit medial collateral ligament. J Biomech Eng. 1990 May;112(2):147–52.
173. Shi D, Wang D, Wang C, Liu A. A novel, inexpensive and easy to use tendon clamp for in vitro biomechanical testing. Med Eng Phys. 2012 May;34(4):516–20.
174. Feng L, Jasiuk I. Effect of specimen geometry on tensile strength of cortical bone. J Biomed Mater Res A. 2010 Nov;95(2):580–7.
175. Yoshihara H, Yoshinobu M. Effects of specimen configuration and measurement method of strain on the characterization of tensile properties of paper. Journal of Wood Science. 2014;60(4):287–93.
176. Readioff R, Geraghty B, Elsheikh A, Comerford E. Viscoelastic characteristics of the canine cranial cruciate ligament complex at slow strain rates. PeerJ. 2020;8:e10635.
177. Rosario M v., Roberts TJ. Loading rate has little Influence on tendon fascicle mechanics. Front Physiol. 2020;11.
178. Ravary B, Pourcelot P, Bortolussi C, Konieczka S, Crevier-Denoix N. Strain and force transducers used in human and veterinary tendon and ligament biomechanical studies. Clin Biomech (Bristol, Avon). 2004 Jun;19(5):433–47.
179. Jansen MO, Schamhardt HC, van den Bogert AJ, Hartman W. Mechanical properties of the tendinous equine interosseus muscle are affected by in vivo transducer implantation. J Biomech. 1998 May;31(5):485–90.
180. van Weeren PR, Jansen MO, van den Bogert AJ, Barneveld A. A kinematic and strain gauge study of the reciprocal apparatus in the equine hind limb. J Biomech. 1992 Nov;25(11):1291–301.
181. Riemersma DJ, van den Bogert AJ, Jansen MO, Schamhardt HC. Tendon strain in the forelimbs as a function of gait and ground characteristics and in vitro limb loading in ponies. Equine Vet J. 1996 Mar;28(2):133–8.
182. Herzog W, Archambault JM, Leonard TR, Nguyen HK. Evaluation of the implantable force transducer for chronic tendon-force recordings. J Biomech. 1996 Jan;29(1):103–9.
183. Herzog W, Hasler EM, Leonard TR. In-situ calibration of the implantable force transducer. J Biomech. 1996 Dec;29(12):1649–52.
184. Howe JG, Wertheimer C, Johnson RJ, Nichols CE, Pope MH, Beynnon B. Arthroscopic strain gauge measurement of the normal anterior cruciate ligament. Arthroscopy. 1990;6(3):198–204.

185. Fleming BC, Beynnon BD, Tohyama H, Johnson RJ, Nichols CE, Renström P, et al. Determination of a zero strain reference for the anteromedial band of the anterior cruciate ligament. J Orthop Res. 1994 Nov;12(6):789–95.
186. Markolf KL, Willems MJ, Jackson SR, Finerman GA. In situ calibration of miniature sensors implanted into the anterior cruciate ligament part I: strain measurements. J Orthop Res. 1998 Jul;16(4):455–63.
187. Carvalho C, Slagmolen P, Bogaerts S, Scheys L, D'hooge J, Peers K, et al. 3D tendon strain estimation using high-frequency volumetric ultrasound images: a feasibility study. Ultrason Imaging. 2018 Mar;40(2):67–83.
188. Smallcomb M, Elliott J, Khandare S, Butt AA, Vidt ME, Simon JC. Focused ultrasound mechanical disruption of ex vivo rat tendon. IEEE Trans Ultrason Ferroelectr Freq Control. 2021 Sep;68(9):2981–6.
189. Gilchrist CL, Xia JQ, Setton LA, Hsu EW. High-resolution determination of soft tissue deformations using MRI and first-order texture correlation. IEEE Trans Med Imaging. 2004 May;23(5):546–53.
190. Khodabakhshi G, Walker D, Scutt A, Way L, Cowie RM, Hose DR. Measuring three-dimensional strain distribution in tendon. J Microsc. 2013 Mar;249(3):195–205.
191. Boutry CM, Kaizawa Y, Schroeder BC, Chortos A, Legrand A, Wang Z, et al. A stretchable and biodegradable strain and pressure sensor for orthopaedic application. Nat Electron. 2018;1(5):314–21.
192. Kennedy JC, Hawkins RJ, Willis RB. Strain gauge analysis of knee ligaments. Clin Orthop Relat Res. 1977;(129):225–9.
193. Zens M, Ruhhammer J, Goldschmidtboeing F, Woias P, Feucht MJ, Mayr HO, et al. A new approach to determine ligament strain using polydimethylsiloxane strain gauges: exemplary measurements of the anterolateral ligament. J Biomech Eng. 2014 Dec;136(12):124504.
194. Hussein M. Effects of strain rate and temperature on the mechanical behavior of carbon black reinforced elastomers based on butyl rubber and high molecular weight polyethylene. Results Phys. 2018;9:511–7.
195. Richeton J, Schlatter G, Vecchio KS, Rémond Y, Ahzi S. A unified model for stiffness modulus of amorphous polymers across transition temperatures and strain rates. Polymer (Guildf). 2005;46(19):8194–201.
196. Nazarychev VM, Lyulin A v, Larin S v, Gurtovenko AA, Kenny JM, Lyulin S v. Molecular dynamics simulations of uniaxial deformation of thermoplastic polyimides. Soft Matter. 2016;12(17):3972–81.

197. Ree T, Eyring H. Theory of non-newtonian flow. I. Solid Plastic System. J Appl Phys. 1955;26(7):793–800.
198. Eyring H. Viscosity, plasticity, and diffusion as examples of absolute reaction rates. J Chem Phys. 1936;4(4):283–91.
199. Richeton J, Ahzi S, Daridon L. Thermodynamic investigation of yield-stress models for amorphous polymers. Philosophical Magazine. 2007;87(24):3629–43.
200. Argon AS. A theory for the low-temperature plastic deformation of glassy polymers. The Philosophical Magazine: A Journal of Theoretical Experimental and Applied Physics. 1973;28(4):839–65.
201. Povolo F, Hermida ÉB. Phenomenological description of strain rate and temperature-dependent yield stress of PMMA. J Appl Polym Sci. 1995;58(1):55–68.
202. Robertson RE. Theory for the plasticity of glassy polymers. J Chem Phys. 1966;44(10):3950–6.
203. Ciarletta P, ben Amar M. A finite dissipative theory of temporary interfibrillar bridges in the extracellular matrix of ligaments and tendons. J R Soc Interface. 2009 Oct;6(39):909–24.
204. Clemmer J, Liao J, Davis D, Horstemeyer MF, Williams LN. A mechanistic study for strain rate sensitivity of rabbit patellar tendon. J Biomech. 2010 Oct;43(14):2785–91.
205. Ng BH, Chou SM, Lim BH, Chong A. Strain rate effect on the failure properties of tendons. Proc Inst Mech Eng H. 2004;218(3):203–6.
206. Chambers NC, Herod TW, Veres SP. Ultrastructure of tendon rupture depends on strain rate and tendon type. J Orthop Res. 2018 Nov;36(11):2842–50.
207. Edwards JH, Ingham E, Herbert A. Decellularisation affects the strain rate dependent and dynamic mechanical properties of a xenogeneic tendon intended for anterior cruciate ligament replacement. J Mech Behav Biomed Mater. 2019;91:18–23.
208. Giesberts RB, G Hekman EE, Verkerke GJ, M Maathuis PG. Rapid decrease of cast-induced forces during the treatment of clubfoot using the Ponseti method. Bone Joint J. 2018 Dec;100-B(12):1655–60.
209. Cocciolone AJ, Hawes JZ, Staiculescu MC, Johnson EO, Murshed M, Wagenseil JE. Elastin, arterial mechanics, and cardiovascular disease. Am J Physiol Heart Circ Physiol. 2018 Aug;315(2):H189–205.

210. Hill MA, Nourian Z, Ho IL, Clifford PS, Martinez-Lemus L, Meininger GA. Small artery elastin distribution and architecture-focus on three dimensional organization. Microcirculation. 2016 Nov;23(8):614–20.
211. Gonçalves CA, Figueiredo MH, Bairos VA. Three-dimensional organization of the elastic fibres in the rat lung. Anat Rec. 1995 Sep;243(1):63–70.
212. Sun Q, Baues M, Klinkhammer BM, Ehling J, Djudjaj S, Drude NI, et al. Elastin imaging enables noninvasive staging and treatment monitoring of kidney fibrosis. Sci Transl Med. 2019;11(486).
213. Taszkun I, Tomaszewska E, Dobrowolski P, Żmuda A, Sitkowski W, Muszyński S. Evaluation of collagen and elastin content in skin of multiparous minks receiving feed contaminated with deoxynivalenol (DON, Vomitoxin) with or without Bentonite supplementation. Animals (Basel). 2019 Dec;9(12).
214. Henninger HB, Valdez WR, Scott SA, Weiss JA. Elastin governs the mechanical response of medial collateral ligament under shear and transverse tensile loading. Acta Biomater. 2015 Oct;25:304–12.
215. Henninger HB, Underwood CJ, Romney SJ, Davis GL, Weiss JA. Effect of elastin digestion on the quasi-static tensile response of medial collateral ligament. J Orthop Res. 2013 Aug;31(8):1226–33.
216. Józsa L, Bálint JB, Réffy A, Demel Z. Histochemical and ultrastructural study of adult human tendon. Acta Histochem. 1979;65(2):250–7.
217. Parry DA, Craig AS. Collagen fibrils and elastic fibers in rat-tail tendon: an electron microscopic investigation. Biopolymers. 1978 Apr;17(4):843–5.
218. Ippolito E, Natali PG, Postacchini F, Accinni L, de Martino C. Morphological, immunochemical, and biochemical study of rabbit achilles tendon at various ages. J Bone Joint Surg Am. 1980;62(4):583–98.
219. Pang X, Wu JP, Allison GT, Xu J, Rubenson J, Zheng MH, et al. Three dimensional microstructural network of elastin, collagen, and cells in Achilles tendons. J Orthop Res. 2017 Jun;35(6):1203–14.
220. Onthank D, Yalamanchili P, Cesati R, Lazewatsky J, Azure M, Hayes M, et al. Abstract 1914: BMS753951: A novel low molecular weight magnetic resonance contrast agent selective for arterial wall imaging. Circulation. 2007;116(suppl_16):II_411-II_412.
221. Makowski MR, Wiethoff AJ, Blume U, Cuello F, Warley A, Jansen CHP, et al. Assessment of atherosclerotic plaque burden with an elastin-specific magnetic resonance contrast agent. Nat Med. 2011 Mar;17(3):383–8.
222. von Bary C, Makowski M, Preissel A, Keithahn A, Warley A, Spuentrup E, et al. MRI of coronary wall remodeling in a swine model of coronary injury using

an elastin-binding contrast agent. Circ Cardiovasc Imaging. 2011 Mar;4(2):147–55.

223. Ritty TM, Ditsios K, Starcher BC. Distribution of the elastic fiber and associated proteins in flexor tendon reflects function. Anat Rec. 2002;268(4):430–40.

224. Kazlouskaya V, Malhotra S, Lambe J, Idriss MH, Elston D, Andres C. The utility of elastic Verhoeff-Van Gieson staining in dermatopathology. J Cutan Pathol. 2013 Feb;40(2):211–25.

225. Percival K, Radi Z. Comparison of five elastin histochemical stains to identify pulmonary small vasculature. J Histotechnol. 2017;40(3):73–8.

226. Nwaneshiudu A, Kuschal C, Sakamoto FH, Anderson RR, Schwarzenberger K, Young RC. Introduction to confocal microscopy. J Invest Dermatol. 2012 Dec;132(12):e3.

227. Richards-Kortum R, Sevick-Muraca E. Quantitative optical spectroscopy for tissue diagnosis. Annu Rev Phys Chem. 1996;47:555–606.

228. Sugita S, Matsumoto T. Multiphoton microscopy observations of 3D elastin and collagen fiber microstructure changes during pressurization in aortic media. Biomech Model Mechanobiol. 2017 Jun;16(3):763–73.

229. Chen H, Slipchenko MN, Liu Y, Zhao X, Cheng JX, Lanir Y, et al. Biaxial deformation of collagen and elastin fibers in coronary adventitia. J Appl Physiol (1985). 2013 Dec;115(11):1683–93.

230. Levillain A, Orhant M, Turquier F, Hoc T. Contribution of collagen and elastin fibers to the mechanical behavior of an abdominal connective tissue. J Mech Behav Biomed Mater. 2016 Aug;61:308–17.

231. Park CY, Lee JK, Kahook MY, Schultz JS, Zhang C, Chuck RS. Revisiting ciliary muscle tendons and their connections with the trabecular meshwork by two photon excitation microscopic imaging. Invest Ophthalmol Vis Sci. 2016 Mar;57(3):1096–105.

232. He B, Wu JP, Chim SM, Xu J, Kirk TB. Microstructural analysis of collagen and elastin fibres in the kangaroo articular cartilage reveals a structural divergence depending on its local mechanical environment. Osteoarthritis Cartilage. 2013;21(1):237–45.

233. Fang F, Lake SP. Multiscale mechanical integrity of human supraspinatus tendon in shear after elastin depletion. J Mech Behav Biomed Mater. 2016 Oct;63:443–55.

234. Ricard C, Vial JC, Douady J, van der Sanden B. In vivo imaging of elastic fibers using sulforhodamine B. J Biomed Opt. 2007;12(6):64017.

235. Im K, Mareninov S, Diaz MFP, Yong WH. An introduction to performing immunofluorescence staining. Methods Mol Biol. 2019;1897:299–311.
236. Kumari P. Congenital clubfoot: a comprehensive review. Orthopedics and Rheumatology Open access Journal. 2017;8.
237. Vaishy AK, Arif M, Acharya D, Choudhary R, Seervi PM, Kumar R. Influence of beginning time of casting for clubfoot treatment by Ponseti method in different age group infants: a retrospective study. Indian J Orthop. 2020 Feb;54(1):55–9.
238. Dietz FR, Noonan K. Treatment of clubfoot using the Ponseti method. JBJS Essent Surg Tech. 2016 Sep;6(3):e28.
239. Csóka TB, Frost GI, Stern R. Hyaluronidases in tissue invasion. Invasion Metastasis. 1997;17(6):297–311.
240. Vafek EC, Plate JF, Friedman E, Mannava S, Scott AT, Danelson KA. The effect of strain and age on the mechanical properties of rat Achilles tendons. Muscles Ligaments Tendons J. 2017;7(3):548–53.
241. Bah I, Fernandes NRJ, Chimenti RL, Ketz J, Flemister AS, Buckley MR. Tensile mechanical changes in the Achilles tendon due to insertional Achilles tendinopathy. J Mech Behav Biomed Mater. 2020;112:104031.
242. Barrett JM, Fewster KM, Cudlip AC, Dickerson CR, Callaghan JP. The rate of tendon failure in a collagen fibre recruitment-based model. J Mech Behav Biomed Mater. 2021 Mar;115:104273.
243. Shepherd JH, Legerlotz K, Demirci T, Klemt C, Riley GP, Screen HRC. Functionally distinct tendon fascicles exhibit different creep and stress relaxation behaviour. Proc Inst Mech Eng H. 2014 Jan;228(1):49–59.
244. Susilo ME, Paten JA, Sander EA, Nguyen TD, Ruberti JW. Collagen network strengthening following cyclic tensile loading. Interface Focus. 2016 Feb;6(1):20150088.
245. Freedman BR, Rodriguez AB, Leiphart RJ, Newton JB, Ban E, Sarver JJ, et al. Dynamic loading and tendon healing affect multiscale tendon properties and ECM stress transmission. Sci Rep. 2018 Jul;8(1):10854.
246. Arampatzis A, Karamanidis K, Albracht K. Adaptational responses of the human Achilles tendon by modulation of the applied cyclic strain magnitude. J Exp Biol. 2007 Aug;210(Pt 15):2743–53.
247. Schatzmann L, Brunner P, Stäubli HU. Effect of cyclic preconditioning on the tensile properties of human quadriceps tendons and patellar ligaments. Knee Surg Sports Traumatol Arthrosc. 1998;6 Suppl 1:S56-61.

248. Miller KS, Edelstein L, Connizzo BK, Soslowsky LJ. Effect of preconditioning and stress relaxation on local collagen fiber re-alignment: inhomogeneous properties of rat supraspinatus tendon. J Biomech Eng. 2012 Mar;134(3):31007.
249. Szczesny SE, Caplan JL, Pedersen P, Elliott DM. Quantification of interfibrillar shear stress in aligned soft collagenous tissues via notch tension testing. Sci Rep. 2015;5(1):14649.
250. Gathercole LJ, Keller A. Crimp morphology in the fibre-forming collagens. Matrix. 1991;11(3):214–34.
251. Atkinson TS, Ewers BJ, Haut RC. The tensile and stress relaxation responses of human patellar tendon varies with specimen cross-sectional area. J Biomech. 1999 Sep;32(9):907–14.
252. Hansen KA, Weiss JA, Barton JK. Recruitment of tendon crimp with applied tensile strain. J Biomech Eng. 2002 Feb;124(1):72–7.
253. Sasaki N, Odajima S. Elongation mechanism of collagen fibrils and force-strain relations of tendon at each level of structural hierarchy. J Biomech. 1996 Sep;29(9):1131–6.
254. Franchi M, Fini M, Quaranta M, de Pasquale V, Raspanti M, Giavaresi G, et al. Crimp morphology in relaxed and stretched rat Achilles tendon. J Anat. 2007 Jan;210(1):1–7.
255. Herchenhan A, Kalson NS, Holmes DF, Hill P, Kadler KE, Margetts L. Tenocyte contraction induces crimp formation in tendon-like tissue. Biomech Model Mechanobiol. 2012 Mar;11(3–4):449–59.
256. Shah JS, Palacios E, Palacios L. Development of crimp morphology and cellular changes in chick tendons. Dev Biol. 1982 Dec;94(2):499–504.
257. Legerlotz K, Dorn J, Richter J, Rausch M, Leupin O. Age-dependent regulation of tendon crimp structure, cell length and gap width with strain. Acta Biomater. 2014;10(10):4447–55.
258. Patterson-Kane JC, Firth EC, Goodship AE, Parry DA. Age-related differences in collagen crimp patterns in the superficial digital flexor tendon core region of untrained horses. Aust Vet J. 1997 Jan;75(1):39–44.
259. Patterson-Kane JC, Parry DA, Goodship AE, Firth EC. Exercise modifies the age-related change in crimp pattern in the core region of the equine superficial digital flexor tendon. N Z Vet J. 1997 Aug;45(4):135–9.
260. Spiesz EM, Thorpe CT, Thurner PJ, Screen HRC. Structure and collagen crimp patterns of functionally distinct equine tendons, revealed by quantitative polarised light microscopy (qPLM). Acta Biomater. 2018 Apr;70:281–92.

261. Diamant J, Keller A, Baer E, Litt M, Arridge RG. Collagen; ultrastructure and its relation to mechanical properties as a function of ageing. Proc R Soc Lond B Biol Sci. 1972 Mar;180(1060):293–315.
262. Franchi M, Torricelli P, Giavaresi G, Fini M. Role of moderate exercising on Achilles tendon collagen crimping patterns and proteoglycans. Connect Tissue Res. 2013;54(4–5):267–74.
263. Wood TO, Cooke PH, Goodship AE. The effect of exercise and anabolic steroids on the mechanical properties and crimp morphology of the rat tendon. Am J Sports Med. 1988;16(2):153–8.
264. Järvinen TAH, Järvinen TLN, Kannus P, Józsa L, Järvinen M. Collagen fibres of the spontaneously ruptured human tendons display decreased thickness and crimp angle. J Orthop Res. 2004 Nov;22(6):1303–9.
265. Spiesz EM, Thorpe CT, Chaudhry S, Riley GP, Birch HL, Clegg PD, et al. Tendon extracellular matrix damage, degradation and inflammation in response to in vitro overload exercise. J Orthop Res. 2015 Jun;33(6):889–97.
266. Thorpe CT, Udeze CP, Birch HL, Clegg PD, Screen HRC. Specialization of tendon mechanical properties results from interfascicular differences. J R Soc Interface. 2012 Nov;9(76):3108–17.
267. Fang F, Lake SP. Multiscale strain analysis of tendon subjected to shear and compression demonstrates strain attenuation, fiber sliding, and reorganization. J Orthop Res. 2015 Nov;33(11):1704–12.
268. Lavagnino M, Wall ME, Little D, Banes AJ, Guilak F, Arnoczky SP. Tendon mechanobiology: current knowledge and future research opportunities. J Orthop Res. 2015 Jun;33(6):813–22.
269. Zhang C, Zhu J, Zhou Y, Thampatty BP, Wang JHC. Tendon stem/progenitor cells and their interactions with extracellular matrix and mechanical loading. Stem Cells Int. 2019;2019:3674647.
270. Thorpe CT, Peffers MJ, Simpson D, Halliwell E, Screen HRC, Clegg PD. Anatomical heterogeneity of tendon: fascicular and interfascicular tendon compartments have distinct proteomic composition. Sci Rep. 2016 Feb;6:20455.
271. Duca L, Blaise S, Romier B, Laffargue M, Gayral S, el Btaouri H, et al. Matrix ageing and vascular impacts: focus on elastin fragmentation. Cardiovasc Res. 2016 Jun;110(3):298–308.
272. Baud S, Duca L, Bochicchio B, Brassart B, Belloy N, Pepe A, et al. Elastin peptides in aging and pathological conditions. Biomol Concepts. 2013 Feb;4(1):65–76.

273. Chambers ES, Vukmanovic-Stejic M. Skin barrier immunity and ageing. Immunology. 2020 Jun;160(2):116–25.
274. Fonck E, Feigl GG, Fasel J, Sage D, Unser M, Rüfenacht DA, et al. Effect of aging on elastin functionality in human cerebral arteries. Stroke. 2009 Jul;40(7):2552–6.
275. Kohn JC, Lampi MC, Reinhart-King CA. Age-related vascular stiffening: causes and consequences. Front Genet. 2015;6:112.
276. Tarakanova A, Chang SW, Buehler MJ. Computational materials science of bionanomaterials: structure, mechanical properties and applications of elastin and collagen proteins. In: Bhushan B, Luo D, Schricker SR, Sigmund W, Zauscher S, editors. Handbook of Nanomaterials Properties . Berlin, Heidelberg: Springer Berlin Heidelberg; 2014. p. 941–62.
277. Ozsvar J, Yang C, Cain SA, Baldock C, Tarakanova A, Weiss AS. Tropoelastin and elastin assembly. Front Bioeng Biotechnol. 2021;9:138.
278. Urry DW, Luan CH, Peng SQ. Molecular biophysics of elastin structure, function and pathology. Ciba Found Symp. 1995;192:4–30.
279. Gosline JM. Hydrophobic interaction and a model for the elasticity of elastin. Biopolymers. 1978 Mar;17(3):677–95.
280. Mecham RP. Methods in elastic tissue biology: elastin isolation and purification. Methods. 2008 May;45(1):32–41.
281. Phan Dinh Ty B, Moczar E. Analysis of elastin peptide by reversed-phase high-performance liquid chromatography. J Chromatogr A. 1984;291:445–8.
282. Moczar M, Moczar E, Robert L. Peptides obtained from elastin by hydrolysis with aqueous ethanolic potassium hydroxide. Connect Tissue Res. 1979;6(4):207–13.
283. Guthold M, Liu W, Sparks EA, Jawerth LM, Peng L, Falvo M, et al. A comparison of the mechanical and structural properties of fibrin fibers with other protein fibers. Cell Biochem Biophys. 2007;49(3):165–81.
284. Aaron BB, Gosline JM. Elastin as a random-network elastomer: A mechanical and optical analysis of single elastin fibers. Biopolymers. 1981;20(6):1247–60.
285. Nonaka R, Sato F, Wachi H. Domain 36 of tropoelastin in elastic fiber formation. Biol Pharm Bull. 2014;37(4):698–702.
286. Nagano N, Ota M, Nishikawa K. Strong hydrophobic nature of cysteine residues in proteins. FEBS Lett. 1999;458(1):69–71.
287. Liang J, Fernández JM. Kinetic Measurements on single-molecule disulfide bond cleavage. J Am Chem Soc. 2011 Mar 16;133(10):3528–34.

288. Szoszkiewicz R. Single-molecule studies of disulfide bond reduction pathways used by human thioredoxin. Biophys Chem. 2013;173–174:31–8.
289. Popa I, Kosuri P, Alegre-Cebollada J, Garcia-Manyes S, Fernandez JM. Force dependency of biochemical reactions measured by single-molecule force-clamp spectroscopy. Nat Protoc. 2013;8(7):1261–76.
290. Garcia-Manyes S, Kuo TL, Fernández JM. Contrasting the individual reactive pathways in protein unfolding and disulfide bond reduction observed within a single protein. J Am Chem Soc. 2011 Mar 9;133(9):3104–13.
291. Alegre-Cebollada J, Kosuri P, Rivas-Pardo JA, Fernández JM. Direct observation of disulfide isomerization in a single protein. Nat Chem. 2011;3(11):882–7.
292. Garcia-Manyes S, Liang J, Szoszkiewicz R, Kuo TL, Fernández JM. Force-activated reactivity switch in a bimolecular chemical reaction. Nat Chem. 2009;1(3):236–42.
293. Wiita AP, Perez-Jimenez R, Walther KA, Gräter F, Berne BJ, Holmgren A, et al. Probing the chemistry of thioredoxin catalysis with force. Nature. 2007;450(7166):124–7.
294. Liang J, Fernández JM. Mechanochemistry: one bond at a time. ACS Nano. 2009 Jul 28;3(7):1628–45.
295. Koti Ainavarapu SR, Wiita AP, Dougan L, Uggerud E, Fernandez JM. Single-molecule force spectroscopy measurements of bond elongation during a bimolecular reaction. J Am Chem Soc. 2008 May 1;130(20):6479–87.
296. Kucharski TJ, Huang Z, Yang QZ, Tian Y, Rubin NC, Concepcion CD, et al. Kinetics of thiol/disulfide exchange correlate weakly with the restoring force in the disulfide moiety. Angew Chem Int Ed Engl. 2009;48(38):7040–3.
297. Tian Y, Kucharski TJ, Yang QZ, Boulatov R. Model studies of force-dependent kinetics of multi-barrier reactions. Nat Commun. 2013;4(1):2538.
298. Hofbauer F, Frank I. CPMD simulation of a bimolecular chemical reaction: nucleophilic attack of a disulfide bond under mechanical stress. Chemistry. 2012 Dec;18(51):16332–8.
299. Anjukandi P, Dopieralski P, Ribas-Arino J, Marx D. The effect of tensile stress on the conformational free energy landscape of disulfide bonds. PLoS One. 2014;9(10):e108812.
300. Zhou B, Baldus IB, Li W, Edwards SA, Gräter F. Identification of allosteric disulfides from prestress analysis. Biophys J. 2014 Aug;107(3):672–81.
301. Dopieralski P, Ribas-Arino J, Anjukandi P, Krupicka M, Kiss J, Marx D. The Janus-faced role of external forces in mechanochemical disulfide bond cleavage. Nat Chem. 2013 Aug;5(8):685–91.

302. Keten S, Chou CC, van Duin ACT, Buehler MJ. Tunable nanomechanics of protein disulfide bonds in redox microenvironments. J Mech Behav Biomed Mater. 2012 Jan;5(1):32–40.
303. Baldus IB, Gräter F. Mechanical force can fine-tune redox potentials of disulfide bonds. Biophys J. 2012 Feb;102(3):622–9.
304. Li W, Gräter F. Atomistic evidence of how force dynamically regulates thiol/disulfide exchange. J Am Chem Soc. 2010 Dec;132(47):16790–5.
305. Iozzi MF, Helgaker T, Uggerud E. Influence of external force on properties and reactivity of disulfide bonds. J Phys Chem A. 2011 Mar;115(11):2308–15.
306. Hofbauer F, Frank I. Disulfide bond cleavage: a redox reaction without electron transfer. Chemistry. 2010 May;16(17):5097–101.
307. Dopieralski P, Ribas–Arino J, Anjukandi P, Krupicka M, Marx D. Unexpected mechanochemical complexity in the mechanistic scenarios of disulfide bond reduction in alkaline solution. Nat Chem. 2017;9(2):164–70.
308. Pober BR, Johnson M, Urban Z. Mechanisms and treatment of cardiovascular disease in Williams-Beuren syndrome. J Clin Invest. 2008 May;118(5):1606–15.
309. Kozel BA, Danback JR, Waxler JL, Knutsen RH, de Las Fuentes L, Reusz GS, et al. Williams syndrome predisposes to vascular stiffness modified by antihypertensive use and copy number changes in NCF1. Hypertension. 2014 Jan;63(1):74–9.
310. Arribas SM, Hinek A, González MC. Elastic fibres and vascular structure in hypertension. Pharmacol Ther. 2006 Sep;111(3):771–91.
311. Campa JS, Greenhalgh RM, Powell JT. Elastin degradation in abdominal aortic aneurysms. Atherosclerosis. 1987 May;65(1–2):13–21.
312. Milewicz DM, Guo DC, Tran-Fadulu V, Lafont AL, Papke CL, Inamoto S, et al. Genetic basis of thoracic aortic aneurysms and dissections: focus on smooth muscle cell contractile dysfunction. Annu Rev Genomics Hum Genet. 2008;9:283–302.
313. Basalyga DM, Simionescu DT, Xiong W, Baxter BT, Starcher BC, Vyavahare NR. Elastin degradation and calcification in an abdominal aorta injury model: role of matrix metalloproteinases. Circulation. 2004 Nov;110(22):3480–7.
314. O'Rourke MF, Safar ME, Dzau V. The cardiovascular continuum extended: aging effects on the aorta and microvasculature. Vasc Med. 2010 Dec;15(6):461–8.
315. Hosoda Y, Kawano K, Yamasawa F, Ishii T, Shibata T, Inayama S. Age-dependent changes of collagen and elastin content in human aorta and pulmonary artery. Angiology. 1984 Oct;35(10):615–21.

316. Rauscher S, Pomès R. Structural disorder and protein elasticity. Adv Exp Med Biol. 2012;725:159–83.
317. Karnik SK, Brooke BS, Bayes-Genis A, Sorensen L, Wythe JD, Schwartz RS, et al. A critical role for elastin signaling in vascular morphogenesis and disease. Development. 2003 Jan;130(2):411–23.
318. Heinz A. Elastases and elastokines: elastin degradation and its significance in health and disease. Crit Rev Biochem Mol Biol. 2020 Jun;55(3):252–73.
319. Maquart FX, Pasco S, Ramont L, Hornebeck W, Monboisse JC. An introduction to matrikines: extracellular matrix-derived peptides which regulate cell activity. Implication in tumor invasion. Crit Rev Oncol Hematol. 2004 Mar;49(3):199–202.
320. Robert L, Tixier JM, Berenholc S, Levy O, Hornebeck W. Inhibition of elastase activity in human gingival extracts by elastin peptides. Pathol Biol (Paris). 1992;40(9):879—882.
321. Péterszegi G, Texier S, Robert L. Cell death by overload of the elastin-laminin receptor on human activated lymphocytes: protection by lactose and melibiose. Eur J Clin Invest. 1999 Feb;29(2):166–72.
322. Senior RM, Griffin GL, Mecham RP, Wrenn DS, Prasad KU, Urry DW. Val-Gly-Val-Ala-Pro-Gly, a repeating peptide in elastin, is chemotactic for fibroblasts and monocytes. J Cell Biol. 1984 Sep;99(3):870–4.
323. Long MM, King VJ, Prasad KU, Freeman BA, Urry DW. Elastin repeat peptides as chemoattractants for bovine aortic endothelial cells. J Cell Physiol. 1989 Sep;140(3):512–8.
324. Fülöp TJ, Jacob MP, Varga Z, Foris G, Leövey A, Robert L. Effect of elastin peptides on human monocytes: Ca2+ mobilization, stimulation of respiratory burst and enzyme secretion. Biochem Biophys Res Commun. 1986 Nov;141(1):92–8.
325. Kamoun A, Landeau JM, Godeau G, Wallach J, Duchesnay A, Pellat B, et al. Growth stimulation of human skin fibroblasts by elastin-derived peptides. Cell Adhes Commun. 1995 Nov;3(4):273–81.
326. Brassart B, Fuchs P, Huet E, Alix AJ, Wallach J, Tamburro AM, et al. Conformational dependence of collagenase (matrix metalloproteinase-1) up-regulation by elastin peptides in cultured fibroblasts. J Biol Chem. 2001 Feb;276(7):5222–7.
327. Antonicelli F, Bellon G, Debelle L, Hornebeck W. Elastin-elastases and inflamm-aging. Curr Top Dev Biol. 2007;79:99–155.

328. Robinet A, Fahem A, Cauchard JH, Huet E, Vincent L, Lorimier S, et al. Elastin-derived peptides enhance angiogenesis by promoting endothelial cell migration and tubulogenesis through upregulation of MT1-MMP. J Cell Sci. 2005 Jan;118(Pt 2):343–56.
329. Petersen E, Wågberg F, Angquist KA. Serum concentrations of elastin-derived peptides in patients with specific manifestations of atherosclerotic disease. Eur J Vasc Endovasc Surg. 2002 Nov;24(5):440–4.
330. Phinikaridou A, Lacerda S, Lavin B, Andia ME, Smith A, Saha P, et al. Tropoelastin: A novel marker for plaque progression and instability. Circ Cardiovasc Imaging. 2018 Aug;11(8).
331. Houghton AM, Quintero PA, Perkins DL, Kobayashi DK, Kelley DG, Marconcini LA, et al. Elastin fragments drive disease progression in a murine model of emphysema. J Clin Invest. 2006 Mar;116(3):753–9.
332. Lee SH, Goswami S, Grudo A, Song LZ, Bandi V, Goodnight-White S, et al. Antielastin autoimmunity in tobacco smoking-induced emphysema. Nat Med. 2007 May;13(5):567–9.
333. Gigante A, Chillemi C, Bevilacqua C, Greco F, Bisaccia F, Tamburro AM. Effects of elastin-derived peptide on Achilles' tendon healing: an experimental study. J Mater Sci Mater Med. 2003 Aug;14(8):717–20.
334. Harnett P, Freeman R, Harrison WJ, Brown LC, Beckles V. An accelerated Ponseti versus the standard Ponseti method: a prospective randomised controlled trial. J Bone Joint Surg Br. 2011 Mar;93(3):404–8.
335. Morcuende JA, Abbasi D, Dolan LA, Ponseti I v. Results of an accelerated Ponseti protocol for clubfoot. J Pediatr Orthop. 2005;25(5):623–6.
336. Uitto J, Ryhänen L, Abraham PA, Perejda AJ. Elastin in diseases. Journal of Investigative Dermatology. 1982;79(1, Supplement):160–8.
337. Tsamis A, Krawiec JT, Vorp DA. Elastin and collagen fibre microstructure of the human aorta in ageing and disease: a review. J R Soc Interface. 2013 Jun;10(83):20121004.
338. Maurice P, Blaise S, Gayral S, Debelle L, Laffargue M, Hornebeck W, et al. Elastin fragmentation and atherosclerosis progression: the elastokine concept. Trends Cardiovasc Med. 2013 Aug;23(6):211–21.
339. Sherratt MJ. Tissue elasticity and the ageing elastic fibre. Age (Dordr). 2009 Dec;31(4):305–25.
340. Wang JHC, Guo Q, Li B. Tendon biomechanics and mechanobiology--a minireview of basic concepts and recent advancements. J Hand Ther. 2012;25(2):133–40; quiz 141.

341. Kostrominova TY, Brooks S v. Age-related changes in structure and extracellular matrix protein expression levels in rat tendons. Age (Dordr). 2013 Dec;35(6):2203–14.
342. Liu J, Chou SM, Goh KL. Age effects on the tensile and stress relaxation properties of mouse tail tendons. In: Lim CT, Goh JCH, editors. 13th International Conference on Biomedical Engineering. Berlin, Heidelberg: Springer Berlin Heidelberg; 2009. p. 1631–5.
343. Godinho MS, Thorpe CT, Greenwald SE, Screen HRC. Elastase treatment of tendon specifically impacts the mechanical properties of the interfascicular matrix. Acta Biomater. 2021;123:187–96.
344. Suki B, Bartolák-Suki E, Rocco PRM. Elastase-induced lung emphysema models in mice. Methods Mol Biol. 2017;1639:67–75.
345. Yuan H, Kononov S, Cavalcante FS, Lutchen KR, Ingenito EP, Suki B. Effects of collagenase and elastase on the mechanical properties of lung tissue strips. J Appl Physiol (1985). 2000 Jul;89(1):3–14.
346. Collins MJ, Eberth JF, Wilson E, Humphrey JD. Acute mechanical effects of elastase on the infrarenal mouse aorta: implications for models of aneurysms. J Biomech. 2012 Feb;45(4):660–5.
347. Popov VL, Heß M, Willert E. Viscoelastic materials. In: Handbook of Contact Mechanics: Exact Solutions of Axisymmetric Contact Problems. Berlin, Heidelberg: Springer Berlin Heidelberg; 2019. p. 213–49.
348. Epaarachchi JA. 17 - The effect of viscoelasticity on fatigue behaviour of polymer matrix composites. In: Guedes RM, editor. Creep and Fatigue in Polymer Matrix Composites. Woodhead Publishing; 2011. p. 492–513. (Woodhead Publishing Series in Composites Science and Engineering).
349. Papanicolaou GC, Zaoutsos SP. 1 - Viscoelastic constitutive modeling of creep and stress relaxation in polymers and polymer matrix composites. In: Guedes RM, editor. Creep and Fatigue in Polymer Matrix Composites (Second Edition). Second Edi. Woodhead Publishing; 2019. p. 3–59. (Woodhead Publishing Series in Composites Science and Engineering).
350. Provenzano P, Lakes R, Keenan T, Vanderby RJ. Nonlinear ligament viscoelasticity. Ann Biomed Eng. 2001 Oct;29(10):908–14.
351. Provenzano PP, Lakes RS, Corr DT, Vanderby RJ. Application of nonlinear viscoelastic models to describe ligament behavior. Biomech Model Mechanobiol. 2002 Jun;1(1):45–57.
352. Duenwald SE, Vanderby RJ, Lakes RS. Viscoelastic relaxation and recovery of tendon. Ann Biomed Eng. 2009 Jun;37(6):1131–40.

353. Duenwald SE, Vanderby RJ, Lakes RS. Stress relaxation and recovery in tendon and ligament: experiment and modeling. Biorheology. 2010;47(1):1–14.
354. Roth SP, Erbe I, Burk J. Decellularization of large tendon specimens: combination of manually performed freeze-thaw cycles and detergent treatment. Methods Mol Biol. 2018;1577:227–37.
355. Xu K, Kuntz LA, Foehr P, Kuempel K, Wagner A, Tuebel J, et al. Efficient decellularization for tissue engineering of the tendon-bone interface with preservation of biomechanics. PLoS One. 2017;12(2):e0171577.
356. Lovati AB, Bottagisio M, Moretti M. Decellularized and engineered tendons as biological substitutes: A Critical Review. Stem Cells Int. 2016;2016:7276150.
357. Zitnay JL, Weiss JA. Load transfer, damage, and failure in ligaments and tendons. Journal of Orthopaedic Research. 2018;36(12):3093–104.
358. Kielty CM. Elastic fibres in health and disease. Expert Rev Mol Med. 2006 Aug;8(19):1–23.
359. Guzzoni V, Selistre-de-Araújo HS, Marqueti R de C. Tendon remodeling in response to resistance training, anabolic androgenic steroids and aging. Cells. 2018 Dec;7(12).
360. Screen HRC, Seto J, Krauss S, Boesecke P, Gupta HS. Extrafibrillar diffusion and intrafibrillar swelling at the nanoscale are associated with stress relaxation in the soft collagenous matrix tissue of tendons. Soft Matter. 2011;7(23):11243–51.
361. Machiraju C, Phan AV, Pearsall AW, Madanagopal S. Viscoelastic studies of human subscapularis tendon: relaxation test and a Wiechert model. Comput Methods Programs Biomed. 2006 Jul;83(1):29–33.
362. Babaei B, Davarian A, Pryse KM, Elson EL, Genin GM. Efficient and optimized identification of generalized Maxwell viscoelastic relaxation spectra. J Mech Behav Biomed Mater. 2016;55:32–41.
363. Milz S, Ockert B, Putz R. Tenozyten und extrazelluläre matrix. Orthopade. 2009;38(11):1071–9.
364. Schmittgen TD, Livak KJ. Analyzing real-time PCR data by the comparative CT method. Nat Protoc. 2008;3(6):1101–8.
365. Cebotari S, Lichtenberg A, Tudorache I, Hilfiker A, Mertsching H, Leyh R, et al. Clinical application of tissue engineered human heart valves using autologous progenitor cells. Circulation. 2006 Jul;114(1 Suppl):I132-7.
366. Uygun BE, Soto-Gutierrez A, Yagi H, Izamis ML, Guzzardi MA, Shulman C, et al. Organ reengineering through development of a transplantable recellularized liver graft using decellularized liver matrix. Nat Med. 2010 Jul;16(7):814–20.

367. Song JJ, Guyette JP, Gilpin SE, Gonzalez G, Vacanti JP, Ott HC. Regeneration and experimental orthotopic transplantation of a bioengineered kidney. Nat Med. 2013 May;19(5):646–51.
368. de Lima Santos A, da Silva CG, de Sá Barreto LS, Leite KRM, Tamaoki MJS, Ferreira LM, et al. A new decellularized tendon scaffold for rotator cuff tears – evaluation in rabbits. BMC Musculoskelet Disord. 2020;21(1):689.
369. Wang S, Wang Y, Song L, Chen J, Ma Y, Chen Y, et al. Decellularized tendon as a prospective scaffold for tendon repair. Mater Sci Eng C Mater Biol Appl. 2017 Aug;77:1290–301.
370. Zhu J, Li J, Wang B, Zhang WJ, Zhou G, Cao Y, et al. The regulation of phenotype of cultured tenocytes by microgrooved surface structure. Biomaterials. 2010 Sep;31(27):6952–8.
371. Zabrzyński J, Gagat M, Paczesny Ł, Łapaj Ł, Grzanka D. Electron microscope study of the advanced tendinopathy process of the long head of the biceps brachii tendon treated arthroscopically. Folia Morphol (Warsz). 2018;77(2):371–7.
372. Abraham T, Fong G, Scott A. Second harmonic generation analysis of early Achilles tendinosis in response to in vivo mechanical loading. BMC Musculoskelet Disord. 2011 Jan;12:26.
373. Patel D, Sharma S, Screen HRC, Bryant SJ. Effects of cell adhesion motif, fiber stiffness, and cyclic strain on tenocyte gene expression in a tendon mimetic fiber composite hydrogel. Biochem Biophys Res Commun. 2018;499(3):642–7.
374. Gaspar D, Pandit A, Zeugolis D. Tenogenic phenotype maintenance and differentiation using macromolecular crowding and mechanical loading. Orthopaedic Proceedings. 2017;99-B(SUPP_1):39.
375. Huisman E, Lu A, McCormack RG, Scott A. Enhanced collagen type I synthesis by human tenocytes subjected to periodic in vitro mechanical stimulation. BMC Musculoskelet Disord. 2014 Nov;15:386.
376. Deniz P, Guler S, Çelik E, Hosseinian P, Aydin HM. Use of cyclic strain bioreactor for the upregulation of key tenocyte gene expression on Poly(glycerol-sebacate) (PGS) sheets. Materials Science and Engineering: C. 2020;106:110293.
377. Fleischhacker V, Klatte-Schulz F, Minkwitz S, Schmock A, Rummler M, Seliger A, et al. In vivo and in vitro mechanical loading of mouse Achilles tendons and tenocytes-a pilot study. Int J Mol Sci. 2020 Feb;21(4).

378. John T, Lodka D, Kohl B, Ertel W, Jammrath J, Conrad C, et al. Effect of pro-inflammatory and immunoregulatory cytokines on human tenocytes. Journal of Orthopaedic Research. 2010;28(8):1071–7.
379. Abbah SA, Thomas D, Browne S, O'Brien T, Pandit A, Zeugolis DI. Co-transfection of decorin and interleukin-10 modulates pro-fibrotic extracellular matrix gene expression in human tenocyte culture. Sci Rep. 2016;6(1):20922.
380. Robert L, Jacob MP, Fülöp T. Elastin in blood vessels. Ciba Found Symp. 1995;192:286–303.
381. Zelle BA, Fu FH. Chapter 1 - Pathogenesis of soft tissue and bone repair. In: Maxey L, Magnusson J, editors. Rehabilitation for the Postsurgical Orthopedic Patient (Third Edition). Third Edit. St. Louis (MO): Mosby; 2013. p. 2–14.
382. Lee C. Tendon physiology and repair. Orthop Trauma. 2021;35(5):274–81.
383. Swedberg AM, Reese SP, Maas SA, Ellis BJ, Weiss JA. Continuum description of the Poisson's ratio of ligament and tendon under finite deformation. J Biomech. 2014 Sep;47(12):3201–9.
384. Reese SP, Maas SA, Weiss JA. Micromechanical models of helical superstructures in ligament and tendon fibers predict large Poisson's ratios. J Biomech. 2010;43(7):1394–400.
385. Vergari C, Pourcelot P, Holden L, Ravary-Plumioën B, Gerard G, Laugier P, et al. True stress and Poisson's ratio of tendons during loading. J Biomech. 2011;44(4):719–24.
386. Vergari C, Pourcelot P, Holden L, Ravary-Plumioën B, Gerard G, Laugier P, et al. True stress and Poisson's ratio of tendons during loading. J Biomech. 2011 Feb;44(4):719–24.
387. POTENZA AD. Tendon healing within the flexor digital sheath in the dog. J Bone Joint Surg Am. 1962 Jan;44-A:49–64.
388. Gelberman RH, Amifl D, Gonsalves M, Woo S, Akeson WH. The influence of protected passive mobilization on the healing of flexor tendons: a biochemical and microangiographic study. Hand. 1981 Jun;13(2):120–8.
389. Matthews JP. Vascular changes in flexor tendons after injury and repair: an experimental study. Injury. 1977 Feb;8(3):227–33.
390. Curtis L. Nutritional research may be useful in treating tendon injuries. Nutrition. 2016 Jun;32(6):617–9.
391. Fahem A, Robinet A, Cauchard JH, Duca L, Soula-Rothhut M, Rothhut B, et al. Elastokine-mediated up-regulation of MT1-MMP is triggered by nitric oxide in endothelial cells. Int J Biochem Cell Biol. 2008;40(8):1581–96.

392. Nackman GB, Karkowski FJ, Halpern VJ, Gaetz HP, Tilson MD. Elastin degradation products induce adventitial angiogenesis in the Anidjar/Dobrin rat aneurysm model. Surgery. 1997 Jul;122(1):39–44.
393. Järvinen TA. Neovascularisation in tendinopathy: from eradication to stabilisation? Vol. 54, British journal of sports medicine. 2020. p. 1–2.
394. Abate M, Silbernagel KG, Siljeholm C, di Iorio A, de Amicis D, Salini V, et al. Pathogenesis of tendinopathies: inflammation or degeneration? Arthritis Res Ther. 2009;11(3):235.
395. Ohberg L, Lorentzon R, Alfredson H. Neovascularisation in Achilles tendons with painful tendinosis but not in normal tendons: an ultrasonographic investigation. Knee Surg Sports Traumatol Arthrosc. 2001 Jul;9(4):233–8.
396. Gisslén K, Alfredson H. Neovascularisation and pain in jumper's knee: a prospective clinical and sonographic study in elite junior volleyball players. Br J Sports Med. 2005 Jul;39(7):423–8.
397. Knobloch K, Kraemer R, Lichtenberg A, Jagodzinski M, Gossling T, Richter M, et al. Achilles tendon and paratendon microcirculation in midportion and insertional tendinopathy in athletes. Am J Sports Med. 2006 Jan;34(1):92–7.
398. Beck S, Blunden T, Dyson S, Murray R. Are matrix and vascular changes involved in the pathogenesis of deep digital flexor tendon injury in the horse? The Veterinary Journal. 2011;189(3):289–95.
399. Chen J, Yu Q, Wu B, Lin Z, Pavlos NJ, Xu J, et al. Autologous tenocyte therapy for experimental Achilles tendinopathy in a rabbit model. Tissue Eng Part A. 2011 Aug;17(15–16):2037–48.
400. Bhattacharya AK, Awan OA, Fenerty S, Taqi I, Jonnalagadda P, Ling S, et al. Repetitive strain injuries of the upper extremity: imaging of tendon pathology and compressive neuropathies. Curr Probl Diagn Radiol. 2021;50(4):512–22.
401. Järvinen M, Józsa L, Kannus P, Järvinen TL, Kvist M, Leadbetter W. Histopathological findings in chronic tendon disorders. Scand J Med Sci Sports. 1997 Apr;7(2):86–95.
402. McIntyre A, Harris AL. Metabolic and hypoxic adaptation to anti-angiogenic therapy: a target for induced essentiality. EMBO Mol Med. 2015 Apr;7(4):368–79.
403. Kaux JF, Forthomme B, Goff C le, Crielaard JM, Croisier JL. Current opinions on tendinopathy. J Sports Sci Med. 2011 Jun;10(2):238–53.
404. Simpson M, Rio E, Cook J. At what age do children and adolescents develop lower limb tendon pathology or tendinopathy? A systematic review and meta-analysis. Sports Med. 2016 Apr;46(4):545–57.

405. Cairns G, Owen T, Kluzek S, Thurley N, Holden S, Rathleff MS, et al. Therapeutic interventions in children and adolescents with patellar tendon related pain: a systematic review. BMJ Open Sport Exerc Med. 2018;4(1):e000383.
406. Yamamoto E, Hayashi K, Yamamoto N. Mechanical properties of collagen fascicles from the rabbit patellar tendon. J Biomech Eng. 1999 Feb;121(1):124–31.
407. Reuvers J, Thoreson AR, Zhao C, Zhang L, Jay GD, An KN, et al. The mechanical properties of tail tendon fascicles from lubricin knockout, wild type and heterozygous mice. J Struct Biol. 2011 Oct;176(1):41–5.
408. Svensson RB, Hassenkam T, Grant CA, Magnusson SP. Tensile properties of human collagen fibrils and fascicles are insensitive to environmental salts. Biophys J. 2010 Dec;99(12):4020–7.
409. Hasan A, Memic A, Annabi N, Hossain M, Paul A, Dokmeci MR, et al. Electrospun scaffolds for tissue engineering of vascular grafts. Acta Biomater. 2014;10(1):11–25.
410. Stekelenburg M, Rutten MCM, Snoeckx LHEH, Baaijens FPT. Dynamic straining combined with fibrin gel cell seeding improves strength of tissue-engineered small-diameter vascular grafts. Tissue Eng Part A. 2009 May;15(5):1081–9.
411. Porter TR, Taylor DO, Fields J, Cycan A, Akosah K, Mohanty PK, et al. Direct in vivo evaluation of pulmonary arterial pathology in chronic congestive heart failure with catheter-based intravascular ultrasound imaging. Am J Cardiol. 1993 Mar;71(8):754–7.
412. Soletti L, Hong Y, Guan J, Stankus JJ, El-Kurdi MS, Wagner WR, et al. A bilayered elastomeric scaffold for tissue engineering of small diameter vascular grafts. Acta Biomater. 2010 Jan;6(1):110–22.
413. Wiesinger HP, Seynnes OR, Kösters A, Müller E, Rieder F. Mechanical and material tendon properties in patients with proximal patellar tendinopathy. Front Physiol. 2020;11:704.
414. Wunderli SL, Blache U, Beretta Piccoli A, Niederöst B, Holenstein CN, Passini FS, et al. Tendon response to matrix unloading is determined by the patho-physiological niche. Matrix Biol. 2020 Jul;89:11–26.
415. Cook JL, Malliaras P, de Luca J, Ptasznik R, Morris M. Vascularity and pain in the patellar tendon of adult jumping athletes: a 5 month longitudinal study. Br J Sports Med. 2005;39(7):458–61.
416. Liu YB, Li SJ, Zhao L, Yu B, Zhao DH. Timing for Ponseti clubfoot management: does the age matter? 90 children (131 feet) with a mean follow-up of 5 years. Acta Orthop. 2018 Dec;89(6):662–7.

417. Bashi RHZ, Baghdadi T, Shirazi MR, Abdi R, Aslani H. Modified Ponseti method of treatment for correction of neglected clubfoot in older children and adolescents--a preliminary report. J Pediatr Orthop B. 2016 Mar;25(2):99–103.
418. Ganesan B, Luximon A, Al-Jumaily A, Balasankar SK, Naik GR. Ponseti method in the management of clubfoot under 2 years of age: A systematic review. PLoS One. 2017;12(6):e0178299.
419. Sihota P, Yadav RN, Dhiman V, Bhadada SK, Mehandia V, Kumar N. Investigation of diabetic patient's fingernail quality to monitor type 2 diabetes induced tissue damage. Sci Rep. 2019;9(1):3193.
420. McClintock DE, Starcher B, Eisner MD, Thompson BT, Hayden DL, Church GD, et al. Higher urine desmosine levels are associated with mortality in patients with acute lung injury. Am J Physiol Lung Cell Mol Physiol. 2006 Oct;291(4):L566-71.
421. Luisetti M, Ma S, Iadarola P, Stone PJ, Viglio S, Casado B, et al. Desmosine as a biomarker of elastin degradation in COPD: current status and future directions. European Respiratory Journal. 2008;32(5):1146–57.